NUMERICAL SIMULATIONS OF VIOLENT FREE SURFACE BY A COUPLED LEVEL-SET AND VOLUME-OF-FLUID METHOD

A Dissertation

by

YUCHENG ZHAO

Submitted to the Office of Graduate and Professional Studies of
Texas A&M University
in partial fulfillment of the requirements for the degree of

DOCTOR OF PHILOSOPHY

Chair of Committee,	Hamn-Ching Chen
Committee Members,	Jun Zhang
	Robert Handler
	Scott A. Socolofsky
Head of Department,	Robin Autenrieth

May 2014

Major Subject: Ocean Engineering

ABSTRACT

This study contributes to the development of a Coupled Level-Set and Volume-Of-Fluid (CLSVOF) method capable of capturing interface between two immiscible fluids in overset grid system. The present CLSVOF interface-capturing method is employed in conjunction with the Finite-Analytical Navier-Stokes (FANS) method for time-domain simulations of violent free surface flow problems.

In this method, immiscible two-phase flow is modeled as a single continuum with variable fluid properties across the interface. The interface is captured by a level set function which is corrected to ensure mass conservation under the framework of a volume of fluid function. The interface is propagated by the evolution of the level set and volume of fluid functions in time. In addition, the conservation equations for mass and momentum are solved in the transformed domain for the dynamics of the fluid flow. Moreover, a chimera domain decomposition approach is implemented using overset grid systems, including embedding, overlapping, and matching grids for accurate resolutions of all varieties of free surface flow problems.

DEDICATION

To my beloved grandfather,

who adored his grandson by providing

unconditional love, kindness, and comfort in life.

I will always remember the smiles and laughter on his face.

ACKNOWLEDGEMENTS

I would like to express my deepest gratitude to the advisor and committee chair, Dr. Chen, for his instruction, patience and support throughout my graduate study. Without his guidance, I would never have stepped into CFD research field.

I would like to extend my gratefulness to my committee members, Dr. Zhang, Dr. Socolofsky, and Dr. Handler, for their valuable time, suggestions and personal encouragement.

I would also like to give a heartfelt thank you to my parents and my beloved wife for their boundless love, firm support and everlasting encouragement throughout my educational years.

TABLE OF CONTENTS

Page

ABSTRACT ii

DEDICATION iii

ACKNOWLEDGEMENTS iv

TABLE OF CONTENTS v

LIST OF FIGURES vii

LIST OF TABLES x

CHAPTER I INTRODUCTION 1

1.1 Background 1
1.2 Literature Review 2
1.2.1 The Marker method 2
1.2.2 The VOF method 3
1.2.3 The LS method 7
1.2.4 The hybrid method 8
1.3 The Method of Present Study 9

CHAPTER II GOVERNING EQUATIONS 10

2.1 Introduction 10
2.2 LS Equation and VOF Equation 10
2.3 RANS Equations 12

CHAPTER III NUMERICAL METHOD 17

3.1 Introduction 17
3.2 Level Set Equation 17
3.3 VOF Equation 21
3.3.1 Interface reconstruction algorithm 21
3.3.2 Interface advection algorithm 25
3.3.3 LS re-distance algorithm 37
3.4 VOF Function for Overset Grid System 44
3.5 Mass Conservation Scheme for Overset Grid System 47

Page

3.6 Summary of Present CLSVOF Method 48

CHAPTER IV TEST CASES 50

4.1 Introduction 50
4.2 2D Single Vortex Flow 50
4.3 3D Single Vortex Flow 53
4.4 3D Deformation Flow with Overset Grid System 55
4.5 2D Dam Breaking Flow 57
4.6 3D Dam Breaking Flow 59
4.7 3D Dam Breaking Flow with Cylindrical Pillar 62

CHAPTER V SLOSHING FLOW IN PARTIALLY FILLED LNG TANK 65

5.1 Introduction 65
5.2 Experimental and Numerical Setups 67
5.3 Results and Discussions 72
5.3.1 Case 1: transverse motion at 30% filling level 74
5.3.2 Case 2: transverse motion at 50% filling level 84
5.3.3 Case 3: longitudinal motion at 80% filling level 94
5.3.4 Case 4: longitudinal motion at 92.5% filling level 102

CHAPTER VI REGULAR WAVES SLAMMING ON PLATFORM 113

6.1 Introduction 113
6.2 Experimental and Numerical Setups 114
6.3 Results and Discussions 117
6.3.1 Case 1: 0° direction of wave propagation 118
6.3.2 Case 2: 30° direction of wave propagation 122

CHAPTER VII CONCLUSIONS 126

REFERENCES 129

LIST OF FIGURES

FIGURE		Page
1.1	Schematic of SLIC and PLIC	4
3.1	General curvilinear grid and transformed grid	18
3.2	2D and 3D reconstructed interface	22
3.3	Schematic diagram of 2nd order Runge-Kutta method	26
3.4	2D EI-LE interface advection scheme	28
3.5	Volume integration after LE scheme	34
3.6	Schematic diagram for the LS function re-distance	39
3.7	Schematic for tri-linear interpolation	44
3.8	Evaluation of the VOF function on overset grid boundary	45
3.9	Flow chart of the CLSVOF method	49
4.1	Numerical grids and initial circular fluid	51
4.2	Single vortex flow test	51
4.3	3D deformation of a sphere at t = 0, 1.0, 1.5 and 3	54
4.4	Overset grid system for simulation of sphere deformation	56
4.5	Deformation of a sphere in overset grids	57
4.6	Free surface pattern in 2D dam breaking	58
4.7	Free surface pattern for 3D dam breaking problem	60
4.8	Comparison of numerical results and experimental data	61
4.9	3D dam breaking around a cylindrical pillar	63

FIGURE Page

5.1 Schematic of tank geometry 68

5.2 Locations of the pressure transducers 69

5.3 Transverse and longitudinal motions in grid planes 70

5.4 Sensor locations for numerical simulations 73

5.5 Tank motion trajectory in Case 1 74

5.6 Impact pressure histories by the CLSVOF method in Case 1 75

5.7 Comparisons of measured and predicted pressures in Case 1 77

5.8 Predicted pressures by CLSVOF and improved LS method in Case 1 78

5.9 Free surface pattern and wall pressure contours in Case 1 79

5.10 Relative mass change in Case 1 83

5.11 Tank motion trajectory in Case 2 85

5.12 Impact pressure histories by the CLSVOF method in Case 2 86

5.13 Comparisons of measured and predicted pressures in Case 2 87

5.14 Comparisons of predicted pressures in Case 2 88

5.15 Free surface pattern and wall pressure contours in Case 2 90

5.16 Relative mass change in Case 2 93

5.17 Tank motion trajectory in Case 3 94

5.18 Impact pressure histories by the CLSVOF method in Case 3 95

5.19 Comparisons of measured and predicted pressures in Case 3 96

5.20 Comparisons of predicted pressures in Case 3 97

5.21 Free surface pattern and wall pressure contours in Case 3 98

FIGURE Page

5.22 Relative mass change in Case 3 102

5.23 Tank motion trajectory in Case 4 103

5.24 Impact pressure histories by the CLSVOF method in Case 4 104

5.25 Comparisons of measured and predicted pressures in Case 4 105

5.26 Comparisons of predicted pressures in Case 4 106

5.27 Free surface pattern and wall pressure contours in Case 4 108

5.28 Relative mass change in Case 4 111

6.1 Schematic of deck geometry and locations of the pressure transducers 115

6.2 Sketch of direction of wave propagation 115

6.3 Overset grid system 117

6.4 Free surface pattern in top view and side view, Case 1 119

6.5 Wave slamming impact forces, Case 1 121

6.6 Free surface pattern in top view and side view, Case 2 123

6.7 Wave slamming impact forces, Case 2 125

LIST OF TABLES

TABLE Page

5.1 Filling levels, tank motion modes, periods and selected sensor..... 71

5.2 Tank motion amplitudes..... 71

5.3 Physical properties of liquids in LNG tank..... 72

CHAPTER I

INTRODUCTION

1.1 Background

The objective of this study is devoted to the development of an accurate, effective and robust Computational Fluid Dynamics (CFD) methodology which is capable of predicting violent free surface flows with a sharp interface.

The flows involving two different immiscible fluids with a well defined interface are commonly encountered in many industrial processes. Among these circumstances, free surface flows, which are known as air-water flows, feature prominently in ocean environment. Another particular area of interest is sloshing phenomena inside Liquefied Natural Gas (LNG) carrier tanks with partial filling condition. These interactions exert unsteady dynamic loads on offshore and ship structures and strongly influence the offshore and ship structure design.

This study mainly handles two-phase immiscible fluids flow (air-liquid flow) problems and numerically predicts the flow behavior. Numerical simulations of such flows are difficult because the interface separating different fluid phases, whose position is not prescribed a priori, must be accurately solved. Eligible numerical methods also deal with the requirements including conservation, generality, high accuracy, minimal computer storage, calculation time, etc.

The preliminary work about CFD methodology capable of predicting interface flow dates as far back as the early 1960s. Since that time, many novel approaches have

appeared. The next section gives an overview of the development of these numerical approaches in historical perspective, and also their advantages/disadvantages. The followed section outlines the contribution of this dissertation.

1.2 Literature Review

Extensive studies have been devoted to the prediction of two-phase fluids flow over the past several decades. The Marker method [1], [2], the Volume-of-Fluid (VOF) method [3], [4] and the Level-Set method [5] are the most common numerical strategies used to predict interface motion.

1.2.1 The Marker method

In the Marker method, marker particles are used to locate the phases or the interface. It can be further divided into the volume-marker method and the surface-marker method. The volume-marker method introduces marker particles in the domain occupied by one fluid phase; the surface-marker method created marker particles only on the interface. The local velocities are used to advect these marker particles in a Lagrangian manner following the velocity streamlines. In the well-known Marker-and-Cell (MAC) method of Harlow and Welch [1], marker particles are introduced to identify the region occupied by a single phase with a free surface. Daly presented a method to track an interface explicitly on a fixed grid by marking the interface with a set of connected mass-less marker particles [2]. The Marker method has several advantages, and an important one is the high degree of accuracy that may be achieved by

representing the interface through high-order interpolation polynomials. However, it requires colossal computer storage and significant additional computational time to update the motion of all the particles, especially when a three-dimensional problem is encountered.

1.2.2 The VOF method

In the VOF method, the interface is represented by a VOF function. The VOF function, defined as C, represents the volume fraction of a reference phase in a computational cell. Its value is between zero and one in cells cut by the interface. The values are zero or one where the cells are away from the interface. The VOF function is based on the characteristic function χ that has the value 1 in the reference phase and 0 in the other phase. Since each elementary fluid parcel does not change its own phase along particle paths in the immiscible fluids, the characteristic function χ is passively advected by the flow. Hence, χ satisfies the advection equation (1.1),

$$\frac{D\chi}{Dt} = \frac{\partial \chi}{\partial t} + (\vec{V} \bullet \nabla)\chi = 0 \tag{1.1}$$

The advection equation of the VOF equation (1.2) is a discrete analog of equation (1.1),

$$\frac{DC}{Dt} = \frac{\partial C}{\partial t} + (\vec{V} \bullet \nabla)C = 0 \tag{1.2}$$

Moreover, particular attention must be given to the consistency property of the VOF function,

$$0 \le C \le 1 \tag{1.3}$$

When the value of the VOF function is outside the range of the consistency property, it indicates that the law of physics is violated. In an incompressible flow, mass conservation is equivalent to conservation of volume and hence of the VOF function. Thus, it is a unique advantage for the VOF method because it has potential to conserve mass. However, a given distribution of the VOF function does not guarantee a unique interface topology. The interface geometry is only inferred from the VOF function field by reconstruction algorithm (figure 1.1(a) and figure 1.1(b)). The principal reconstruction constraint is local volume conservation: the reconstructed interface must truncate cells with a volume equal to the local fluid volume. The interface is tracked by evolving the VOF function forward in time with particular advection algorithm for the VOF function advection equation. In general, reconstruction algorithm and advection algorithm are the two procedures which mainly comprise the unique features of a given VOF method.

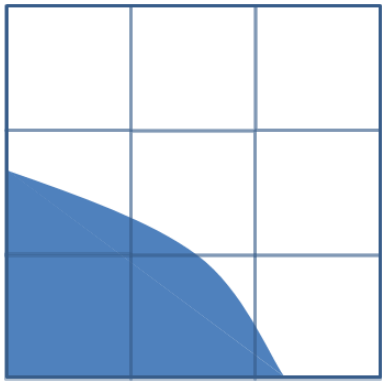

0	0	0
0.5	0.2	0
1	0.8	0.1

(a) Actual Interface (b) Distribution of the VOF function

Figure 1.1: Schematic of SLIC and PLIC

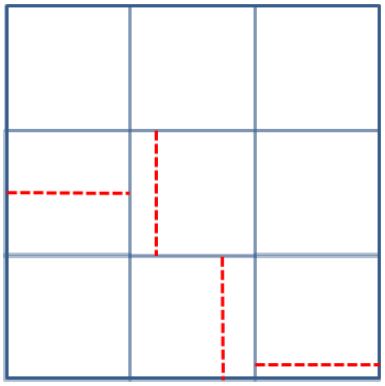

(c) SLIC

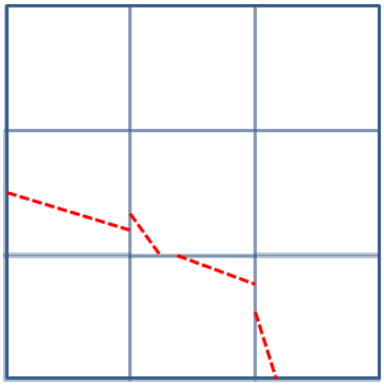

(d) PLIC

Figure 1.1: (Continued)

Reconstruction algorithm is to evaluate an approximation to the section of the interface in each cut cell. The simplest type of reconstruction algorithms is the Simple Line Interface Calculation (SLIC) of Noh and Woodward (1976) [4]. In SLIC reconstruction in figure 1.1(c), the interface in each cut cell is a segment parallel to one of the grid coordinate axis. SLIC reconstruction algorithm has featured in many commercial CFD codes, SOLA-VOF (Nichols et al., 1980) [3] and its descendants NASA-VOF2D (Torrey et al., 1985) [6], NASA-VOF3D (Torrey et al., 1987) [7], RIPPLE (Kothe, Mjolsness and Torrey, 1991; Kothe and Mjolsness, 1992) [8],[9] and FLOW3D (Hirt and Nichols, 1988) [10]. However, SLIC algorithms only rely on a piecewise constant or "staircase" representation of the interface which is relatively crude. The more modern and accurate reconstruction technique is known as the Piecewise Linear Interface Construction (PLIC). In PLIC technique, the interface is a segment perpendicular to the gradient of the VOF function in figure 1.1(d). One of the critical simplifying features of PLIC algorithms is that the reconstructed interface is not forced to form by a chain of joined segments but rather by a discontinuous chain. PLIC

techniques are more complex but accurate than SLIC technique. Youngs' PLIC reconstruction positioned each reconstructed interface line, defined by a slope and intercept [11]. Numerous extensions and enhancements to the significant work of Youngs have occurred since its introduction. Johnson extended Youngs' method to non-orthogonal meshes [12]. Colella et al. used adaptive mesh refinement (AMR) in the VOF method [13]. Puckett and Puckett refined Youngs' algorithm in two dimensions with an un-split, "corner-coupled" time integration scheme extension that has second-order accuracy [14].

The following step is advection algorithm. Once the interface has been reconstructed, its motion by the velocity flow field must be modeled by a suitable advection algorithm. Most of the advection algorithms are based on structured grids, either with a split scheme or an un-split scheme. More particularly, the advection of the VOF function can be updated independently along each coordinate direction, with multidimensionality obtained by an operator split technique [15]. Alternatively, there are a few of un-split multidimensional schemes dependent on each coordinate direction [14], [16], [17]. Overall, un-split algorithms are more complex in geometry, while split algorithms are more robust in implementation. For triangular unstructured grids, a promising method is the Lagrangian-Eulerian advection method, which is independent of the grid type [18], [19]. It is suitable for both rectangular structured grids and triangular unstructured grids.

A drawback of the VOF method is that it is hard to compute accurate interface normal and curvature because the VOF function is discontinuous. Several algorithms

[20]-[23] have been developed for normal vector calculations. However, most of them are less than second order accurate. It is even more difficult to calculate curvature which involves taking second order derivatives of the VOF function.

1.2.3 The LS method

In the LS method, the interface is tracked by a LS function. The LS function, specified as ϕ, is a smooth function and is initialized to the signed distance from the interface. The value is zero on an interface, negative in one phase, and positive in the other phase. Thus, the interface coincides with the zero level of the LS function. The advection equation of the LS function by the underlying velocity field $\vec{V}$ is,

$$\frac{\partial \phi}{\partial t} + (\vec{V} \bullet \nabla)\phi = 0 \tag{1.4}$$

Osher and Sethian (1988) proved that the interface will remain at the zero level, but the LS function does not always maintain as a signed distance function when the interface evolves [5]. Therefore, a re-distancing or re-initialization procedure is necessary to adjust the LS function to maintain as a signed distance function while the zero level of the LS function remains the same. Sussman et al. (1994) proposed a re-distancing equation until the steady state is reached to modify the LS function [24],

$$\frac{\partial \phi}{\partial \tau} = sign(\phi_0) \cdot (1 - |\nabla \phi|) \tag{1.5}$$

The advantage of the LS method is that it can handle the complex interface geometry automatically, and it is not necessary to explicitly reconstruct the interface as

the VOF method does. Since the LS function is a smooth function, the unit normal $\vec{m}$ and curvature κ of the interface can be accurately calculated from the LS function,

$$\vec{m} = \frac{\nabla \phi}{|\nabla \phi|} \tag{1.6}$$

$$\kappa = \nabla \cdot \frac{\nabla \phi}{|\nabla \phi|} \tag{1.7}$$

However, the drawback is that the LS method is not able to preserve mass conservation because of the numerical dissipation across the interface. It is prone to more numerical error when the interface experiences severe stretching or tearing. In order to improve mass conservation, many research groups extended the original LS method. Sussman et al. (1998) first introduced a new constraint term in the re-distancing scheme to improve accuracy and efficiency [25]. Takahira et al. (2004) improved the re-initialization procedure of the LS function by adding a multiplier of the order of one to the constraint term in order to recover the mass [26]. Van der Pijl et al. presented the mass conserving level set method (MCLS) [27]. Unfortunately, the inherent mass conservation problem still exists.

1.2.4 The hybrid method

From the general point of view of the choice among various methods in interface tracking such as the Marker method, the VOF method and the LS method, it is desirable to retain the strong point and avoid the weak point. A few of hybrid methods have been developed recently. A coupled method can take advantage of the strengths of each of the

two coupled methods, and is superior to either single method. Enright et al. proposed a hybrid particle level set method for improved interface capturing [28]. Aulisa et al. presented a mixed markers and VOF method for the interface in two-phase and free boundary flows [29]. Sussman and Puckett developed a coupled level set and VOF method for computing 3D and axisymmetric incompressible two-phase flow [30]. Sussman also extended a coupled level set and VOF method for an adaptive Cartesian grid [31].

1.3 The Method of Present Study

The present study inherits the work about the pure level set method incorporated into the Chimera FANS method for the predictions of various free surface problems. On this basis, the pure LS method was extended to the coupled level set and VOF (CLSVOF) method by introducing a VOF function and its evolution simultaneously with the evolution of the LS function. For the level set method part, a 5^{th} order Weighted Essentially Non-Oscillatory (WENO) scheme was used for spatial derivatives instead of 3^{rd} order Essentially Non-Oscillatory (ENO) scheme. For the VOF method part, PLIC algorithm was employed to reconstruct the interface and a mixed 2^{nd} order Lagrangian and Eulerian advection scheme was used to update the VOF function. The level set re-distancing procedure was also modified for LS function based on the reconstructed interface on the computational domain. Finally, the work about the VOF method and new level set re-distancing procedure was implemented for overset grid system.

CHAPTER II

GOVERNING EQUATIONS

2.1 Introduction

This chapter describes the mathematical model of the two-phase fluids flow and the movement of the interface separating the fluids. The two-phase fluids flow is modeled as a single continuum with variable fluid properties across the interface. The interface is implicitly defined by the LS function which is corrected by the VOF function in the CLSVOF method. The CLSVOF method is generally applied for any immiscible two-phase fluids flow. In keeping with ocean engineering field closely, air-water fluids flow is taken as a particular two-phase flow in following sections. In addition, this approach is also equally applicable for both laminar and turbulent flows.

2.2 LS Equation and VOF Equation

As mentioned in Chapter I, the LS function is specified as a signed distance from the interface. The interface Γ can be represented by the zero LS function,

$$\Gamma = \{\vec{x} \mid \phi(\vec{x}, t) = 0\} \tag{2.1}$$

And the region of air and water phase can be distinguished by the sign of the LS function,

$$\phi(\vec{x}, t) = \begin{cases} > 0 & for \vec{x} \in water \\ = 0 & for \vec{x} \in \Gamma \\ < 0 & for \vec{x} \in air \end{cases} \tag{2.2}$$

During the time evolution, the advection equation of the LS function in the velocity field $\vec{V}$ as follows,

$$\frac{\partial \phi}{\partial t} + \vec{V} \cdot \nabla \phi = 0 \tag{2.3}$$

In the present two-phase flow formulation, both the density ρ and the viscosity μ nearby the interface depend on the LS function. The region where both the density and the viscosity vary is set as a transition zone. A transition zone is defined by $|\phi| \leq \varepsilon$, where ε is the half thickness of the interface. In the transition of the interface, the fluid properties can be smoothed by the smoothed Heaviside function.

$$\begin{cases} \rho(\phi) = \rho_a + (\rho_l - \rho_a) \cdot H(\phi) \\ \mu(\phi) = \mu_a + (\mu_l - \mu_a) \cdot H(\phi) \end{cases} \tag{2.4}$$

where the subscripts a and l represent air and liquid phases; the smoothed Heaviside function is specified as,

$$H(\phi) = \begin{cases} 0 & if\ \phi < -\varepsilon \\ \frac{1}{2}\left(1 + \frac{\phi}{\varepsilon} + \frac{1}{\pi}\sin(\frac{\pi\phi}{\varepsilon})\right) & if\ -\varepsilon \leq \phi \leq \varepsilon \\ 1 & if\ \phi > \varepsilon \end{cases} \tag{2.5}$$

It is desirable to maintain the LS function as a signed distance to the interface in every time instance. In order to ensure the LS function as a signed distance, a process called re-distance is introduced to reconstruct ϕ. Re-distance algorithm maintains a signed distance property by solving the re-distance equation to steady state,

$$\phi_\tau + sign(\phi_0)(|\nabla \phi| - 1) = 0 \tag{2.6}$$

where τ is fictional time, $sign(\phi_0)$ is one-dimensional sign function which is smeared out by a small value ε,

$$sign(\phi_0) = \frac{\phi_0}{\sqrt{\phi_0^2 + (\varepsilon)^2}} \tag{2.7}$$

The VOF function, C, represents the volume fraction of the water in a computational cell. Its value is between zero and one in cells cut by the interface; zero and one away from the interface, respectively. The cells can be divided into two groups by the value of the VOF function: cut cell with the value between zero and one indicates the interface segment located inside the cell; full cell with the value of zero or one means only one phase flow inside the cell.

$$\begin{cases} 0 < C < 1 & cut \quad cell \\ C = 0; C = 1 & full \quad cell \end{cases} \tag{2.8}$$

The advection equation of the VOF function in the velocity field $\vec{V}$ as follows,

$$\frac{\partial C}{\partial t} + \vec{V} \cdot \nabla C = 0 \tag{2.9}$$

2.3 RANS Equations

The Navier-Stokes equations are modified by the LS function, because both the density and viscosity nearby the air-water interface depend on the LS function. This enables the present method to handle air-water fluid as a single continuum with variable fluid properties across the interface.

At first, it is assumed that both water and air phase fluids are governed by the incompressible Navier-Stokes equations,

$$\begin{cases} \rho_w(\frac{\partial \overrightarrow{V'}}{\partial t'} + \overrightarrow{V'} \cdot \nabla \overrightarrow{V'}) = \rho_w \vec{g} + \mu_w \nabla^2 \overrightarrow{V'} - \nabla p' \\ \rho_a(\frac{\partial \overrightarrow{V'}}{\partial t'} + \overrightarrow{V'} \cdot \nabla \overrightarrow{V'}) = \rho_a \vec{g} + \mu_a \nabla^2 \overrightarrow{V'} - \nabla p' \end{cases} \tag{2.10}$$

where t is time, $\overrightarrow{V'}$ is the velocity vector, $\vec{g}$ is the acceleration due to gravity, p' is pressure, and the superscript means the equations are in the dimensional form.

The equation (2.10) can be normalized by the characteristic length L and the characteristic velocity U_0.

$$\vec{V} = \frac{\overrightarrow{V'}}{U_0}, t = \frac{t'}{t_0} = \frac{U_0}{L} t', p = \frac{p'}{\rho_w U_0^2} \tag{2.11}$$

In addition, the non-dimensional density $\rho(\phi)$ and non-dimensional dynamic viscosity $\mu(\phi)$ can be represented as below:

$$\begin{cases} \rho(\phi) = \rho_a / \rho_l + (1 - \rho_a / \rho_l) \cdot H(\phi) \\ \mu(\phi) = \mu_a / \mu_l + (1 - \mu_a / \mu_l) \cdot H(\phi) \end{cases} \tag{2.12}$$

After dividing by $\rho_w U_0^2 / L$ and combining the equation (2.10) together, the Navier-Stokes equations for two-phase fluid in non-dimensional form is,

$$\frac{\partial \vec{V}}{\partial t} + \vec{V} \cdot \nabla \vec{V} = -\frac{\delta_{i,3}}{Fr^2} + \frac{\nu(\phi)}{\mathrm{Re}} \nabla^2 \vec{V} - \frac{1}{\rho(\phi)} \nabla p \tag{2.13}$$

where $\delta_{i,j}$ is the Kronecker delta function, $\nu(\phi) = \rho(\phi)/\mu(\phi)$ is the normalized kinematic viscosity, p is pressure, Froude number $Fr = \sqrt{\frac{U_0^{\ 2}}{gL}}$ and Reynolds number $\mathrm{Re} = \frac{\rho_w U_0 L}{\mu_w}$.

The continuity and momentum equations are transformed to the general curvilinear coordinates $x^i = (x^1, x^2, x^3)$,

$$\begin{cases} \sum_{i=1}^{3} \frac{\partial U_i}{\partial x^i} = 0 \\ \frac{\partial U_i}{\partial t} + \sum_{j=1}^{3} (U_j \frac{\partial U_i}{\partial x^j} + \frac{\partial \overline{u_i u_j}}{\partial x^j}) + \frac{1}{\rho(\phi)} \frac{\partial p}{\partial x^i} - \frac{\nu(\phi)}{\mathrm{Re}} \nabla^2 U_i + \frac{\delta_{i,3}}{Fr^2} = 0 \end{cases} \tag{2.14}$$

where $\nabla^2 = \sum_{i=1}^{3} \frac{\partial^2}{\partial x^j \partial x^j}$

The Reynolds stresses $\overline{u_i u_j}$ are related to the corresponding mean rate of strain through an isotropic eddy viscosity ν_t,

$$-\overline{u_i u_j} = \nu_t (\frac{\partial U_i}{\partial x^j} + \frac{\partial U_j}{\partial x^i}) - \frac{2}{3} \delta_{ij} k \tag{2.15}$$

where $k = (\overline{uu} + \overline{vv} + \overline{ww})/2$ is the turbulent kinetic energy and δ_{ij} is the Kronecker delta. The substitution of Reynolds stress into the momentum equations yields,

$$\frac{\partial U_i}{\partial t} + \sum_{j=1}^{3} [(U_i - \frac{\partial \nu_t}{\partial x^j}) \frac{\partial U_i}{\partial x^j} - \frac{\partial \nu_t}{\partial x^j} \frac{\partial U_j}{\partial x^i}] = -\frac{\delta_{i,3}}{Fr^2} + (\frac{\nu(\phi)}{\mathrm{Re}} + \nu_t) \nabla^2 U_i - (\frac{1}{\rho(\phi)} \frac{\partial p}{\partial x^i} + \frac{\partial (\frac{2}{3} k)}{\partial x^i}) \tag{2.16}$$

Let $\varphi = U_i$ and rearrange the momentum equations as follows,

$$\nabla^2 \varphi = R_\varphi \cdot [\sum_{j=1}^{3} (U_j - \frac{\partial \nu_t}{\partial x^j}) \frac{\partial \varphi}{\partial x^j} + \frac{\partial \varphi}{\partial t}] + s_\varphi \tag{2.17}$$

where the effective viscosity is $R_\varphi = (\frac{\nu(\phi)}{\mathrm{Re}} + \nu_t)^{-1}$ and the source terms are given by,

$$s_\varphi = R_\varphi [\frac{1}{\rho(\phi)} \frac{\partial p}{\partial x^i} + \frac{\partial (\frac{2}{3} k)}{\partial x^i} - \sum_{i=1}^{3} \frac{\partial \nu_t}{\partial x^j} \frac{\partial U_j}{\partial x^i} + \frac{\delta_{i,3}}{Fr^2}] \tag{2.18}$$

In curvilinear coordinate system, those terms can be rewritten in the transformed plane $\xi^i = (\xi, \eta, \zeta)$ as follows,

$$\begin{cases} \nabla^2 \varphi = \sum_i \sum_j g^{ij} \frac{\partial^2 \varphi}{\partial \xi^i \partial \xi^j} + \sum_j f^j \frac{\partial \varphi}{\partial \xi^j} \\ \frac{\partial \varphi}{\partial t} = \frac{\partial \varphi}{\partial \tau} - \frac{1}{J} \sum_i \sum_j b_i^{\ j} \frac{\partial x^i}{\partial \tau} \frac{\partial \varphi}{\partial \xi^j} \\ \sum_j U_j \frac{\partial \varphi}{\partial x^j} = \sum_i U_i (\frac{1}{J} \sum_j b_i^{\ j} \frac{\partial \varphi}{\partial \xi_j}) \\ -\frac{\partial \nu_t}{\partial x^j} \frac{\partial \varphi}{\partial x^j} = -\sum_n [\frac{1}{J} \sum_m b_n^{\ m} \frac{\partial \nu_t}{\partial \xi^m} \cdot \frac{1}{J} \sum_j b_n^{\ j} \frac{\partial \varphi}{\partial \xi^j}] \end{cases} \tag{2.19}$$

where $b_i^{\ j}, g^{ij}, f^j$ and the Jacobian J are geometric coefficients in curvilinear coordinate system whose values can be readily evaluated in the transformed plane. Plug these terms into equation (2.17), it can get,

$$\sum_i \sum_j g^{ij} \frac{\partial^2 \varphi}{\partial \xi^i \partial \xi^j} - \sum_j 2a_\varphi^{\ j} \frac{\partial \varphi}{\partial \xi^j} = R_\varphi \frac{\partial \varphi}{\partial \tau} + s_\varphi \tag{2.20}$$

where, $2a_\varphi^{\ j} = \frac{R_\varphi}{J} \sum_n b_n^{\ j} [U_n - \frac{\partial x_i}{\partial \tau} - \sum_m \frac{1}{J} b_n^{\ m} \frac{\partial \nu_t}{\partial \xi^m}] - f^i$

Note that,

$$\sum_i \sum_j g^{ij} \frac{\partial^2 \varphi}{\partial \xi^i \partial \xi^j} = g^{11} \frac{\partial^2 \varphi}{\partial \xi^1 \partial \xi^1} + g^{22} \frac{\partial^2 \varphi}{\partial \xi^2 \partial \xi^2} + g^{33} \frac{\partial^2 \varphi}{\partial \xi^3 \partial \xi^3} + 2(g^{12} \frac{\partial^2 \varphi}{\partial \xi^1 \partial \xi^2} + g^{23} \frac{\partial^2 \varphi}{\partial \xi^2 \partial \xi^3} + g^{31} \frac{\partial^2 \varphi}{\partial \xi^3 \partial \xi^1}) \tag{2.21}$$

Plugging it into equation (2.20), it can get

$$\sum_j (g^{jj} \frac{\partial^2 \varphi}{\partial \xi^j \partial \xi^j} - 2a_\varphi{}^j \frac{\partial \varphi}{\partial \xi^j}) = R_\varphi \frac{\partial \varphi}{\partial \tau} + S_\varphi \tag{2.22}$$

$$S_\varphi = s_\varphi - 2(g^{12} \frac{\partial^2 \varphi}{\partial \xi^1 \partial \xi^2} + g^{23} \frac{\partial^2 \varphi}{\partial \xi^2 \partial \xi^3} + g^{31} \frac{\partial^2 \varphi}{\partial \xi^3 \partial \xi^1}) \tag{2.23}$$

The momentum equation and the continuity equation are the Reynolds-Averaged Navier-Stokes (RANS) equation for unsteady, three-dimensional turbulent flows.

CHAPTER III

NUMERICAL METHOD

3.1 Introduction

This chapter presents the distinct numerical schemes for advection equations of the LS function and the VOF function. The LS function is a smooth and continuous function, the 3rd order Total Variation Diminishing (TVD) Runge-Kutta scheme is employed to discretize temporal derivative and the 5th order Weighted Essentially Non-Oscillatory (WENO) scheme is employed for spatial derivatives. Because the VOF function is discontinuous as a step function, using standard numerical scheme such as finite difference method can easily diffuse the interface. The VOF advection is performed using the PLIC interface reconstruction and the mixed Lagrangian and Eulerian advection scheme. Finally, the LS function is adjusted for mass conservation based on the reconstructed PLIC interface.

3.2 Level Set Equation

Equation (2.3) can be rewritten from the general curvilinear grid $x^i = (x^1, x^2, x^3)$ to the transformed grid $\xi^i = (\xi, \eta, \zeta)$ (figure 3.1) as following,

$$\frac{\partial \phi}{\partial t} + U\frac{\partial \phi}{\partial \xi} + V\frac{\partial \phi}{\partial \eta} + W\frac{\partial \phi}{\partial \zeta} = 0 \tag{3.1}$$

where $U^i = (U, V, W)$ are the contravariant velocity components in the transformed grid defined as,

$$U^i = \sum_{j=1}^{3} b_j^i U_j \tag{3.2}$$

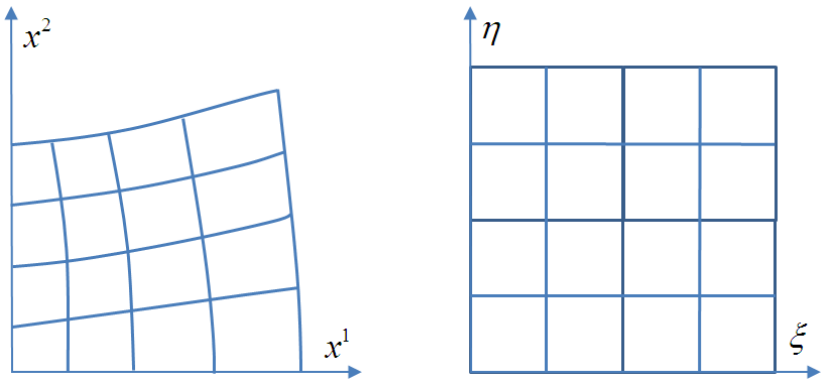

(a) General curvilinear grid (b) Transformed grid

Figure 3.1: General curvilinear grid and transformed grid

In the present study, equation (3.1) is advanced in time using the 3rd order TVD Runge-Kutta scheme which is total variation stable,

$$\begin{cases} \phi^{(1)} = \phi^{(n)} - \Delta\tau \cdot R(\phi^{(n)}) \\ \phi^{(2)} = \frac{3}{4}\phi^{(n)} + \frac{1}{4}\phi^{(1)} - \frac{\Delta\tau}{4} \cdot R(\phi^{(1)}) \\ \phi^{(n+1)} = \frac{1}{3}\phi^{(n)} + \frac{2}{3}\phi^{(2)} - \frac{2\Delta\tau}{3} \cdot R(\phi^{(2)}) \end{cases} \tag{3.3}$$

where $R(\phi) = U^i \cdot \dfrac{\partial \phi}{\partial \xi^i}$ is the spatial operator.

To improve the accuracy of the spatial discretization, the 5th order Hamilton-Jacobi Weighted Essentially Non-oscillatory (HJ-WENO) scheme is adopted to evaluate the spatial operator $R(\phi)$ [32].

Firstly considering the properties of upwind difference scheme, the spatial term is addressed as below,

If $U^i < 0$, we define $(\phi_\xi)_i = D^- \phi_i = \dfrac{\phi_i - \phi_{i-1}}{\Delta\xi}$

If $U^i > 0$, we define $(\phi_\xi)_i = D^+ \phi_i = \dfrac{\phi_{i+1} - \phi_i}{\Delta\xi}$

If $U^i = 0$, this term vanishes

where $(\phi_\xi)_i$ denotes the spatial derivative of ϕ with respect to ξ.

WENO method chooses a convex combination of the three ENO approximations. Since it reduces the errors by more than an order of magnitude over the 3rd order accurate ENO scheme, WENO scheme is useful for solving level set equation to increase the accuracy.

In the 3rd order accurate HJ-ENO scheme, the spatial derivative $(\phi_\xi^-)_i$ is approximated by one of the following three upwind discretizations,

$$\begin{cases} \phi^1{}_\xi = \dfrac{v_1}{3} - \dfrac{7v_2}{6} + \dfrac{11v_3}{6} \\ \phi^2{}_\xi = -\dfrac{v_2}{6} + \dfrac{5v_3}{6} + \dfrac{v_4}{3} \\ \phi^3{}_\xi = \dfrac{v_3}{3} + \dfrac{5v_4}{6} - \dfrac{v_5}{6} \end{cases} \tag{3.4}$$

where $v_1 = D^- \phi_{i-2}, v_2 = D^- \phi_{i-1}, v_3 = D^- \phi_i, v_4 = D^- \phi_{i+1}, v_5 = D^- \phi_{i+2}$.

The WENO approximation of $(\phi_\xi^-)_i$ is a convex combination given by,

$$\phi_\xi = \omega_1 \phi_\xi{}^1 + \omega_2 \phi_\xi{}^2 + \omega_3 \phi_\xi{}^3 \tag{3.5}$$

where $0 \le w_1, w_2, w_3 \le 1$, and $\omega_1 + \omega_3 + \omega_3 = 1$.

In smooth region, these three weight coefficients are equally significant. To the contrary, the weight coefficient values are evaluated in non-smooth region. In order to define the weights, the smoothness of the stencils are estimated as below,

$$\begin{cases} S_1 = \frac{13}{12}(v_1 - 2v_2 + v_3)^2 + \frac{1}{4}(v_1 - 4v_2 + 3v_3)^2 \\ S_2 = \frac{13}{12}(v_2 - 2v_3 + v_4)^2 + \frac{1}{4}(v_2 - 4v_4)^2 \\ S_3 = \frac{13}{12}(v_3 - 2v_4 + v_5)^2 + \frac{1}{4}(3v_3 - 4v_4 + v_5)^2 \end{cases} \tag{3.6}$$

Using these smoothness estimates,

$$\begin{cases} \alpha_1 = \frac{0.1}{(S_1 + \varepsilon)^2} \\ \alpha_2 = \frac{0.6}{(S_2 + \varepsilon)^2} \\ \alpha_3 = \frac{0.3}{(S_3 + \varepsilon)^2} \end{cases} \tag{3.7}$$

with $\varepsilon = 10^{-6}$. Finally, the weights are as follows,

$$\begin{cases} \omega_1 = \frac{\alpha_1}{\alpha_1 + \alpha_2 + \alpha_3} \\ \omega_2 = \frac{\alpha_2}{\alpha_1 + \alpha_2 + \alpha_3} \\ \omega_3 = \frac{\alpha_3}{\alpha_1 + \alpha_2 + \alpha_3} \end{cases} \tag{3.8}$$

Thus, the (ϕ_ξ^-) throughout the domain can be computed.

The derivative $(\phi_{\xi}^{+})_i$ is constructed with a subset of $\{\phi_{i-2}, \phi_{i-1}, \phi_i, \phi_{i+1}, \phi_{i+2}, \phi_{i+3}\}$, defining $v_1 = D^{+}\phi_{i+2}, v_2 = D^{+}\phi_{i+1}, v_3 = D^{+}\phi_i, v_4 = D^{+}\phi_{i-1}, v_5 = D^{+}\phi_{i-2}$.

3.3 VOF Equation

Equation (2.8) can be rewritten from the general curvilinear grid $x^i = (x^1, x^2, x^3)$ to the transformed grid $\xi^i = (\xi, \eta, \zeta)$ as following,

$$\frac{\partial (JC)}{\partial t} + (JU)\frac{\partial C}{\partial \xi} + (JV)\frac{\partial C}{\partial \eta} + (JW)\frac{\partial C}{\partial \zeta} = 0 \tag{3.9}$$

where J is the Jacobian of transformation from the physical domain to the transformed domain and J represents the physical volume for each computational cell; $U^i = (U, V, W)$ are the contravariant velocity components defined in equation (3.2).

3.3.1 Interface reconstruction algorithm

The key part of interface reconstruction is to determine the orientation of the interface segments in every cut cell. An explicit expression by Gueyffier et al. (1999) [33] is employed. The interface is represented by a plane in 3D case as following.

$$m_1 x_1 + m_2 x_2 + m_3 x_3 = \alpha \tag{3.10}$$

where α is a parameter which indicates the shortest distance from the origin to the plane, and the normal vector $\vec{m} = (m_1, m_2, m_3)$ can be obtained from the LS function in equation (1.6) in the CLSVOF method.

Every interface segment can be reconstructed in the transformed grid $\xi^i = (\xi, \eta, \zeta)$ in this study. Equation (3.10) in transformed grid is as following,

$$m_1\xi + m_2\eta + m_3\zeta = \alpha \tag{3.11}$$

Figure 3.2 illustrates the reconstructed interface in 2D and 3D cases. The shaded area represents the "cut area" in 2D case and the "cut volume" in 3D case under certain reconstructed interface.

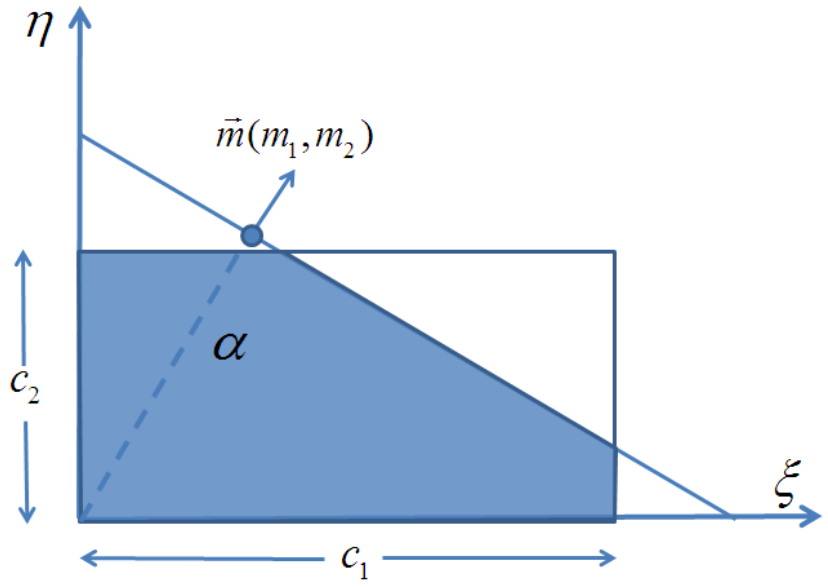

(a) 2D reconstructed plane and the cut area under the plane

Figure 3.2: 2D and 3D reconstructed interface

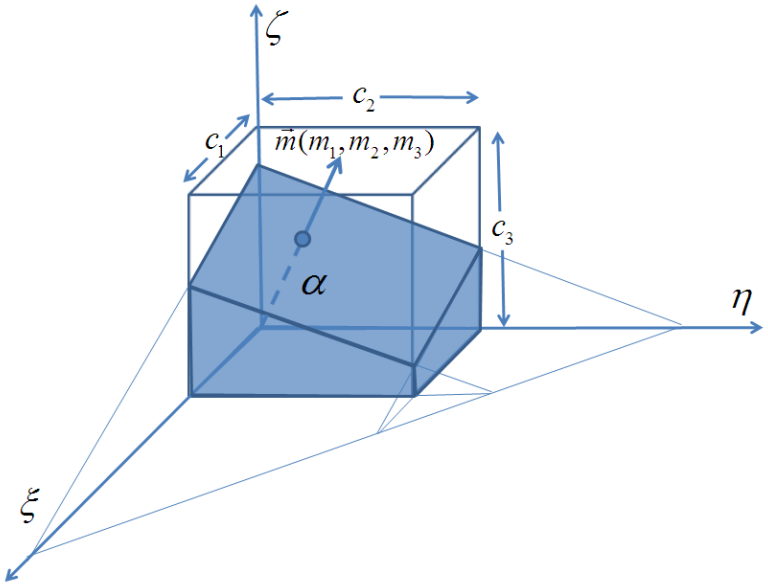

(b) 3D reconstructed plane and the cut volume under the plane

Figure 3.2: (Continued)

On the one hand, the "forward" problem of finding the cut volume, VL, under certain interface orientation within the cell spacing (c_1, c_2, c_3) in figure 3.2 (b) is given below,

$$VL = \frac{1}{6|m_1 m_2 m_3|}[\alpha^3 - \sum_{j=1}^{3} H(\alpha - |m_j| c_j)(\alpha - |m_j| c_j)^3 + \sum_{j=1}^{3} H(\alpha - \alpha_{MAX} + |m_j| c_j)(\alpha - \alpha_{MAX} + |m_j| c_j)^3] \quad (3.12)$$

where $\alpha_{MAX} = |m_1| c_1 + |m_2| c_2 + |m_3| c_3$, and $H(x) = \begin{cases} 0 & for\ x < 0 \\ 1 & for\ x > 0 \end{cases}$.

The above expression is only valid when all three components of the normal $\vec{m} = (m_1, m_2, m_3)$ are nonzero. In this study, the expressions for the other possibilities (the normal components could be zero) are also included.

When only one component of the normal vector is zero, the expression of the volume is reduced to the expression of the 2D area in figure 3.2 (a) multiplied by the "thickness",

$$VL = \frac{1}{2|m_1 m_2|}[\alpha^2 - \sum_{j=1}^{2} H(\alpha - |m_j| c_j)(\alpha - |m_j| c_j)^2] \times c_3 \tag{3.13}$$

where the third component of normal vector m_3 is zero in this case.

Furthermore, when only one component of normal vector is nonzero, the volume is straightforward to compute volume of a cube,

$$VL = \alpha \times c_1 \times c_2 \tag{3.14}$$

where only the third component of normal vector m_3 is nonzero value in this case.

On the other hand, because the relation between *VL* and α is one-to-one, the "inverse" problem of determining the parameter α given a cut volume and normal direction $\vec{m} = (m_1, m_2, m_3)$ in a computational cell can be solved using a standard root-finding approach. In this study, the Brent's method [34] is employed to find the polynomial root. In general, both the "forward" and "inverse" problems are needed in the reconstruction step and the following advection step.

3.3.2 Interface advection algorithm

A mixed split Eulerian implicit-Lagrangian explicit (EI-LE) scheme was presented by Scardovelli and Zaleski, which can conserve the mass to machine error under the discrete divergence-free velocity field [15], [35]. The original advection scheme is 1st order accurate in time and fails to preserve mass conservation when the velocity field is not exactly discrete divergence-free. In this study, the scheme is extended to the transformed plane which can be applied for the general curvilinear grids. The 2nd order Runge-Kutta scheme is used to improve numerical accuracy. Moreover, an extra volume-correction scheme is added to preserve the mass conservation for incompressible flow field [36].

Firstly, the 2nd order Runge-Kutta scheme in this study is described. It is assumed that any particle within a cell is moving only along x direction in figure 3.3, and the velocity is only the function of x. It indicates, any vertical face is moving as a whole without deformation. The mathematical model is,

$$\frac{dx}{dt} = U(x,t) \tag{3.15}$$

with the initial conditions,

$$\begin{cases} U(0,t^n) = U_1 \\ U(\Delta x,t^n) = U_2 \end{cases}$$

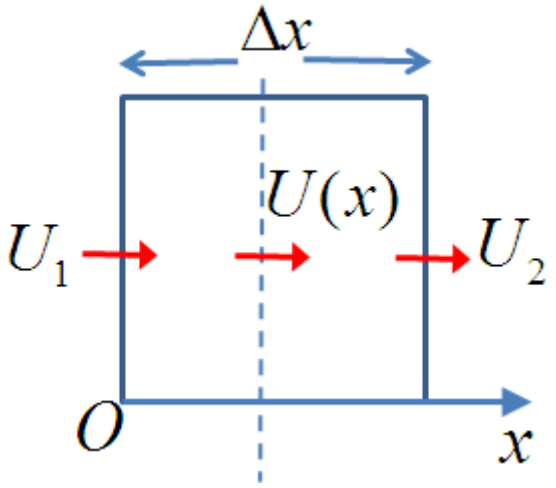

Figure 3.3: Schematic diagram of 2nd order Runge-Kutta method

The goal is to update the position x^n to the new time x^{n+1} with the time increment Δt. The velocity $U(x^n, t^n)$ within the cell is the linear interpolation of boundary conditions U_1 and U_2,

$$U(x^n, t^n) = \frac{U_2 - U_1}{\Delta x} x^n + U_1 = Ax^n + B \tag{3.16}$$

with $A = \frac{U_2 - U_1}{\Delta x}$,and $B = U_1$.

For 1st order Runge-Kutta scheme,

$$x^{n+1} = x^n + U(x^n, t^n)\Delta t = x^n(1 + A\Delta t) + B\Delta t \tag{3.17}$$

$$Dis = x^{n+1} - x^n = x^n A\Delta t + B\Delta t = U(x^n, t^n)\Delta t \tag{3.18}$$

For 2nd order Runge-Kutta scheme,

$$x^{n+1} = x^n + \Delta t(\frac{1}{2}K_1 + \frac{1}{2}K_2) \tag{3.19}$$

in which,

$$K_1 = U(x^n, t^n) = Ax^n + B$$

$$K_2 = U(x^n + \Delta t K_1, t^n + \Delta t)$$

Expanding K_2 by Taylor Series,

$$K_2 = U(x^n, t^n) + \Delta t A K_1 + O(\Delta t^2)$$

Thus,

$$x^{n+1} = x^n + U(x^n, t^n)\Delta t + \frac{1}{2}U(x^n, t^n)A\Delta t^2 + O(\Delta t^3) \tag{3.20}$$

$$Dis = x^{n+1} - x^n = U(x^n, t^n)\Delta t + \frac{1}{2}U(x^n, t^n)A\Delta t^2 \tag{3.21}$$

Similarly, the position x^n can date back to the old x^{n-1} with the same time increment Δt.

For 1st order Runge-Kutta scheme,

$$x^{n-1} = x^n - U(x^n, t^n)\Delta t = x^n(1 - A\Delta t) - B\Delta t \tag{3.22}$$

$$Dis = x^n - x^{n-1} = x^n A\Delta t + B\Delta t = U(x^n, t^n)\Delta t \tag{3.23}$$

For 2nd order Runge-Kutta scheme,

$$x^{n-1} = x^n - \Delta t(\frac{1}{2}K_1 + \frac{1}{2}K_2)$$

in which,

$$K_1 = U(x^n, t^n) = Ax^n + B$$

$$K_2 = U(x^n - \Delta t K_1, t^n - \Delta t)$$

$$x^{n-1} = x^n - U(x^n, t^n)\Delta t + \frac{1}{2}U(x^n, t^n)A\Delta t^2 + O(\Delta t^3) \tag{3.24}$$

$$Dis = x^n - x^{n-1} = U(x^n, t^n)\Delta t - \frac{1}{2}U(x^n, t^n)A\Delta t^2 \tag{3.25}$$

A mixed EI-LE scheme for a two-dimensional case is to combine an Eulerian step along one direction followed by a Lagrangian step in the other direction on the basis of split technique to propagate the interface separately.

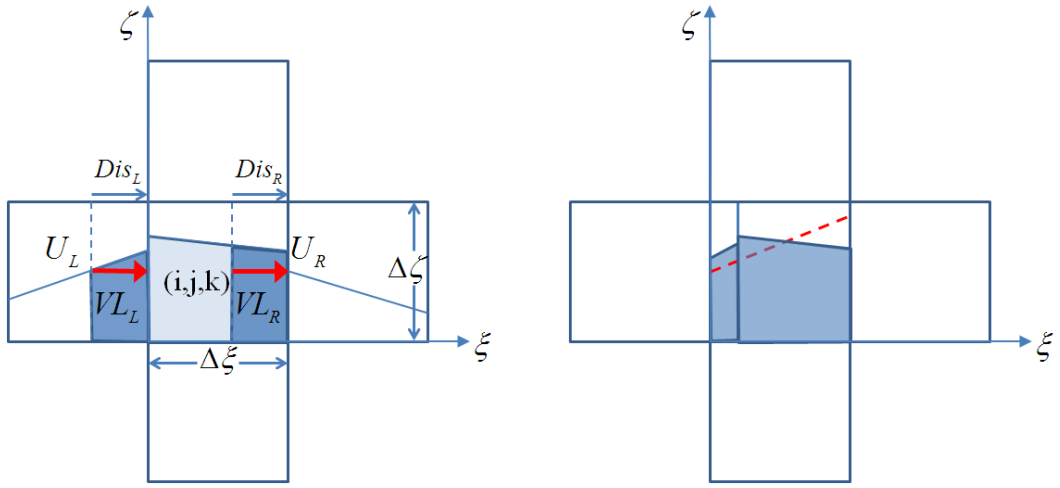

(a) Geometrical EI scheme (b) Remapped and reconstructed

Figure 3.4: 2D EI-LE interface advection scheme

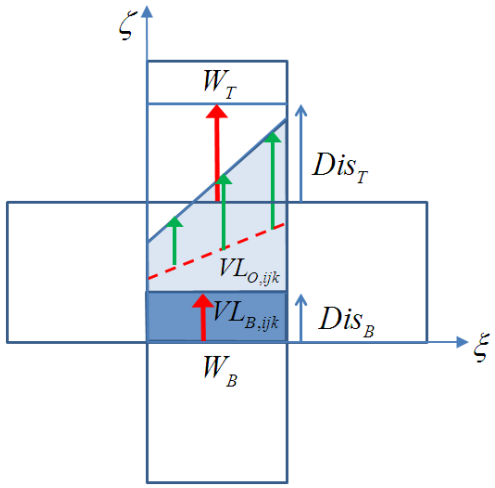

(c) Geometrical LE scheme

Figure 3.4: (Continued)

Take the EI-LE scheme in the ξ–ζ plane as an example. During one time step from t^n to t^{n+1}, the interface within the cell (i, j, k) is first propagating along ξ direction by the EI scheme in figure 3.4(a). The mono-dimensional version of equation (3.9) along ξ direction is as following,

$$\frac{\partial (JC)}{\partial t} + (JU)\frac{\partial C}{\partial \xi} = 0 \tag{3.26}$$

$$\Longrightarrow \quad \frac{\partial (JC)}{\partial t} + \frac{\partial (JUC)}{\partial \xi} = C\frac{\partial (JU)}{\partial \xi} \tag{3.27}$$

A simple finite difference scheme in time and in space can discretize equation (3.27).

$$\Longrightarrow \quad \frac{(JC^*)_{ijk} - (JC^n)_{ijk}}{\Delta t} + \frac{J_{(i+1/2)jk}U_{(i+1/2)jk}C_{(i+1/2)jk} - J_{(i-1/2)jk}U_{(i-1/2)jk}C_{(i-1/2)jk}}{\Delta \xi_{ijk}}$$
$$= C^*_{ijk}\frac{J_{(i+1/2)jk}U_{(i+1/2)jk} - J_{(i-1/2)jk}U_{(i-1/2)jk}}{\Delta \xi_{ijk}}$$

$$\Longrightarrow \quad \begin{aligned} & C^*_{ijk}(J_{ijk} - \frac{J_{(i+1/2)jk}U_{(i+1/2)jk}\Delta t}{\Delta\xi_{ijk}} + \frac{J_{(i-1/2)jk}U_{(i-1/2)jk}\Delta t}{\Delta\xi_{ijk}}) = \\ & J_{ijk}C^n_{ijk} - \frac{J_{(i+1/2)jk}U_{(i+1/2)jk}\Delta tC_{(i+1/2)jk}}{\Delta\xi_{ijk}} + \frac{J_{(i-1/2)jk}U_{(i-1/2)jk}\Delta tC_{(i-1/2)jk}}{\Delta\xi_{ijk}} \end{aligned} \tag{3.28}$$

Some simplifications for the terms in equation (3.28) are made as below,

$$\frac{J_{(i+1/2)jk}U_{(i+1/2)jk}\Delta tC_{(i+1/2)jk}}{\Delta\xi_{ijk}} = \frac{J_{(i+1/2)jk}U_{(i+1/2)jk}(\Delta\eta\Delta\zeta)_{ijk}\Delta tC_{(i+1/2)jk}}{(\Delta\xi\Delta\eta\Delta\zeta)_{ijk}} = \frac{VL_{L,ijk}}{(\Delta\xi\Delta\eta\Delta\zeta)_{ijk}} \tag{3.29}$$

$$\frac{J_{(i-1/2)jk}U_{(i-1/2)jk}\Delta tC_{(i-1/2)jk}}{\Delta\xi_{ijk}} = \frac{J_{(i-1/2)jk}U_{(i-1/2)jk}(\Delta\eta\Delta\zeta)_{ijk}\Delta tC_{(i-1/2)jk}}{(\Delta\xi\Delta\eta\Delta\zeta)_{ijk}} = \frac{VL_{R,ijk}}{(\Delta\xi\Delta\eta\Delta\zeta)_{ijk}} \tag{3.30}$$

$$\frac{J_{(i-1/2)jk}U_{(i-1/2)jk}}{J_{ijk}} = U_L \tag{3.31}$$

$$\frac{J_{(i+1/2)jk}U_{(i+1/2)jk}}{J_{ijk}} = U_R \tag{3.32}$$

where VL_L and VL_R represent the liquid volume across the left and the right faces, respectively; U_R and U_L are the velocities on the left and the right faces, respectively.

The intermediate VOF function, C^*_{ijk}, after 1D advection along ξ direction is obtained,

$$\Longrightarrow \quad C^*_{ijk} = \frac{J_{ijk}C^n_{ijk} + VL_{L,ijk}/(\Delta\xi\Delta\eta\Delta\zeta)_{ijk} - VL_{R,ijk}/(\Delta\xi\Delta\eta\Delta\zeta)_{ijk}}{J_{ijk}(1 + Dis_{L,ijk}/\Delta\xi_{ijk} - Dis_{R,ijk}/\Delta\xi_{ijk})} \tag{3.33}$$

where Dis_L and Dis_R are the travelling distances for the liquid through left and right faces during the time increment $\Delta t = t^{n+1} - t^n$. In the original version, the distance travelled through any face is 1st order in time by equation (3.23),

$$\begin{cases} Dis_L = U_L \Delta t \\ Dis_R = U_R \Delta t \end{cases} \tag{3.34}$$

In the present study, the 2nd order Runge-Kutta method in equation (3.25) is used to evaluate the distance travelled during the time increment. Therefore, the acceleration of the velocity is accounted for implicitly.

$$\begin{cases} Dis_L = U_L \Delta t - 0.5 U_L \Delta t^2 A \\ Dis_R = U_R \Delta t - 0.5 U_R \Delta t^2 A \end{cases} ; A = \frac{U_R - U_L}{\Delta \xi} \tag{3.35}$$

After propagating in ξ direction by the EI scheme, the VOF function is updated to an intermediate level, and the related normal vector $\vec{m} = (m_1^*, m_2^*, m_3^*)$ is also updated by the LS function at the same intermediate level. Another interface reconstruction procedure is employed to obtain the new orientation of the interface in the cell at the intermediate level t^* in figure 3.4(b).

$$m_1^* \xi^* + m_2^* \eta^* + m_3^* \zeta^* = \alpha^* \tag{3.36}$$

The following step is advection along ζ direction by the LE scheme in figure 3.4(c). The velocity component $W_{ijk}^*(\zeta)$ along ζ direction, within the cell, is a simple linear interpolation,

$$W(x_3^*) = \frac{W_T - W_B}{\Delta \zeta} x_3^* + W_B \tag{3.37}$$

Then the ζ coordinate of each point on the interface at the intermediate level is updated to the new time level t^{**} after one application EI-LE scheme. The new position is updated in 1st order Runge-Kutta scheme in equation (3.18) as following,

$$\zeta^{**} = \zeta^{*} + W(\zeta^{*})\Delta t = (1 + \frac{W_T - W_B}{\Delta\zeta}\Delta t)\zeta^{*} + W_B \Delta t \tag{3.38}$$

$$\Longrightarrow \quad \zeta^{*} = \frac{\zeta^{**} - W_B \Delta t}{1 + \frac{W_T - W_B}{\Delta\zeta}\Delta t} \tag{3.39}$$

The ξ^{*} and η^{*} coordinates remain constant. Upon substituting ζ^{*} into equation (3.36), the updated interface equation after LE scheme along ζ direction is,

$$m_1^{*}\xi^{*} + m_2^{*}\eta^{*} + m_3^{*}\frac{\zeta^{**} - W_B \Delta t}{1 + \frac{W_T - W_B}{\Delta\zeta}\Delta t} = \alpha^{*} \tag{3.40}$$

Equation (3.40) can be written in the standard form at the time level t^{**},

$$m_1^{**}\xi^{**} + m_2^{**}\eta^{**} + m_3^{**}\zeta^{**} = \alpha^{**} \tag{3.41}$$

in which,

$$m_3^{**} = \frac{m_3^{*}}{1 + \frac{W_T - W_B}{\Delta\zeta}\Delta t},$$

$$\alpha^{**} = \alpha^{*} + \frac{m_3^{*} W_B \Delta t}{1 + \frac{W_T - W_B}{\Delta\zeta}\Delta t},$$

while the other variables with superscript (**) in equation (3.41) remain the same with their old values with superscript (*).

Also, the 2nd order Runge-Kutta scheme can be used to update the new position by equation (3.21). The interface equation at the time level t^{**} is,

$$m_1^{**}\xi^{**} + m_2^{**}\eta^{**} + m_3^{**}\zeta^{**} = \alpha^{**} \tag{3.42}$$

in which,

$$m_3^{**} = \frac{m_3^*}{1 + \frac{W_T - W_B}{\Delta\zeta}\Delta t + \frac{1}{2}(\frac{W_T - W_B}{\Delta\zeta}\Delta t)^2}$$

$$\alpha^{**} = \alpha^* + \frac{m_3^*[\frac{1}{2}\frac{W_T - W_B}{\Delta\zeta}W_B(\Delta t)^2 + W_B\Delta t]}{1 + \frac{W_T - W_B}{\Delta\zeta}\Delta t + \frac{1}{2}(\frac{W_T - W_B}{\Delta\zeta}\Delta t)^2}$$

while the other variables with superscript (**) in equation (3.42) remain the same with their old values with superscript (*).

Similar with equation (3.34) and equation (3.35), the corresponding distances Dis_T and Dis_B for top and bottom faces can be updated explicitly as,

1st order in time

$$\begin{cases} Dis_B = W_B\Delta t \\ Dis_T = W_T\Delta t \end{cases} \tag{3.43}$$

2nd order in time

$$\begin{cases} Dis_B = W_B\Delta t + 0.5W_B\Delta t^2 B \\ Dis_T = W_T\Delta t + 0.5W_T\Delta t^2 B \end{cases} ; \quad B = \frac{W_T - W_B}{\Delta\zeta} \tag{3.44}$$

After Lagrangian advection, the interface might protrude into the neighboring cells. Similarly, the interface which belongs to the neighboring cells might also enter the present cell. The portion of the liquid volume that remains in the original cell are defined as VL_O; the liquid volumes from top and bottom neighboring cells to enter the current cell are defined as VL_T, VL_B. The VOF function after one application of the EI-LE scheme in ξ–ζ plane is C_{ijk}^{**},

$$C_{ijk}^{**} = \frac{VL_{O,ijk} + VL_{B,ijk} + VL_{T,ijk}}{J_{ijk}(\Delta\xi\Delta\eta\Delta\zeta)_{ijk}} \tag{3.45}$$

This 2D EI-LE scheme can preserve the exact volume conservation under the divergence-free velocity. The total volume can be checked analytically after one application of the EI-LE scheme.

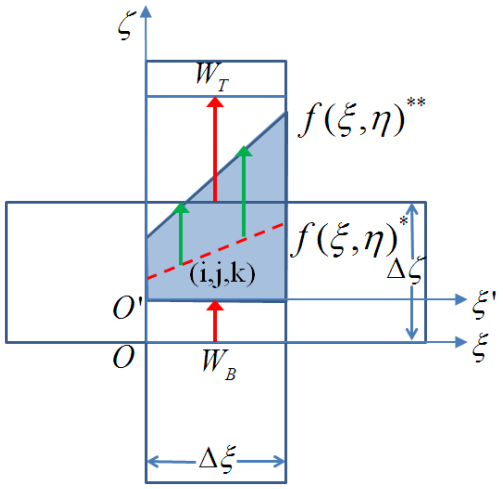

Figure 3.5: Volume integration after LE scheme

After the first EI part, the volume in the cell (i, j, k) is VL_{ijk}^{*},

$$VL_{ijk}^{*} = J_{ijk}(\Delta\xi\Delta\eta\Delta\zeta)_{ijk} \times C_{ijk}^{*} = \frac{J_{ijk}(\Delta\xi\Delta\eta\Delta\zeta)_{ijk} C_{ijk}^{n} + VL_{L,ijk} - VL_{R,ijk}}{1 + Dis_{L,ijk} / \Delta\xi_{ijk} - Dis_{R,ijk} / \Delta\xi_{ijk}} \tag{3.46}$$

After that, another new PLIC is reconstructed as the red dashed line in figure 3.5. It is assumed that $f(\xi,\eta)^{*}$ is the elevation of current interface relative to the origin O, along ζ direction in the function of ξ and η. There is another expression for VL_{ijk}^{*},

$$VL^{*}_{ijk} = J_{ijk} \int_{0}^{\Delta\xi} \int_{0}^{\Delta\eta} f(\xi,\eta)^{*} d\eta d\xi \tag{3.47}$$

And then the segment within the cell is moved to the new position in Lagrangian manner. The elevation of the new interface to new origin *O'* is,

$$f(\xi,\eta)^{**} = f(\xi,\eta)^{*}(1 + Dis_T / \Delta\zeta - Dis_B / \Delta\zeta) \tag{3.48}$$

where Dis_B and Dis_T are specified in equation (3.43).

In the end, the final deformed volume originated from the cell (i, j, k) is VL^{**}_{ijk},

$$\begin{aligned} VL^{**}_{ijk} &= J_{ijk} \int_{0}^{\Delta\xi} \int_{0}^{\Delta\eta} f(\xi,\eta)^{**} d\eta d\xi \\ &= J_{ijk}(1 + Dis_T / \Delta\zeta - Dis_B / \Delta\zeta) \int_{0}^{\Delta\xi} \int_{0}^{\Delta\eta} f(\xi,\eta)^{*} d\eta d\xi \\ &= (1 + Dis_T / \Delta\zeta - Dis_B / \Delta\zeta) \times VL^{*}_{ijk} \\ &= (VL^{n}_{ijk} + VL_{L,ijk} - VL_{R,ijk}) \frac{(1 + Dis_{T,ijk} / \Delta\zeta_{ijk} - Dis_{B,ijk} / \Delta\zeta_{ijk})}{(1 + Dis_{L,ijk} / \Delta\xi_{ijk} - Dis_{R,ijk} / \Delta\xi_{ijk})} \end{aligned} \tag{3.49}$$

The 2D discrete divergence-free flow condition is,

$$\frac{(U_{R,ijk} - U_{L,ijk})}{\Delta\xi_{ijk}} + \frac{(W_{T,ijk} - W_{B,ijk})}{\Delta\zeta_{ijk}} = 0 \tag{3.50}$$

If the 1st order travelling distances are used in equation (3.34) and equation (3.43), equation (3.50) leads to,

$$\frac{(1 + Dis_{T,ijk} / \Delta\zeta_{ijk} - Dis_{B,ijk} / \Delta\zeta_{ijk})}{(1 + Dis_{L,ijk} / \Delta\xi_{ijk} - Dis_{R,ijk} / \Delta\xi_{ijk})} = 1 \tag{3.51}$$

Finally, the final deformed volume originated from the cell (i, j, k) is,

$$VL^{**}_{ijk} = (VL^{n}_{ijk} + VL_{L,ijk} - VL_{R,ijk}) \tag{3.52}$$

It is assumed that the flow cannot move out of the domain and there is not any source or sink flow over the domain. The total volume $\sum_{ijk=1}^{MAX} VL_{ijk}^{**}$ after one-time EI-LE scheme application is identical to the total volume $\sum_{ijk=1}^{MAX} VL_{ijk}^{n}$ before one-time EI-LE scheme application, due to the fact that the liquid volumes VL_L and VL_R through every face are balanced out among neighboring cells. The volume conservation indicates the mass conservation for an incompressible flow.

However, there exist some possibilities that the original EI-LE scheme cannot preserve the mass. For instance, the velocity obtained from the numerical flow solver may not be able to achieve exact discrete divergence-free condition in equation (3.50), due to discretization or iteration errors. Also, if the 2nd order travelling distances in equation (3.35) and equation (3.44) are used, $\frac{(1+Dis_{T,ijk}/\Delta\zeta_{ijk}-Dis_{B,ijk}/\Delta\zeta_{ijk})}{(1+Dis_{L,ijk}/\Delta\xi_{ijk}-Dis_{R,ijk}/\Delta\xi_{ijk})}$ is not always equal to one.

To preserve exact mass conservation, an extra term called 1st volume-correction term is incorporated in the present study to maintain the mass conservation.

$$VL_{ijk}^{**} = (1+Dis_{T,ijk}/\Delta\zeta_{ijk}-Dis_{B,ijk}/\Delta\zeta_{ijk}+\varepsilon)\times VL_{ijk}^{*} \tag{3.53}$$

where $\varepsilon = Dis_{B,ijk}/\Delta\zeta_{ijk}-Dis_{T,ijk}/\Delta\zeta_{ijk}+Dis_{L,ijk}/\Delta\xi_{ijk}-Dis_{R,ijk}/\Delta\xi_{ijk}$.

The 1st volume-correction term $\varepsilon\times VL_{ijk}^{*}$ exists in every cell within the domain. The summation of the 1st volume-correction over the domain can be collected and redistributed to the cut cells in the domain. More precisely, the domain can be divided

into pieces of region; every region has its own volume-correction summation which is only redistributed to the cut cells within its domain.

Furthermore, this scheme can also be extended to three-dimensional applications by designing three new velocity fields, $(U_1, V_1, 0)$, $(0, V_2, W_1)$, and $(U_2, 0, W_2)$. Therefore, the interface advection goes through the EI-LE scheme three times within each time step. It is desirable that each sub velocity field is discrete divergence free if the original EI-LE scheme is used [29]. After using the 1st volume-correction term, the three new sub-velocity fields in 3D are not required to be incompressible. Generally, the velocity field can be divided equally into $(0.5U, 0.5V, 0)$, $(0, 0.5V, 0.5W)$, and $(0.5U, 0, 0.5W)$. After going through EI-LE scheme under the three velocity fields above, the VOF function is fully updated to new time level. It is desirable to alternate the sequence of the three velocity field to remove possible asymmetries.

3.3.3 LS re-distance algorithm

In the CLSVOF method, the coupling between the LS function and the VOF function happens when computing the normal of the reconstructed interface and also when adjusting the LS function with the exact signed distance to the reconstructed interface. The LS function is required to adjust by the reconstructed interface for mass conservation. Many researchers have proposed different re-distance algorithms, which are mainly dealing with the 2D cases (Bourlioux [37]; Sussman and Puckett [30]; Son and Hur [38]; Son [39]; Menard, Tanguy and Berlemont [40]). Among these algorithms, the schemes by Son and Hur can be extended to 3D cases. However, the procedures are

complicated because of considering every possible interface configuration. In addition, all of the above algorithms are either based on structured Cartesian grids or 2D triangular and 3D tetrahedral grids [41]. Wang et al. proposed another new re-distance algorithm which can simplify the procedure and also can be extended to a general structured grid [42], [43]. In this study, the re-distance algorithm of Wang et al. in transformed grid is adopted. Another straightforward and robust scheme to transform the LS function, from the transformed grid to the physical grid, is developed.

The first task of the re-distance algorithm is to evaluate the LS function based on the reconstructed interface in the transformed grid. It includes two steps: determination of the sign of the LS function; evaluation of the magnitude of the LS function.

In the first step, the sign of the LS function S^{ϕ} is defined as,

$$S^{\phi} = sign(C - 0.5) = \begin{cases} 1 & 0.5 \le C \le 1 \\ -1 & 0 \le C < 0.5 \end{cases} \tag{3.54}$$

It is because that the PLIC interface is employed. For the VOF function greater than 0.5, the cell center falls inside the liquid phase where the LS function is positive; for the VOF function less than 0.5, the cell center stays in the air phase where the LS function is negative.

The second step is to determine the magnitude of the LS function, which is the most important and complicated step of the whole re-distance algorithm. All of the re-distance algorithms have their particular ways in this step. All in all, the basic principle is to find the closest point T, $\vec{x}_T = (\xi_T, \eta_T, \zeta_T)$, in a cut cell to the neighboring cell center.

Take two adjoining cells (i, j, k) and (i', j', k') as an instance. The closest point on the boundary of cell (i, j, k) to the center of cell (i', j', k') is either at the corner or at the face centroid of the cell (i, j, k). If the cell (i, j, k) contains an interface segment, the closest point on the segment to the cell center of (i', j', k') is also considered. For 2D case, the closest point on the segment will be either one of the two endpoints or the projection point of the cell (i', j', k') center, which depends on the location of the projection point. For 3D case, the reconstructed interface inside the cell is an n-sided $(3 \le n \le 6)$ polygon. The possible closest point on the interface can be the projection point of the cell (i', j', k') center to the interface, one of the vertices, or the projection point of the cell (i', j', k') center to one polygon side.

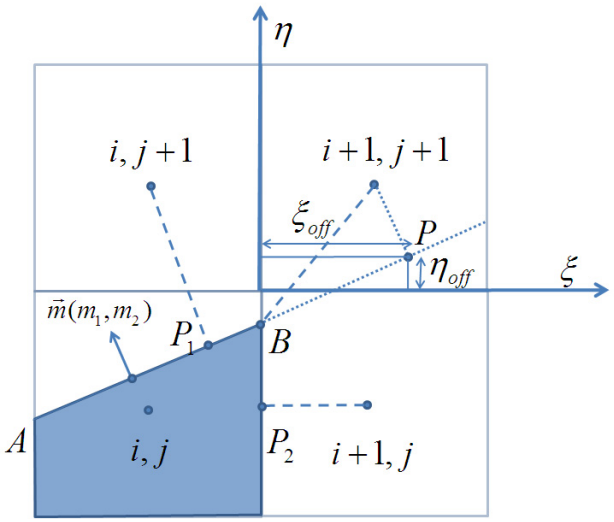

(a) The LS function re-distance in 2D case

Figure 3.6: Schematic diagram for the LS function re-distance

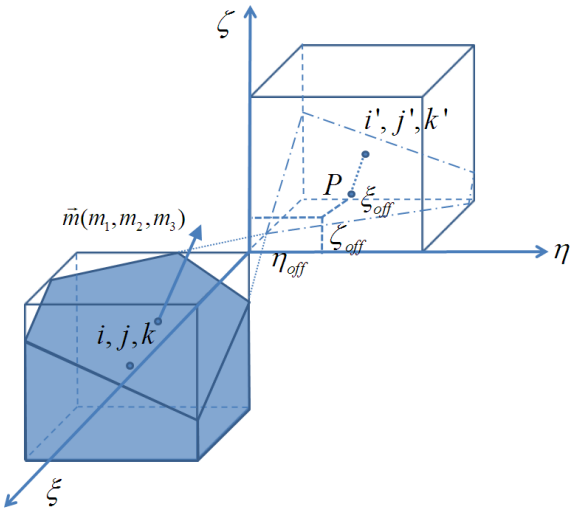

(b) The LS function re-distance in 3D case

Figure 3.6: (Continued)

In figure 3.6, for a given cell (i, j, k) with a reconstructed interface segment and any its neighbor cell (i', j', k') in the region where $|i'-i| \le K, |j'-j| \le K, |k'-k| \le K$ and K is the thickness of this region:

(1) The closest point V on the cell boundary of the cell (i, j, k) is considered first. The candidates are the face controid or the corner of the cell (i, j, k). The coordinates of point V is $\vec{x}_V = (\xi_V, \eta_V, \zeta_V)$,

$$\begin{cases} \xi_V = \xi_{i+l/2} \\ \eta_V = \eta_{j+m/2} \\ \zeta_V = \zeta_{k+n/2} \end{cases} \quad \text{where} \begin{cases} l = \max(-1, \min(1, i'-i)) \\ m = \max(-1, \min(1, j'-j)) \\ n = \max(-1, \min(1, k'-k)) \end{cases} \tag{3.55}$$

Point V is the closest point on the cell boundary of the cell (i, j, k) to the cell (i', j', k') but the distance from point V to cell center (i', j', k') may not be the magnitude of the local LS function.

If $D(\vec{x}_V) \times S^{\phi}_{i',j',k'} < 0$, the point V is the closest point to the cell (i', j', k').

$$D(\vec{x}_V) = \alpha - (m_1 \xi_V + m_2 \eta_V + m_3 \zeta_V) \tag{3.56}$$

$D(\vec{x}_V)$ is the distance from point V to the reconstructed interface $m_1 \xi + m_2 \eta + m_3 \zeta = \alpha$ in cell (i, j, k).

If $D(\vec{x}_V) \times S^{\phi}_{i',j',k'} \geq 0$, it indicates that point V and the center of cell (i', j', k') are in the same phase. It needs to go to step (2).

(2) The projection point P of point (i', j', k') on the interface can be found. The coordinates of point P is $\vec{x}_P = (\xi_P, \eta_P, \zeta_P)$ which can be computed by,

$$\vec{x}_P = \vec{x}_{i',j',k'} + \vec{m} \times D(\vec{x}_{i',j',k'}) \tag{3.57}$$

If point P falls inside of cell (i, j, k), $D(\vec{x}_{i',j',k'})$ is the shortest distance. Otherwise point P stays outside of cell (i, j, k), it needs to find the closest point on the boundary of interface segment.

(3) The closest point S on the boundary of interface segment has several possible candidates. For 2D cases, it can be one of the two end points of the line segment. For 3D cases, it can be one of the vertices of the n-sides polygon, or the projection point of the cell (i', j', k') center onto one polygon side.

To determine the coordinates of point S, $\vec{x}_S = (\xi_S, \eta_S, \zeta_S)$, there are two sets of auxiliary coordinates, $\vec{x}_{off} = (\xi_{off}, \eta_{off}, \zeta_{off})$ and $\vec{x}_{fc} = (\xi_{fc}, \eta_{fc}, \zeta_{fc})$.

$\vec{x}_{off}$ is the distance that the projection point P deviates away from the nearest boundary of cell (i, j, k) in each direction, given by,

$$\begin{cases} \xi_{off} = \max(\left|\xi_p - \xi_i\right| - 0.5\Delta\xi, 0) \\ \eta_{off} = \max(\left|\eta_p - \eta_i\right| - 0.5\Delta\eta, 0) \\ \zeta_{off} = \max(\left|\zeta_p - \zeta_i\right| - 0.5\Delta\zeta, 0) \end{cases} \tag{3.58}$$

$\vec{x}_{fc}$ is the nearest face of cell (i, j, k) to the projection point, given by,

$$\begin{cases} \xi_{fc} = \xi_i + sign(\xi_p - \xi_i) \times \dfrac{\Delta\xi}{2} \\ \eta_{fc} = \eta_i + sign(\eta_p - \eta_i) \times \dfrac{\Delta\eta}{2} \\ \zeta_{fc} = \zeta_i + sign(\zeta_p - \zeta_i) \times \dfrac{\Delta\zeta}{2} \end{cases} \tag{3.59}$$

In Wang's method, the nearest face of cell (i, j, k) intercepted by the interface can be found, based on which is the maximum value among $(\xi_{off}\left|m_1\right|, \eta_{off}\left|m_2\right|, \zeta_{off}\left|m_3\right|)$. For 2D case of $(\xi_{off}\left|m_1\right|, \eta_{off}\left|m_2\right|)$, if $\xi_{off}\left|m_1\right| > \eta_{off}\left|m_2\right|$, set $\xi_S = \xi_{fc}$, and substitute ξ_S into the interface equation to get η_S. For general 3D case of $(\xi_{off}\left|m_1\right|, \eta_{off}\left|m_2\right|, \zeta_{off}\left|m_3\right|)$, if $\zeta_{off}\left|m_3\right|$ is the maximum value, set $\zeta_S = \zeta_{fc}$, and substitute ζ_S into the interface equation which reduces to a 2D problem. By repeating step (2) and step (3), ξ_S and η_S can be obtained.

The above procedure fails to find the closest point *S* on the interface based on $(\xi_{off}|m_1|, \eta_{off}|m_2|, \zeta_{off}|m_3|)$, when one or more components of the normal $\vec{m}$ are zero. In this study, all the possibilities, in which the component of the normal $\vec{m}$ might be zero, are taken into account. Some modifications are made for Wang's method to avoid using $(\xi_{off}|m_1|, \eta_{off}|m_2|, \zeta_{off}|m_3|)$.

For the set of auxiliary coordinate, $\vec{x}_{off} = (\xi_{off}, \eta_{off}, \zeta_{off})$, the component is checked one by one. If $\xi_{off} > 0$, the nearest face of cell (i, j, k) is ξ_{fc}. Set $\xi_S = \xi_{fc}$, and substitute ξ_S into the interface equation which reduces to a 2D problem. By repeating step (2) and (3), ξ_S and η_S can be obtained. If point *S* falls inside of cell (i, j, k), it is the final closest point *S* on the interface. If not, go to check η_{off} and ζ_{off}. If any of η_{off} and ζ_{off} is positive, the same procedure is applied as for ξ_{off}. Finally, point *S*, $\vec{x}_S = (\xi_S, \eta_S, \zeta_S)$, can be obtained.

After that, point *T*, $\vec{x}_T = (\xi_T, \eta_T, \zeta_T)$, can be confirmed, which is point *V*, point *P*, or point *S*. Point *T* is the closest point to cell (i', j', k') in transformed grid, while the LS function represents a signed physical distance. It indicates the distance function needs a transformation from the transformed grid to the physical grid. In this case, tri-linear interpolation scheme is adopted to locate the closest point *TP*, $\vec{x}_{TP} = (x^1_{TP}, x^2_{TP}, x^3_{TP})$, in physical grid. In figure 3.7, point *T* belongs to a computational cell with the cell spacing (c_1, c_2, c_3).

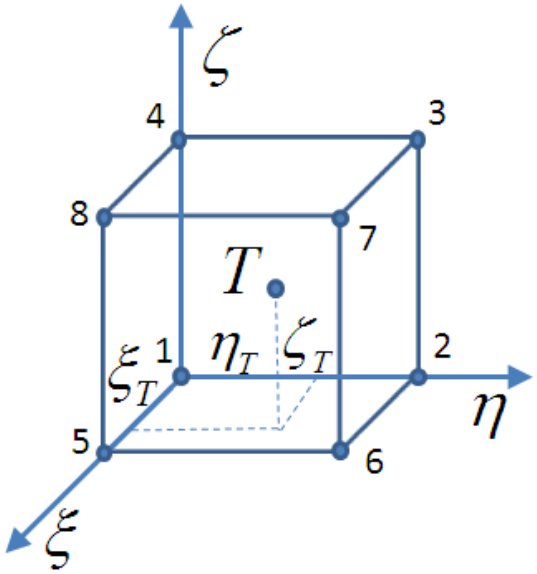

Figure 3.7: Schematic for tri-linear interpolation

$$
\begin{cases}
x_{TP}^1 = [(1-\xi_T)(1-\eta_T)(1-\zeta_T)x_1^1 + (1-\xi_T)\eta_T(1-\zeta_T)x_2^1 + (1-\xi_T)\eta_T\zeta_T x_3^1 + \\
\quad (1-\xi_T)(1-\eta_T)\zeta_T x_4^1 + \xi_T(1-\eta_T)(1-\zeta_T)x_5^1 + \xi_T\eta_T(1-\zeta_T)x_6^1 + \\
\quad \xi_T\eta_T\zeta_T x_7^1 + \xi_T(1-\eta_T)\zeta_T x_8^1]/(c_1c_2c_3) \\
x_{TP}^2 = [(1-\xi_T)(1-\eta_T)(1-\zeta_T)x_1^2 + (1-\xi_T)\eta_T(1-\zeta_T)x_2^2 + (1-\xi_T)\eta_T\zeta_T x_3^2 + \\
\quad (1-\xi_T)(1-\eta_T)\zeta_T x_4^2 + \xi_T(1-\eta_T)(1-\zeta_T)x_5^2 + \xi_T\eta_T(1-\zeta_T)x_6^2 + \\
\quad \xi_T\eta_T\zeta_T x_7^2 + \xi_T(1-\eta_T)\zeta_T x_8^2]/(c_1c_2c_3) \\
x_{TP}^3 = [(1-\xi_T)(1-\eta_T)(1-\zeta_T)x_1^3 + (1-\xi_T)\eta_T(1-\zeta_T)x_2^3 + (1-\xi_T)\eta_T\zeta_T x_3^3 + \\
\quad (1-\xi_T)(1-\eta_T)\zeta_T x_4^3 + \xi_T(1-\eta_T)(1-\zeta_T)x_5^3 + \xi_T\eta_T(1-\zeta_T)x_6^3 + \\
\quad \xi_T\eta_T\zeta_T x_7^3 + \xi_T(1-\eta_T)\zeta_T x_8^3]/(c_1c_2c_3)
\end{cases}
\tag{3.60}
$$

3.4 VOF Function for Overset Grid System

Besides using the general curvilinear structured grid, a Chimera domain decomposition approach is also implemented into the present CLSVOF method using an

overset grid system, including embedding, overlapping, and matching grids for accurate resolution of complex geometries. The key technique is the inter-grid communications through interior boundary which represents all the boundaries among overset grids.

Because the LS function is smooth, the LS function on interior boundary among overset grid blocks can be obtained by using standard Chimera interpolation technique [44], [45]. However, it is invalid to directly interpolate the VOF function or the liquid volumes across interior boundary since the volume fraction varies with the computational cell size. In the present study, a new numerical procedure is implemented to ensure that the VOF function is updated consistently with the local LS function across interior boundary.

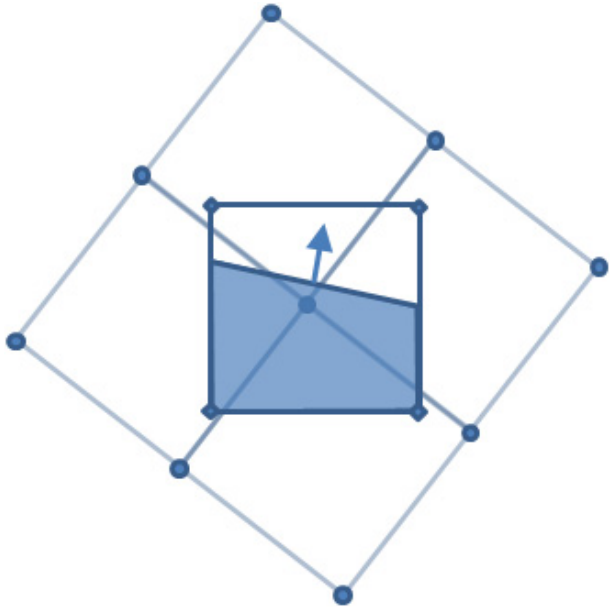

(a) Cell embedded in background grid

Figure 3.8: Evaluation of the VOF function on overset grid boundary

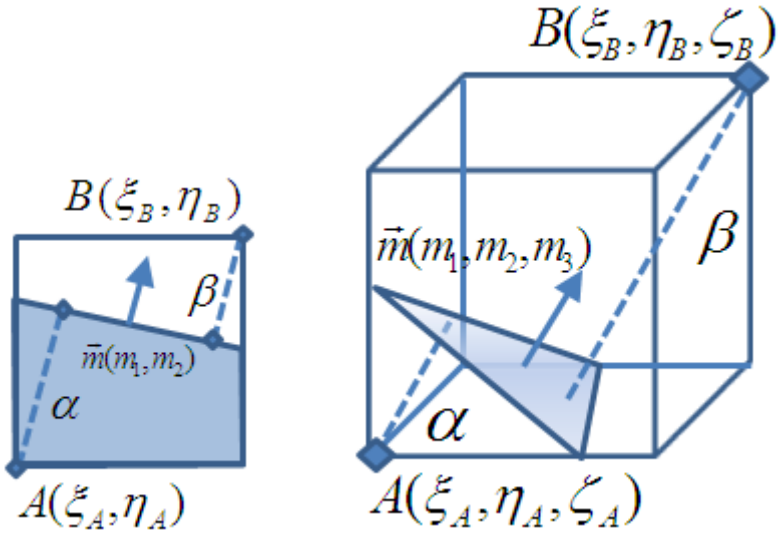

(b) 2D and 3D computational cell

Figure 3.8: (Continued)

In figure 3.8(a), one computational cell, which belongs to interior boundary of another grid, is embedded in background grid. When the information about the VOF function is properly evaluated for such cells on interior boundary, the inter-grid communication technique is applicable for the VOF function. Firstly, the LS function at every corner point can be interpolated using the standard Chimera technique, for each cell on the interior boundary. The local origin is chosen as the corner point with the largest LS function value. In figure 3.8(b), point A, $\vec{x}_A = (\xi_A, \eta_A, \zeta_A)$ is the local origin. The parameter α indicates the shortest distance from point A to the interface plane from equation (3.11). Similarly, β denotes the shortest distance from point B, $\vec{x}_B = (\xi_B, \eta_B, \zeta_B)$, which is opposite to point A. it is noted that the parameters α and β are the distances in the transformed grid; while the LS function at point A and point B are the physical

distances. It is assumed that the ratios of the distances between point A and point B in the transformed and physical grids are identical,

$$\frac{\alpha}{\beta} = \left| \frac{\phi_A}{\phi_B} \right| \tag{3.61}$$

From the interface equation of this cell,

$$m_1 \xi + m_2 \eta + m_3 \zeta = \alpha \tag{3.62}$$

The parameter β can be also obtained by equation (3.62),

$$\left| m_1 \xi_B + m_2 \eta_B + m_3 \zeta_B - \alpha \right| = \beta \tag{3.63}$$

Combining equation (3.61) and equation (3.63), the parameter α is solved. The evaluation of the VOF function is turned into the "forward" problem in interface reconstruction algorithm (equation (3.12), (3.13), or (3.14)). In conclusion, this is the inter-grid communication technique for the VOF function among the overset grid system.

3.5 Mass Conservation Scheme for Overset Grid System

In the section 3.3.2, it has demonstrated that current EI-LE scheme can conserve the precise mass within a single domain. Even for flow field which is not exactly discrete divergence-free, the mass conservation can still be achieved by the aid of the 1st volume-correction term.

For overset grid system considered here, an additional volume-correction procedure has also been incorporated into the present interface advection algorithm to enforce mass conservation across non-matching overset grids. The current EI-LE scheme with the 1st volume-correction term is employed for every grid block in overset grid

system. It indicates that every gird block is able to conserve the mass conservation within its own domain. However, the inter-grid communication for the VOF function is required to pass the VOF function information from one grid to another. This technique is consistently related with the local LS function which does not possess the mass conservation ability. To maintain global mass conservation for the entire overset grid system, the 2nd volume-correction term is collected for each grid of the overset grid system to compensate the potential volume change.

The 2nd volume-correction term is formed by two parts: (1) the first part is the volume change between the inter-grid treatment for the VOF function and the EI-LE advection scheme; (2) the other part is the net liquid volume fluxes out of each interior boundary. Similar to the 1st volume-correction term, each grid block can collect its own 2nd volume-correction term summation. Because this kind of volume-correction is accounted for the volume from one grid to another, all of the 2nd volume-correction terms are collected together and redistributed to the cut cells in the entire overset grid system.

3.6 Summary of Present CLSVOF Method

Figure 3.9 is the flow chart for the present CLSVOF method algorithm in overset grid system.

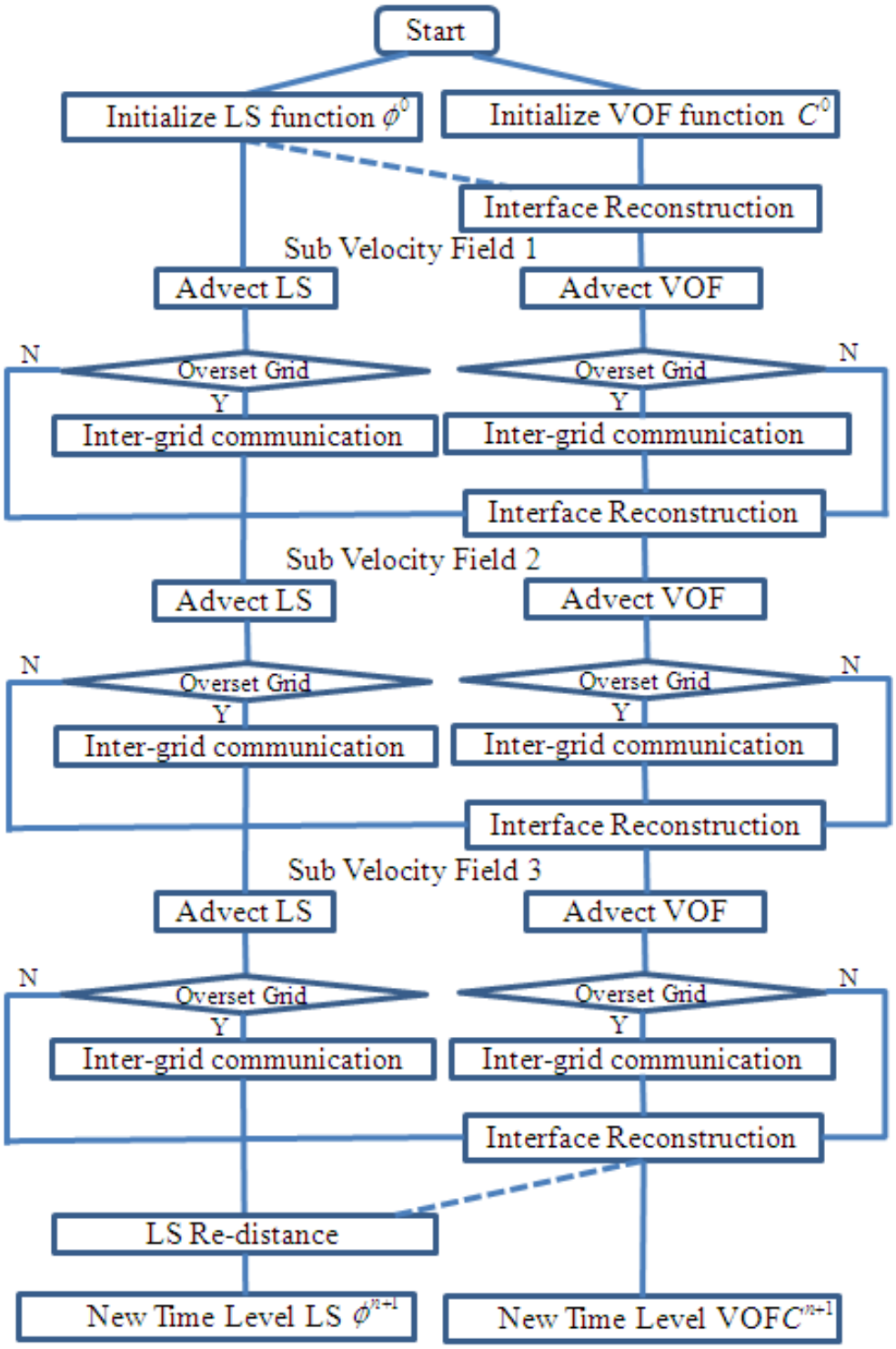

Figure 3.9: Flow chart of the CLSVOF method

CHAPTER IV

TEST CASES

4.1 Introduction

In the previous chapters, the methodology of interface capturing has been presented for two-phase immiscible fluids. In this chapter, the methodology has been implemented and tested against several test cases.

4.2 2D Single Vortex Flow

This test case is concerned with the stretching of a circular fluid element in a swirling shear velocity field [16]. The objective of this test case is to evaluate how well the EI-LE interface advection scheme conserves mass and handles the development of the stretched and deformed interface to a large extent.

The divergence-free velocity field is given below in a 1.0×1.0 solution domain with a flow oscillation period T = 8.0. The time increment is 0.5.

$$\begin{cases} u = -\sin^2(\pi x)\sin(2\pi y)\cos(\dfrac{\pi t}{T}) \\ v = \sin^2(\pi y)\sin(2\pi x)\cos(\dfrac{\pi t}{T}) \end{cases} \tag{4.1}$$

Initially, a circle with a radius of 0.15 is centered at (0.5, 0.75). The size of the 2D domain is shown in figure 4.1, for both the rectangular and curvilinear solution domain using 128×128 numerical grids.

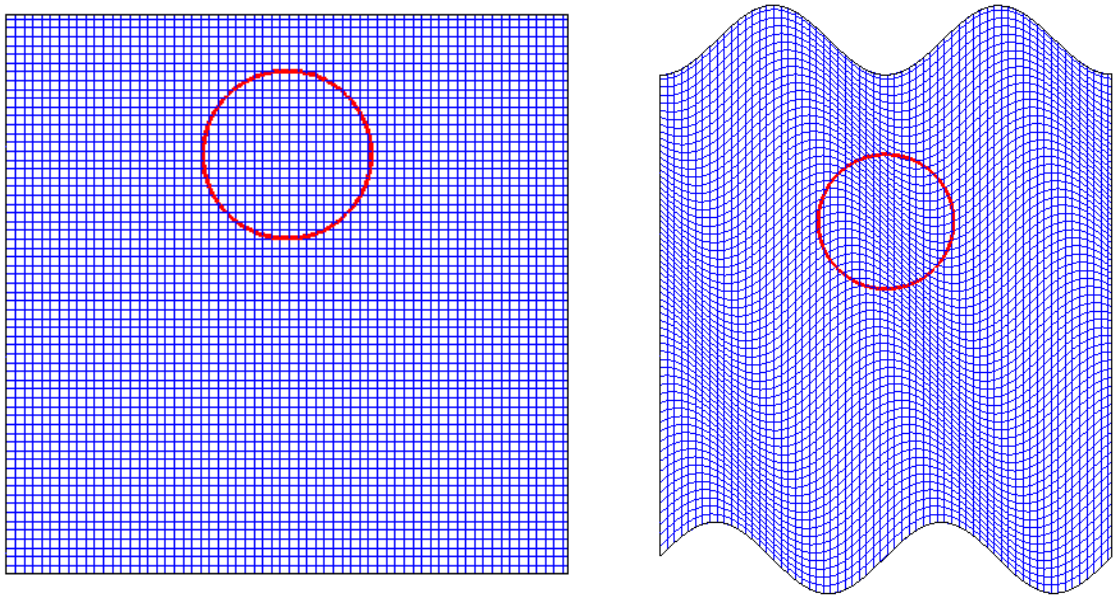

Figure 4.1: Numerical grids and initial circular fluid

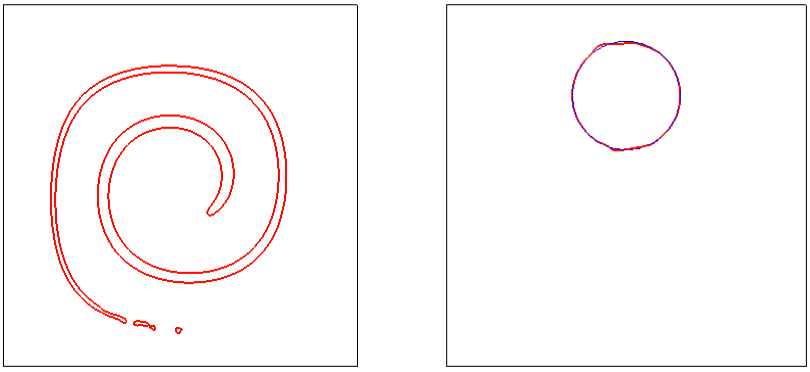

(a) Interface in Cartesian grid at t = 4 and 8

Figure 4.2: Single vortex flow test

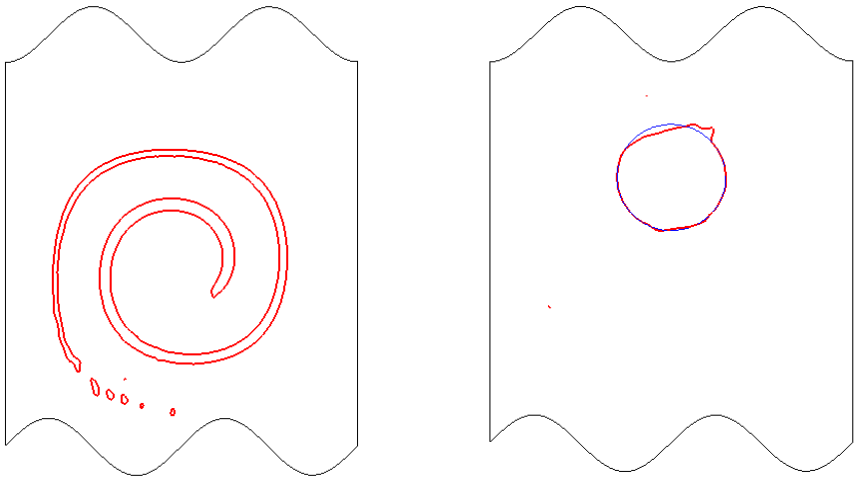

(b) Interface in curvilinear grid at t = 4 and 8

Figure 4.2: (Continued)

Figure 4.2 shows the interface evolution in both Cartesian and curvilinear grids. It can be seen that at t = 4, the fluid is stretched to the maximal position where the sharpest and thinnest filament appears. On the tail of the liquid filament, the fluid is broken into several small droplets. The occurrence of this type of break-up is due to the fact that it is assumed there exists only one piecewise linear segment in the cut cell. When the filament is smaller than one grid spacing, one piecewise linear segment cannot fully describe the specific structure of such filament. However, PLIC scheme is still adopted as the interface reconstruction algorithm because PLIC scheme is robust and straightforward for interface reconstruction. The "break-up" symptom can be avoided by increasing the grid resolution. After the flow returns back at t = 8, the recovered shape of the interface is compared with the original interface. The recovered shape in Cartesian grid is closer to the initial shape than that in curvilinear grid. It can be explained by that

the geometrical coefficients from curvilinear grid cannot be computed accurately as those from Cartesian grid.

As expected, the present CLSVOF method is very effective in maintaining mass conservation. The relative mass change during one period is 1.42×10^{-3} % for Cartesian grid, and 0.07% for curvilinear grid. The same case was also performed as a benchmark test by several other researchers. The relative mass loss using the CLSVOF method is 0.04% by Wang et al. [42], and 0.01% by Menard et al. [40].

4.3 3D Single Vortex Flow

This case is extended from 2D single vortex flow in section 4.2, to demonstrate the 3D interface capturing ability. In this case, a 3D incompressible flow in an 1.0×1.0×1.0 solution domain is prescribed, with an oscillation period T = 3.0 and time increment of 0.5,

$$\begin{cases} u = 2\sin^2(\pi x)\sin(2\pi y)\sin(2\pi z)\cos(\dfrac{\pi t}{T}) \\ v = -\sin(2\pi x)\sin^2(\pi y)\sin(2\pi z)\cos(\dfrac{\pi t}{T}) \\ w = -\sin(2\pi x)\sin(2\pi y)\sin^2(\pi z)\cos(\dfrac{\pi t}{T}) \end{cases} \tag{4.2}$$

A sphere with a radius of 0.15 is centered at (0.35, 0.35, 0.35). The 3D domain size is $101\times101\times101$ with a uniform Cartesian grid and a curvilinear grid with the same *x*-*y* plane shown in figure 4.1 with uniform spacing in the *z*-direction. Figure 4.3 shows the deformed shapes of the sphere at t = 0, t = 1.0, t = 1.5, and t = 3 for the LS method and the CLSVOF method.

The full velocity field combines a deformation in the *x-y* plane another deformation in the *x-z* plane. Therefore, the sphere is stretched by these two rotating vortices to stretch out the middle part of the interface until t = 1.5. And it goes on to return to the initial position at t = 3. It is seen that there was a very large (26.92%) mass loss for the level-set method as the droplet was split into several smaller pieces under vortex stretching process. Furthermore, the droplet is unable to recover its original spherical shape due to insufficient grid resolution. On the other hand, the CLSVOF method is able to maintain excellent mass conservation with a relative mass change of 9.22×10^{-5}% in Cartesian grid and 2.47×10^{-3}% in curvilinear grid, at the end of one period. Wang (2009) also proposed this case in Cartesian grid and obtained a relative mass error of 0.4%. This clearly demonstrates the capability of the present CLSVOF method in maintain divergence-free condition under 3D strong velocity gradients.

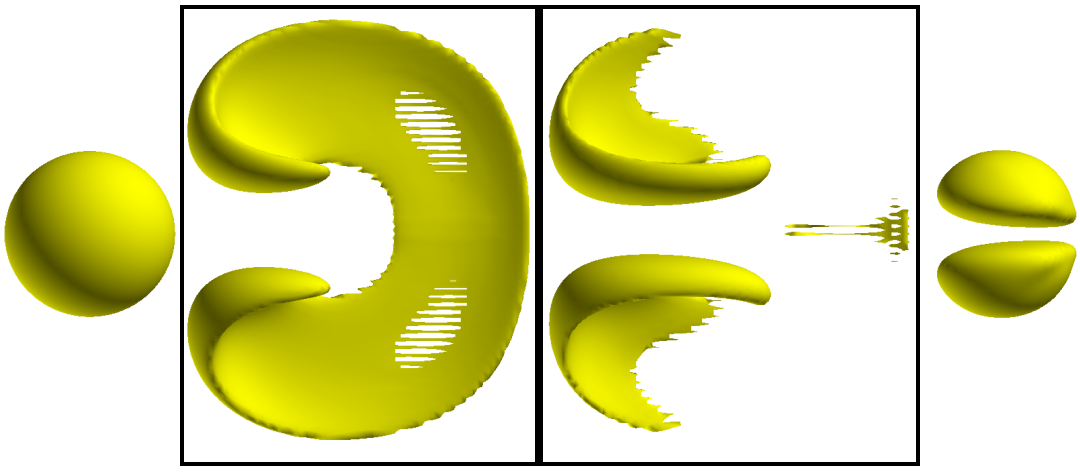

(a) Interface for level-set method in Cartesian grid

Figure 4.3: 3D deformation of a sphere at t = 0, 1.0, 1.5 and 3

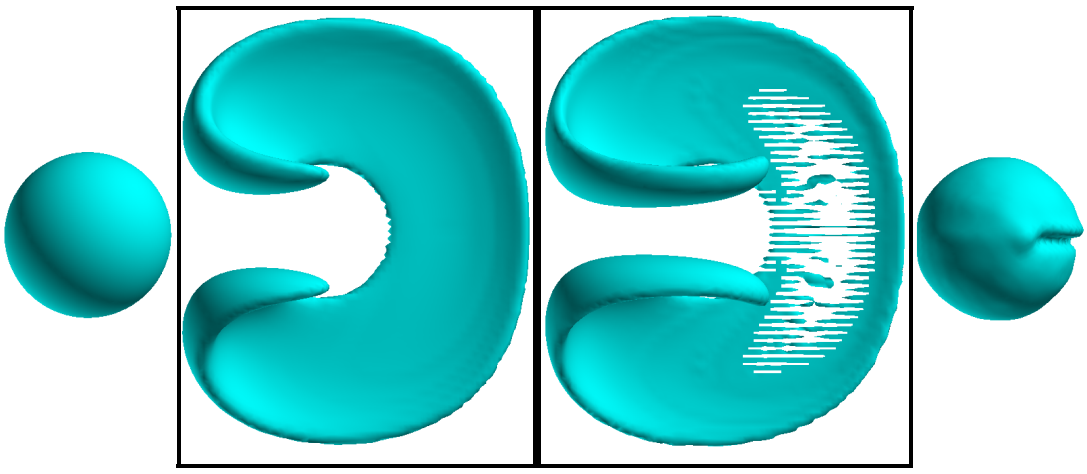

(b) Interface for CLSVOF method in Cartesian grid

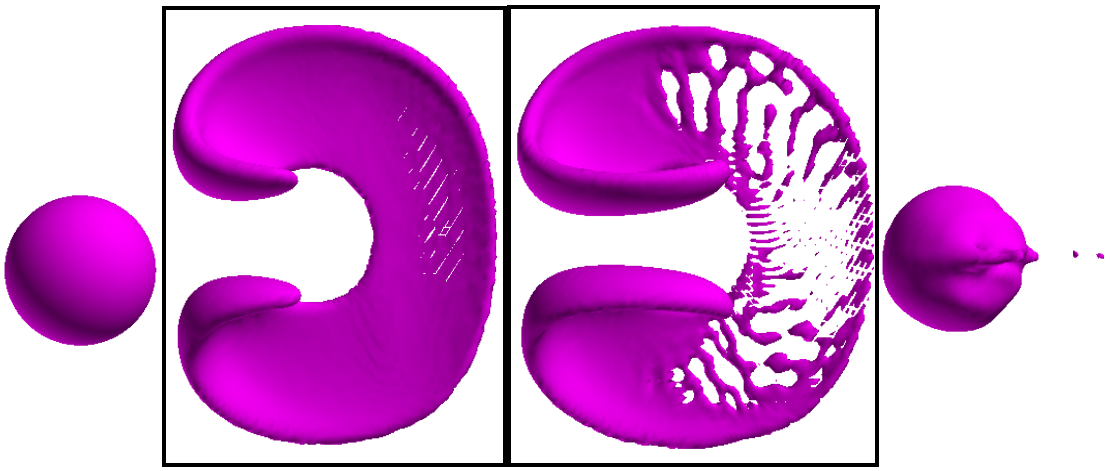

(c) Interface for CLSVOF method in curvilinear grid

Figure 4.3: (Continued)

4.4 3D Deformation Flow with Overset Grid System

Succeed with 2D single vortex flow and 3D deformation flow, the 3D deformation flow with an overset grid system is designed to demonstrate the present interface capturing method in overset grid system. In this case, the overset grid system is

constructed with two overlapping semi-cylindrical grids (in green and yellow) embedded in a Cartesian background grid as shown in figure 4.4. The background domain is further split into outer (in blue) and inner (in red) by the cylindrical regions.

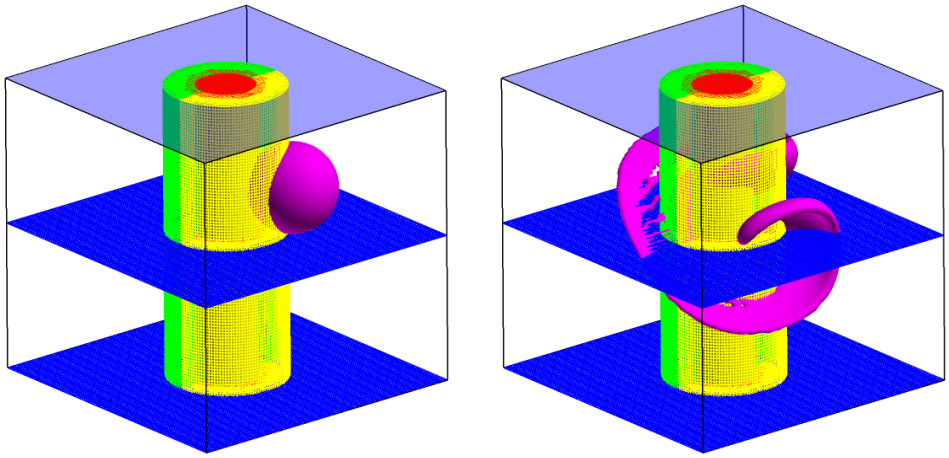

Figure 4.4: Overset grid system for simulation of sphere deformation

It is seen from figure 4.5 that the interface of the deforming sphere passed through each non-matching overset grid block before returning into its initial position after one complete cycle. The final shape of the interface is similar to that shown in figure 4.3(b), but somewhat large distortion was observed due to the grid interpolation error across overset grids. The relative mass change in the overset grid system is 3.46×10^{-4}%, which demonstrates the effectiveness of the present volume-correction scheme for non-matching overset grid system.

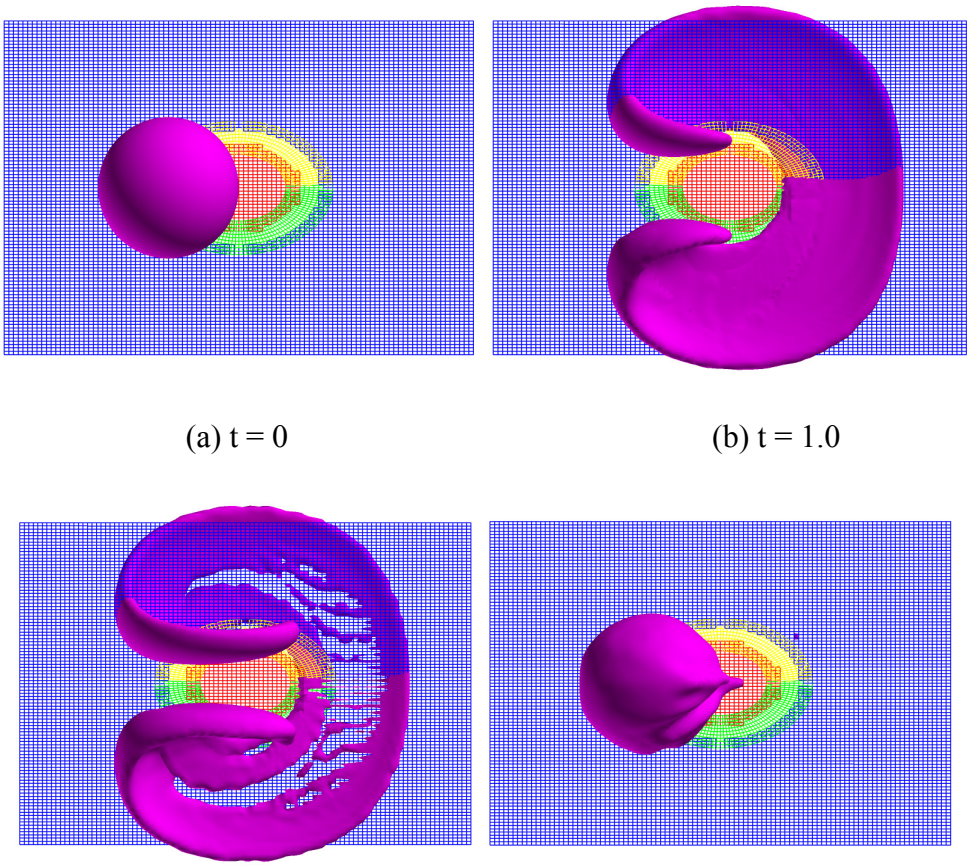

(a) t = 0 (b) t = 1.0

(c) t = 1.5 (d) t= 3.0

Figure 4.5: Deformation of a sphere in overset grids

4.5 2D Dam Breaking Flow

The collapse of a water column over a rigid horizontal plane is called a dam breaking problem. This simulation is carried out over a 5×2 solution domain with grid size 251×101 and uniform grid spacing of 0.02. The numerical setup follows the experiments by Martin and Moyce (1952) [46]: the water column, with 1.0 height and

1.0 length on the left side of the tank, is released at time t = 0. A time increment of 0.002 is used in the present simulation.

The snapshots of the instantaneous free surface are shown in figure 4.6, where red region represents air and blue region is water. When the barrier was removed, the flow collapsed and flushed to the downstream due to the gravitational effect. As the edge of water front reached the tank wall, the flow began to climb along the tank wall upward till the kinetic energy completely turned into potential energy. The flow started to fall back to the tank bottom and produced overturning wave structures due to flow instability at the air-water interface. At the end of the simulation, several air pockets and water droplets can be observed along the channel. The relative mass change for the CLSVOF method at t = 8.0 was only 0.026%.

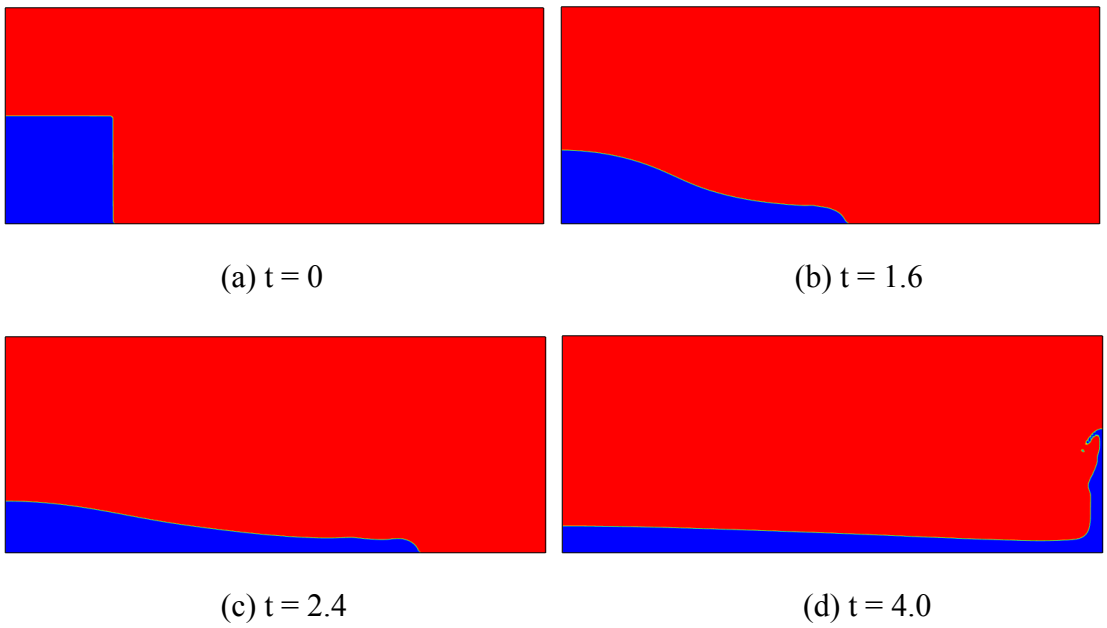

(a) t = 0 (b) t = 1.6

(c) t = 2.4 (d) t = 4.0

Figure 4.6: Free surface pattern in 2D dam breaking

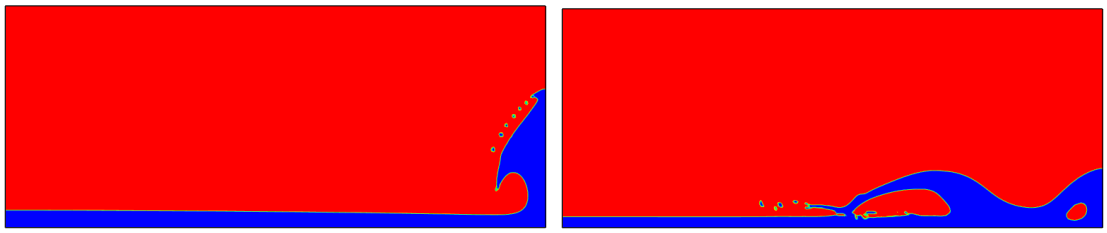

(e) t = 5.6 (f) t = 8.0

Figure 4.6: (Continued)

4.6 3D Dam Breaking Flow

After successful simulation of the 2D dam breaking problem, the present CLSVOF method is extended for 3D dam breaking problem. Simulation is performed for dam breaking in a rectangular tank as shown in figure 4.7 with a time increment of 0.002. A 251×101×31 grid is used to cover the 5×2×0.6 solution domain with uniform grid spacing of 0.02 in all three directions. The Stillwater column is initialized as 1.0 long, 1.0 high, and 0.6 wide. It is seen from figure 4.7 that the free surface remained two-dimensional before the wave front reached the tank sidewall. When the flow began to run up along the tank wall, the wave front quickly became three-dimensional with strong flow interaction in the transverse direction. Overturning waves with large air pockets and small water droplets were observed after t = 5.0 as the wave front fell back into the tank and collided with the trailing water in the tank. Complex 3D breaking waves and splashes were observed at t = 8.0 and 12.0 with the presence of small droplets and air

bubbles. The relative mass change in our CLSVOF method was only 4.87×10^{-3}% at t = 12.0.

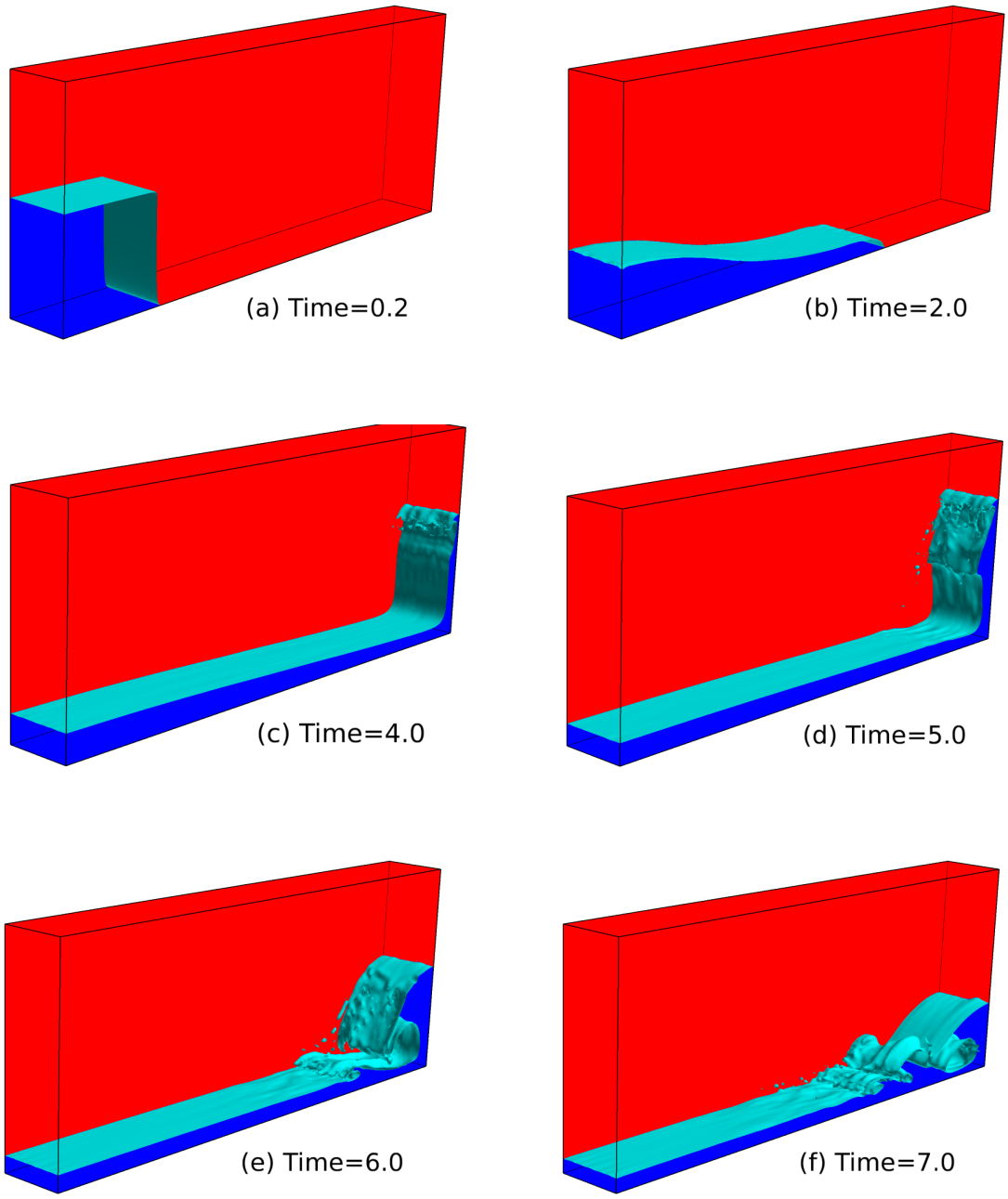

Figure 4.7: Free surface pattern for 3D dam breaking problem

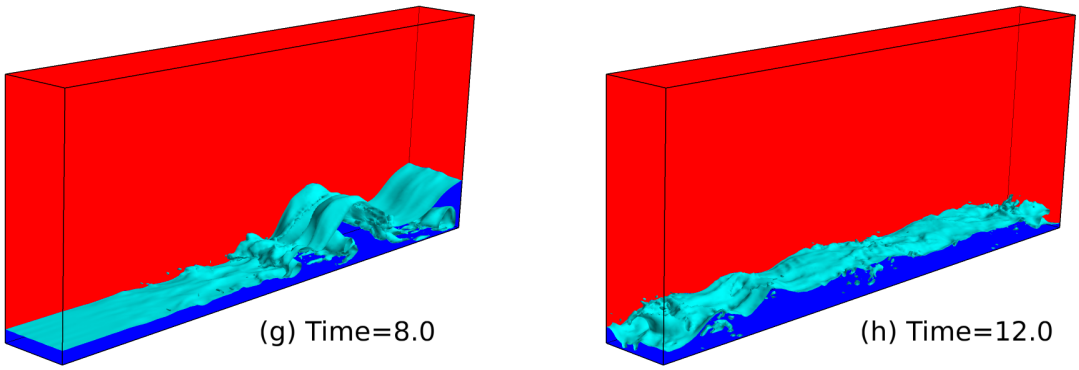

Figure 4.7: (Continued)

Figure 4.8 shows a comparison of the predicted time histories of the surge front and water column height with the experiment data of Martin and Moyce (1952) [46]. Both the 2D and 3D CLSVOF results are in good agreement with the experiment data.

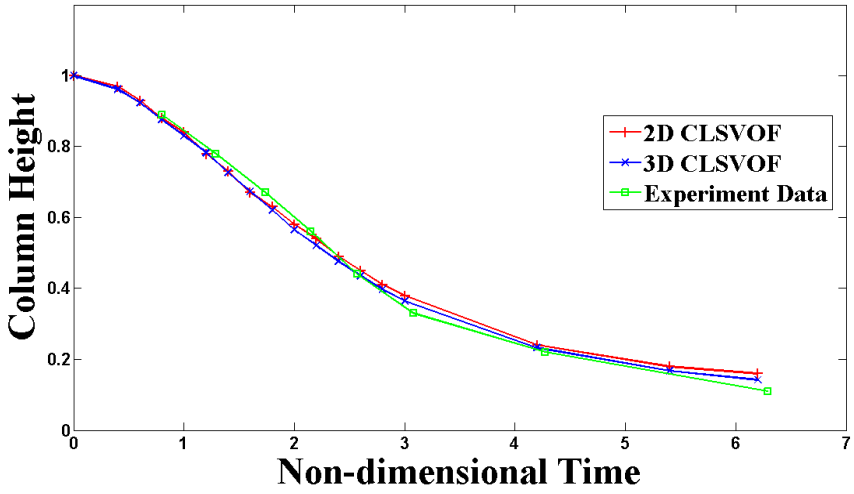

(a) Column height vs. time

Figure 4.8: Comparison of numerical results and experimental data

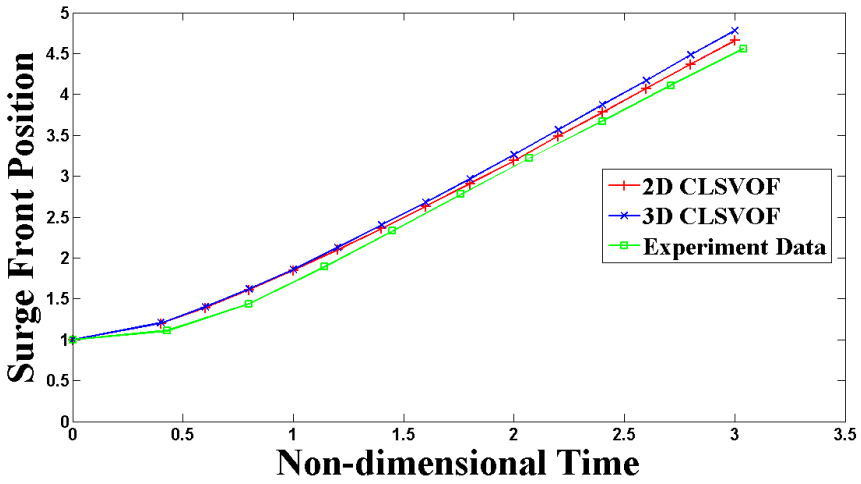

(b) Surge front vs. time

Figure 4.8: (Continued)

4.7 3D Dam Breaking Flow with Cylindrical Pillar

In this test case, a cylindrical pillar of diameter D = 0.4 is placed in a 4.0×1.4×1.1 rectangular tank as shown in figure 4.9. The still water column is initialized as 1.0 long, 1.0 high and 1.1 wide. And the pillar is located at a distance of 3.0 from the upstream boundary. The time increment is specified as 0.002. An overset grid system similar to that shown in figure 4.4 is used in the present study with two overlapping semi-cylindrical grids embedded in a rectangular tank grid. The free surface profiles at ten different time instants are shown in figure 4.9 to illustrate the complex 3D dam breaking flow and its interaction with the cylindrical pier, as well as tank sidewalls. The simulation successfully resolved the wave run-up in front of the pillar, the overturning wave on the tank wall, and the presence of air pockets behind the cylindrical

pillar. It is clearly seen that the leeside of pillar was completely dry until t = 3.4. It is also interesting to note that a small section of the tank bottom remained dry at t = 4.0 even though the water splashed up from the downstream wall already impinged upon the leeside of the cylindrical pillar. Finally, the relative mass loss at t = 8.0 was 1.86×10^{-3}%. The simulation results clearly demonstrate the capability of the present CLSVOF method for effective resolution of violent free surface flows in an overset grid system involving embedding and overlapping grids.

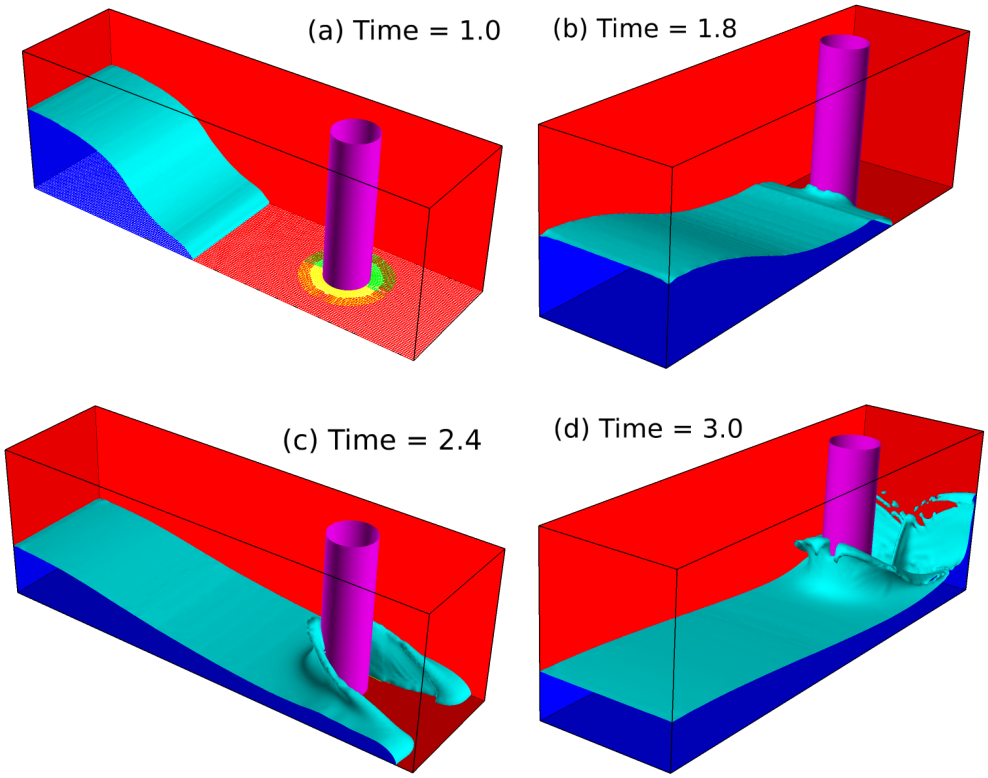

Figure 4.9: 3D dam breaking around a cylindrical pillar

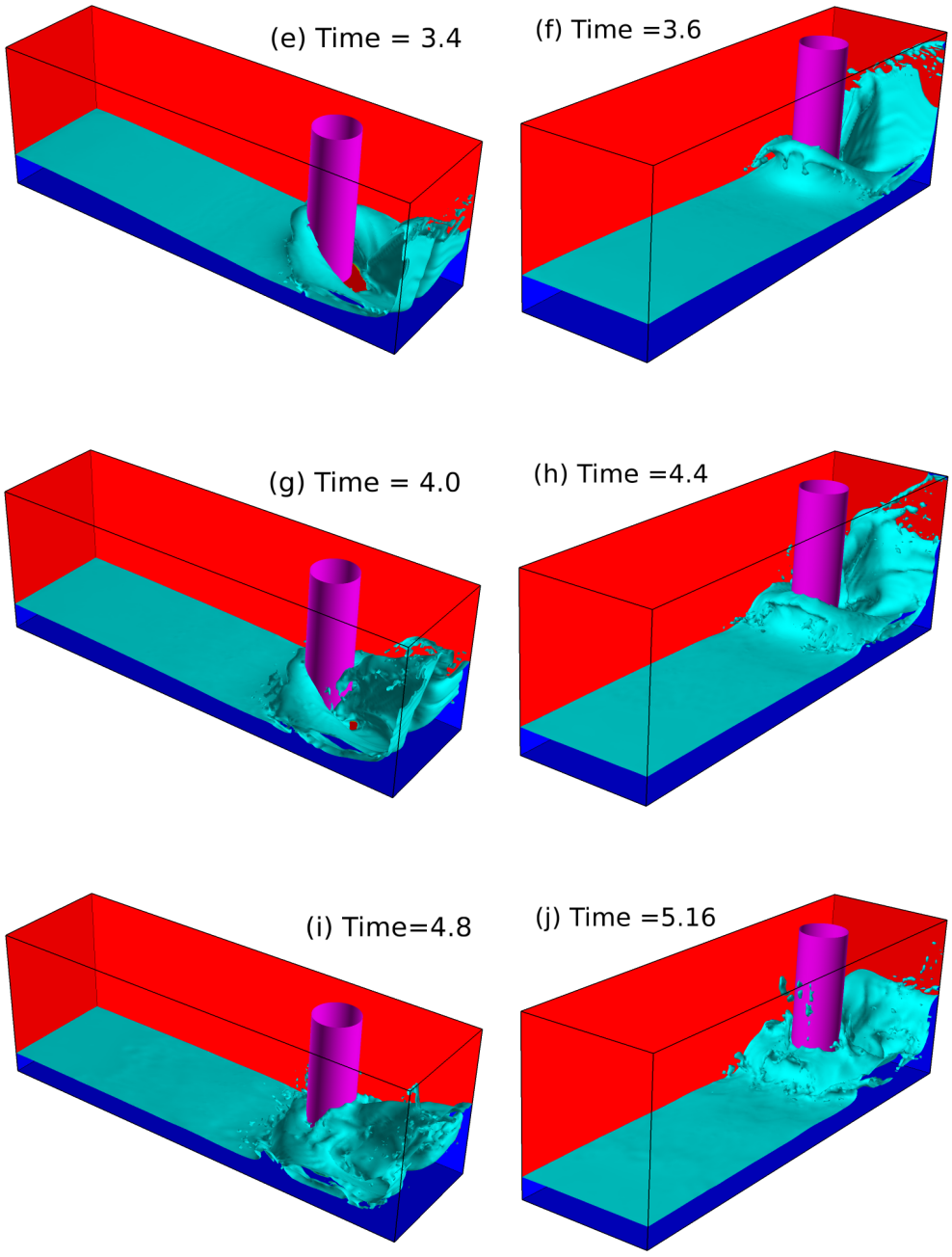

Figure 4.9: (Continued)

CHAPTER V

SLOSHING FLOW IN PARTIALLY FILLED LNG TANK

5.1 Introduction

As the increasing demand for natural gas, the trend of Liquefied Natural Gas (LNG) carriers with supersize cargo capacity is growing in the world fleet of LNG carriers. Most of the current LNG carrier designs adopt the membrane-type LNG cargo tanks. It is common operation for supersize LNG carriers with a wide range of filling conditions, for which it is prone to violent sloshing inside tanks under certain sea condition. Sloshing can produce localized high impact loads on tank walls and ceiling which may lead to severe structural damage. Hence, it is essential to investigate sloshing phenomena for the design of membrane-type tank structure and the safety operation with partially filled conditions. For the analysis of sloshing, model test has been known as the most reliable method in predicting the maximum impact pressure due to the complex sloshing phenomenon. However, the impact load scaled up from model test to prototype is still not clear because of the scale effects associated with some unmatched parameters such as fluid viscosity, density ratio between liquid and ullage gas, ullage pressure and wall elasticity.

Numerical methods are alternative tools in applying for the simulation of sloshing problems inside LNG tanks. Any appropriate numerical method must be able to handle arbitrary interface behavior due to the complexity of sloshing phenomena. The Marker and Cell (MAC) method, the Volume-of-Fluid (VOF) method and the Level-Set

(LS) method have been successfully applied to capture the profile of the interface in LNG sloshing. Arai et al. used the MAC method to compute sloshing impact pressure in 2D and 3D simulations [47], [48]. Nam and Kim used the smoothed particle hydrodynamics (SPH), which is developed from the MAC scheme, to solve the two-dimensional sloshing flows [49]. Kim used the SOLA-SURF program to simulate the sloshing problem in rectangular and prismatic tanks [50], [51]. Loots et al. presented an improved Volume of Fluid (iVOF) method to numerically produce the dynamics of sloshing in LNG tanks, with several improvements in the treatment of spikes for the pressure signals [52]. Wemmenhove et al. extended iVOF method to incorporate two-phase flow and improved the method to simulate the effect of gas bubbles of different sizes [53]. Yu and Chen performed the Level-Set Reynolds-Averaged Navier-Stokes (RANS) method for the simulation of liquid sloshing in 2D and 3D LNG tanks [54], [55].

As it discussed the above numerical methods in Chapter I, each of them has its own advantages and disadvantages. However, a coupled method can take advantage of the strength of the two coupled methods, and is superior to either single method. For this particular sloshing flow problem, there are two major requirements to necessarily fulfill. The first requirement is to preserve the mass conservation. Considering sloshing flow is developing inside an enclosed tank, the mass conservation of liquid fluid (LNG) is the fundamental task for simulation and also directly affects the impact pressure measured on wall. The other requirement is to accurately capture the violent sloshing flow on the basis of mass conservation. The sloshing flow is one complicated and violent flow, especially when the exciting frequency is close to the natural frequency of the liquid

fluid. Part of the interface may break up into discontinuous droplets and small air bubbles are trapped in the liquid fluid. The VOF method has its unique capability to keep the mass conservation; and the LS method is celebrated for capturing the sharp and smooth interface. It is natural way to use the CLSVOF method for the sloshing flow simulation.

In the present study, the CLSVOF method is employed as the interface-capturing method for time-domain simulation of sloshing in a three-dimensional membrane-type LNG tank. The sloshing impact load on membrane-type LNG tanks is predicted by the CLSVOF method, which is compared with the numerical result by the pure level set method and the experimental data. The simulation results clearly demonstrate not only the capability of the CLSVOF method for accurate prediction of violent free surface flows, but also the unique feature of the CLSVOF method in mass conservation.

5.2 Experimental and Numerical Setups

This section describes the detailed experimental and numerical setups, including the LNG tank geometry, the locations of sensors for sloshing impact load, the motions of the LNG tank and the filling level conditions. Figure 5.1 shows the schematic of the tank geometry: the dimension of the tank in full scale is 37.9m × 43.72m × 26.75m (tank breadth × tank length × tank height). More precisely, the lower and upper chamfer angles (γ_l, γ_u) are equal to 135°; the lower chamfer height h_l is 3.77m; and the upper chamfer height h_u is 8.63m. The filling level $H\%$ is specified in terms of d/h.

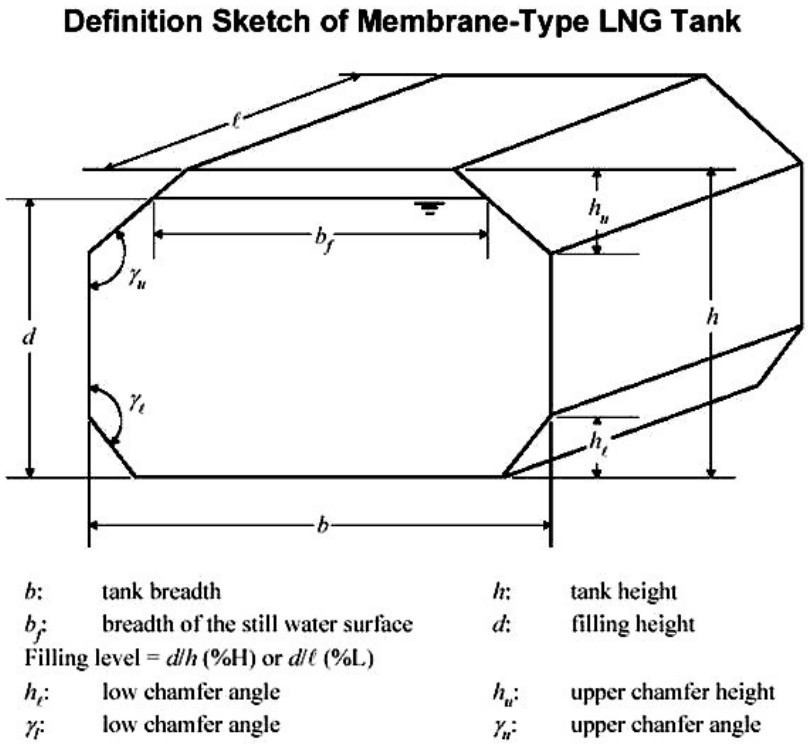

Figure 5.1: Schematic of tank geometry

The experiment with a 1/70 scale model of full scale model was carried out by Lee et al. [56]. The dimension of the 1/70 scale model is 541.36mm × 624.50mm × 382.20mm. A cluster of 17 pressure transducers were mounted on the LNG tank walls to measure the sloshing induced load, as illustrated in figure 5.2. The sampling frequency of the total pressure transducers is about 20,000 Hz.

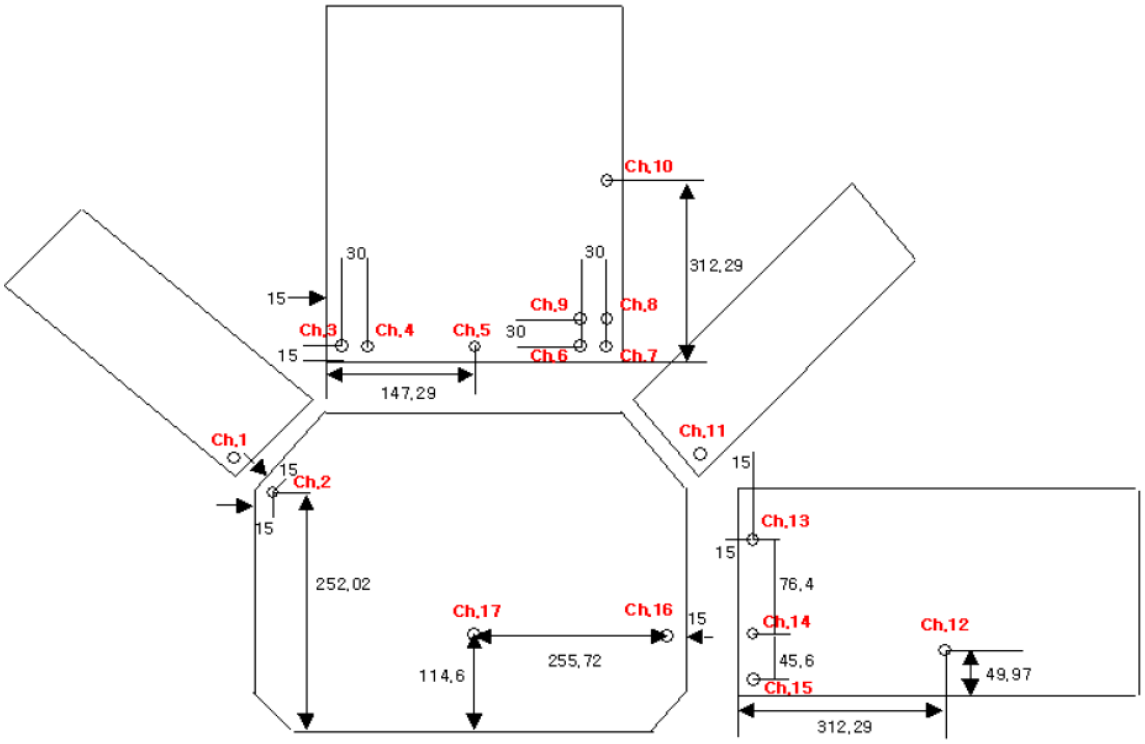

Figure 5.2: Locations of the pressure transducers

In the present numerical simulations, both transverse and longitudinal sloshing motions with various combinations of horizontal, vertical and rotational motion modes are included. As shown in figure 5.3, the transverse motion is along the *x*-direction in the *x*-*z* plane; while the longitudinal motion is along the *y*-direction in the *y*-*z* plane. Table 5.1 and table 5.2 summarize the motion parameters in all of numerical cases considered in present sloshing study. There are total four simulation cases in this study. Two of them (Case 1 and Case 2) are transverse motion cases, and the other two (Case 3 and Case 4) are longitudinal motion cases. For each case, a particular pressure transducer is selected from the total 17 sensors to measure the impact pressure history at its position.

The selected position of pressure transducer can be a representation to reflect the most potential risk about sloshing induced load under certain excited tank motion. In Case 1 which is the lowest filling level in the series of cases, the location is chosen on the bottom of vertical side wall in transverse direction and is slightly above the upper knuckle point of the low chamber. In Case 2, the location is looked into on the inclined surface where is slightly above the lower knuckle corner point of the upper chamber. In Case 3 and Case 4, the locations are selected on the tank top ceiling, where the localized high impact loads may occur but it is most challenging to predict loads by numerical methods.

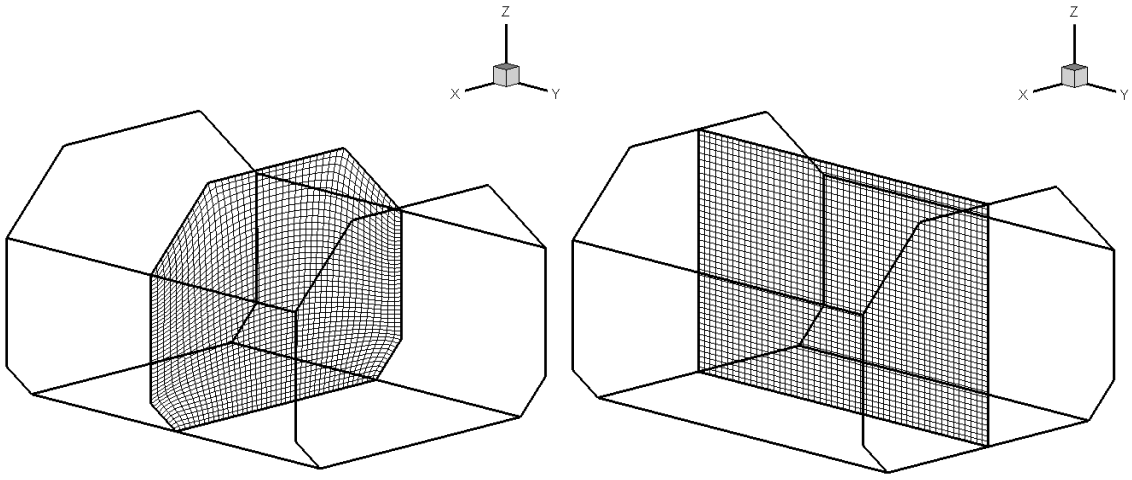

Figure 5.3: Transverse and longitudinal motions in grid planes

Table 5.1: Filling levels, tank motion modes, periods and selected sensor

Case	FLVL(%H)	Motion Mode	Period(s)	Selected Senor No.
1	30	Transverse	9.67	Ch. 15
2	50	Transverse	8.98	Ch. 11
3	80	Longitudinal	7.17	Ch. 7
4	92.5	Longitudinal	9.08	Ch. 3

Table 5.2: Tank motion amplitudes

Case	Horizontal Motion		Vertical Motion		Rotational Motion	
	Amplitude (m)	Phase (rad)	Amplitude (m)	Phase (rad)	Amplitude (rad)	Phase (rad)
1	4.05	-2.96	7.78	-2.18	0.006	0
2	3.38	-0.214	5.89	0.307	0.00248	0
3	0.584	-4.47	1.72	-1.89	0.0121	0
4	0.181	-1.26	6.80	-0.495	0.0952	0

The horizontal, vertical, and rotational motions are defined as follows,

$$Motion(t) = Amplitude \times \sin(\frac{2\pi}{Period} t + Phase) \tag{5.1}$$

After define the motions in each degree of freedom, the general motion is combined by the single motion modes together.

In all the numerical studies, the physical properties of the fluids are chosen in table 5.3. The effect of surface tension is neglected in this study, because the surface tension effect is insignificant in the large-scale fluid flow and has less contribution to

impact pressure load. The simulations are performed in the grid of 85×101×85 with a constant time increment of 0.001T, where T is the motion period. The detailed grid refinement and time increment study can be found in the work of Yu et al. [54] using the level set method. It should be remarked that the data acquisition frequency in numerical simulations is 1,000 Hz, which is lower than the sampling frequency in the experiments (20,000 Hz). It is expectable to miss the higher pressure peaks which are reflected in the experiments. However, the time increment is constrained by the computational time concern and still kept as 0.001T in this study.

Table 5.3: Physical properties of liquids in LNG tank

Phase	Density (kg / m^3)	Dynamic Viscosity ($N \bullet s / m^2$)
Water	1000	1.12 E -3
Air	1.23	1.79 E -5

5.3 Results and Discussions

All of the study cases are normally performed for 20 periods. The pressures at selected locations in figure 5.2 are measured by the pressure sensors. Due to the three-dimensional instability, there occurs the drastically different impact pressure among the sensor locations and their mirror image locations. In order to provide a complete understanding of the three-dimensional sloshing flow, the number of the sensors is increased to 48 in numerical simulations. These 48 sensors in figure 5.4 located not only

at the original 17 sensor locations in figure 5.2, but also at original sensors' mirror image locations in x and y directions. Because the details of sensor size in model test are not known, the measurement locations in model test may not stay precisely at the grid points in numerical grid. In consideration of this, all the impact pressures on a 3×3 grid point stencil around each sensor locations are recorded. It is helpful to post-process the pressure data and determine the proper impact pressure in the vicinity of each pressure sensor location.

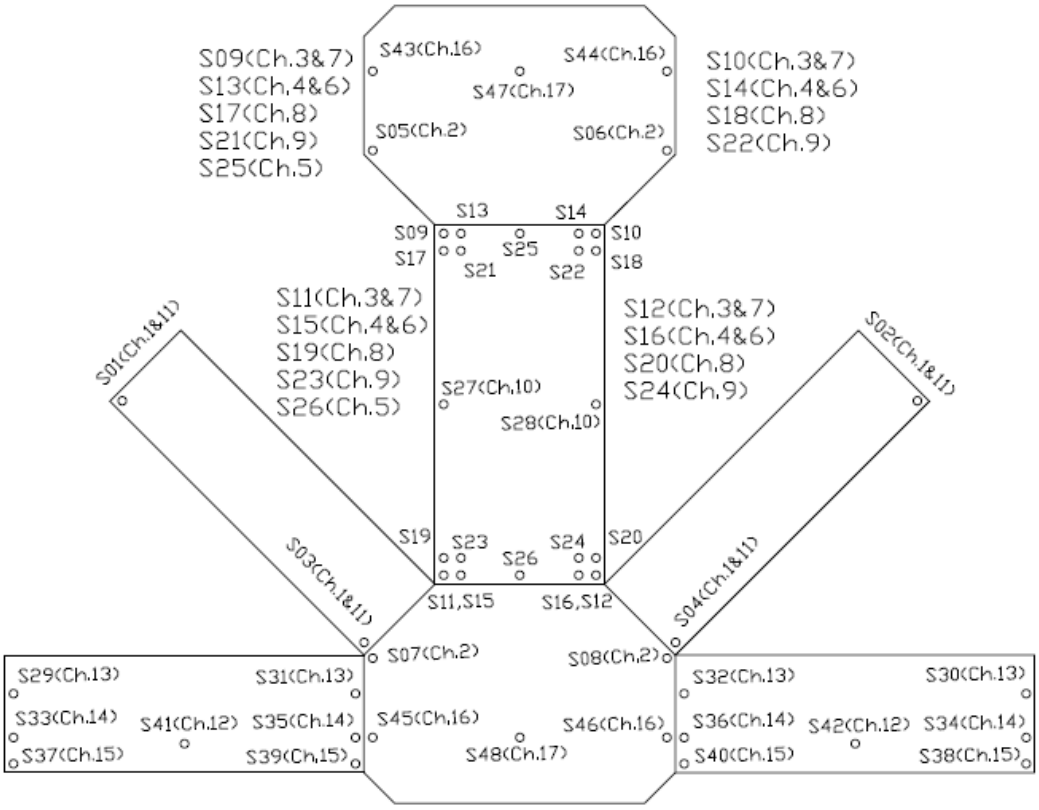

Figure 5.4: Sensor locations for numerical simulations

5.3.1 Case 1: transverse motion at 30% filling level

Figure 5.5 illustrates the trajectory of the LNG tank center for Case 1 in prescribed transverse motion. In the first half period, a modulation function is applied to buffer the tank motion and prevent excessive fluid motion from the rest state. After that, the normal tank motion is prescribed and advanced periodically. It can be found that the trajectory of the tank motion after the first half period is elliptic but asymmetric with respect to the *x* and *z* axis. Besides the translatory motions, the tank also experiences an angular motion with a maximum angle of $\pm 0.344^{\circ}$.

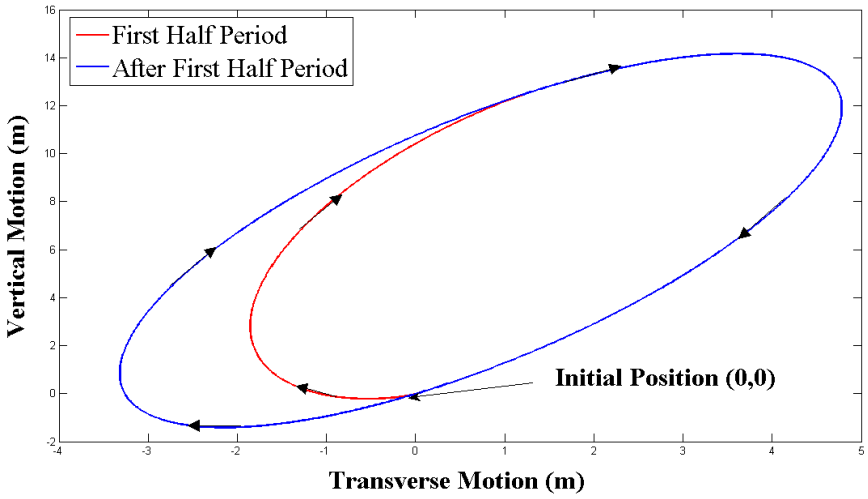

Figure 5.5: Tank motion trajectory in Case 1

Figure 5.6 shows the impact pressure at the location corresponding to the pressure sensor Ch. 15 in model test. Note that Ch. 15 is located on the bottom of vertical side wall in transverse direction and is slightly above the upper knuckle point of

the low chamber, where is submerged under the water in the initial condition. In the simulation, sensors S37-S40 are located at the position of Ch.15 or its mirror image positions. S37 and S39 are located on the same vertical wall; while S38 and S40 are situated on the opposite vertical wall. Due to the asymmetrical behavior of the tank motion shown in figure 5.5, there exhibit distinct pressure patterns for the location on different walls. The pressure histories at S38 and S40 display "double-peak" pattern in the same phase; while the pressure histories at S37 and S39 show "single-peak" pattern in another same phase. The phase difference between "double-peak" and "single-peak" is about a half-period phase shift.

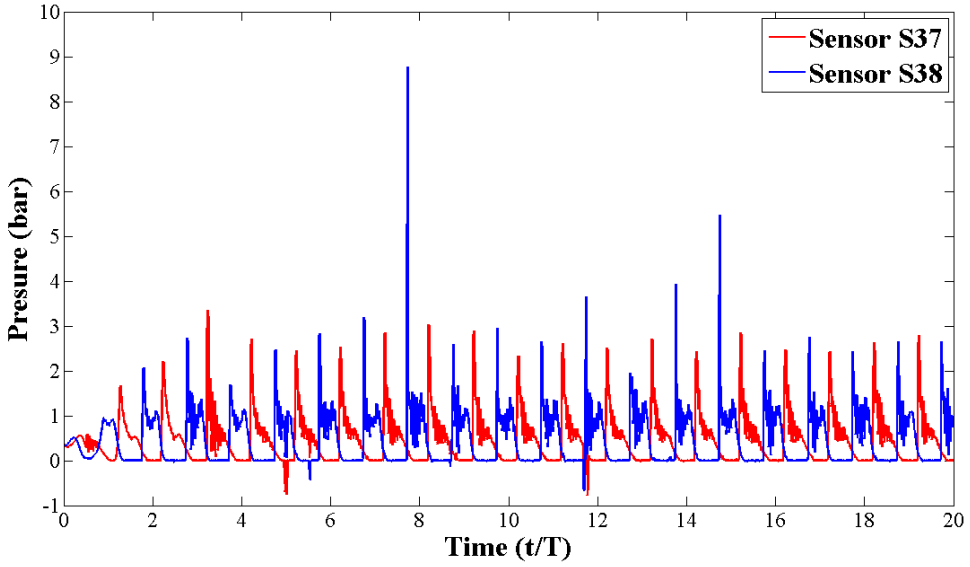

(a) Impact pressure at sensor locations S37, S38

Figure 5.6: Impact pressure histories by the CLSVOF method in Case 1

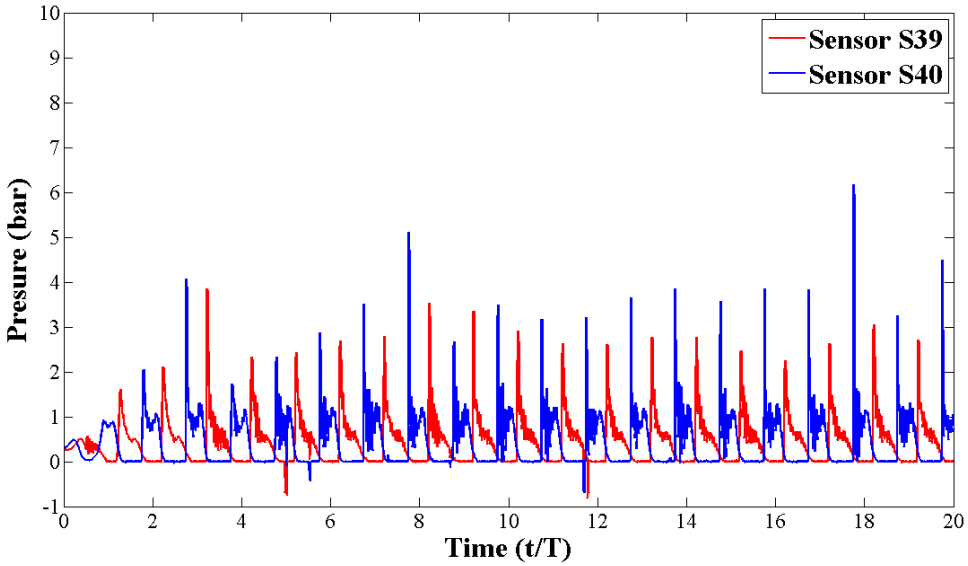

(b) Impact pressure at sensor locations S39, S40

Figure 5.6: (Continued)

Because the pressure history at Ch.15 behaves "double-peak" pattern, it indicates that sensor S38 and S40 are on the same side wall with Ch.15. The impact pressure history at sensor S40 is chosen for the following comparison with experimental data and numerical data by pure LS method. In figure 5.7, the pressure at sensor location S40 is compared with the experimental result. The peak impact pressures are somewhat lower in the first five periods than the experimental peak pressures in the same periods. However, the predicted impact peak pressures are in the good agreement with those in experiment after the first five periods. The under-predicted peak pressures within the first several cycles can be explained by that the sloshing flow does not achieve the stable state accompanying with the tank motion in the first several periods.

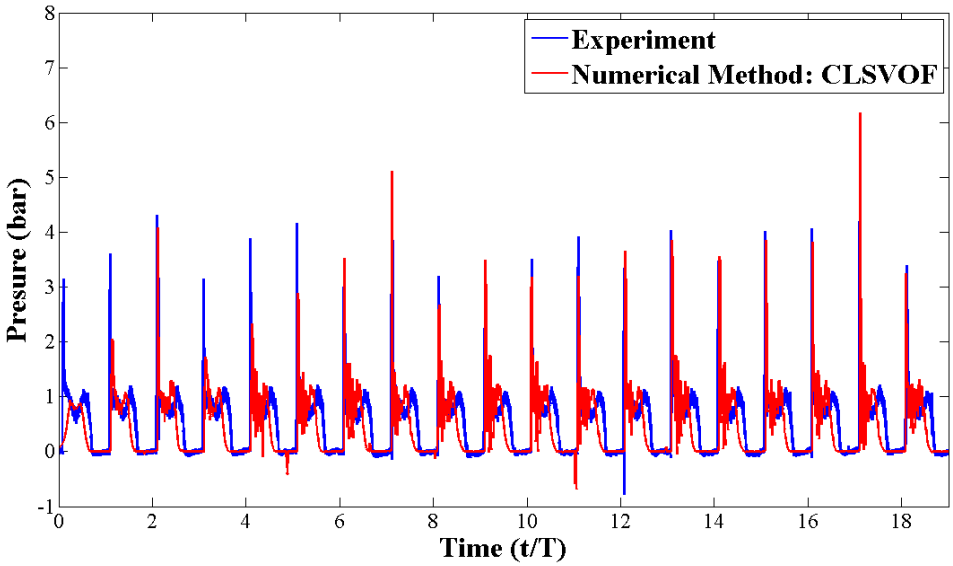

Figure 5.7: Comparisons of measured and predicted pressures in Case 1

Figure 5.8 shows the comparisons of two predicted pressures by the CLSVOF method and an improved level set method. It has clarified the level set method as an efficient numerical method to capture the smooth interface with the flaw in mass loss. Yu and Chen proposed an improved level set method for the particular sloshing flow case [54], [55]. In the improved level set method, besides the regular re-distance algorithm, the LS function is adjusted to re-gain the mass loss. Since the sloshing flow is confined in an enclosed tank, the total mass is constant during the entire process, which is convenient to compute the mass change. The mass conservation of sloshing flow can greatly help predicting the maximum impact pressures on wall. In figure 5.8, the impact peak pressures by improved level set method are larger than those by the CLSVOF method. It has demonstrated that the peak pressures by the CLSVOF method are in good

agreement with the peak pressures in experiment in figure 5.7. It indicates that the impact peak pressures by improved level set method are over-predicted. It can be explained by the mechanism of mass conservation in improved level set method. The mechanism of mass conservation in improved level set is only responsible for making up the mass loss by adjusting the LS function. Normally, it relies on the change of the integral LS function system but there are not any modifications for the LS function in local region. In other words, all of the mass loss may be repaid to the fluid attached on wall and contribute to the impact pressure on wall at all.

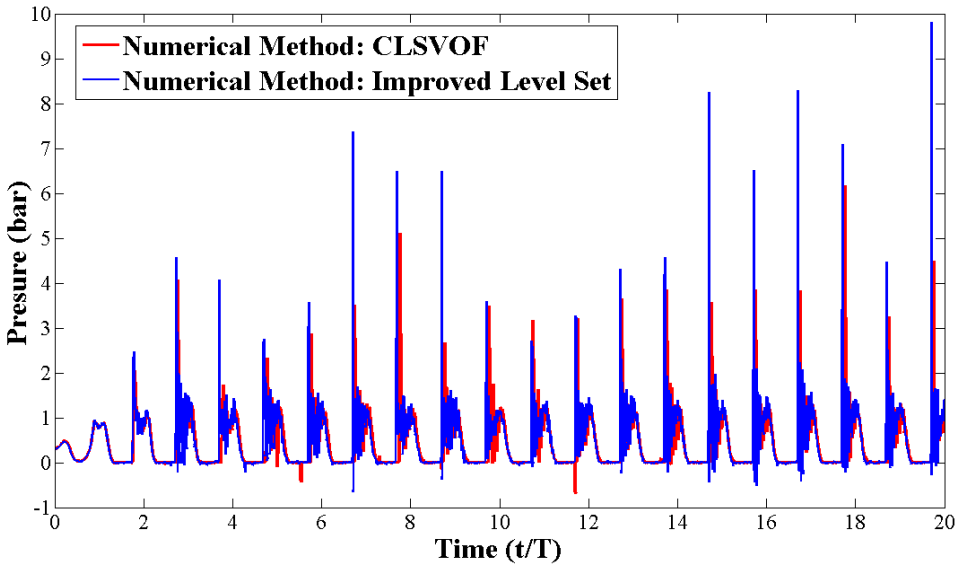

Figure 5.8: Predicted pressures by CLSVOF and improved LS method in Case 1

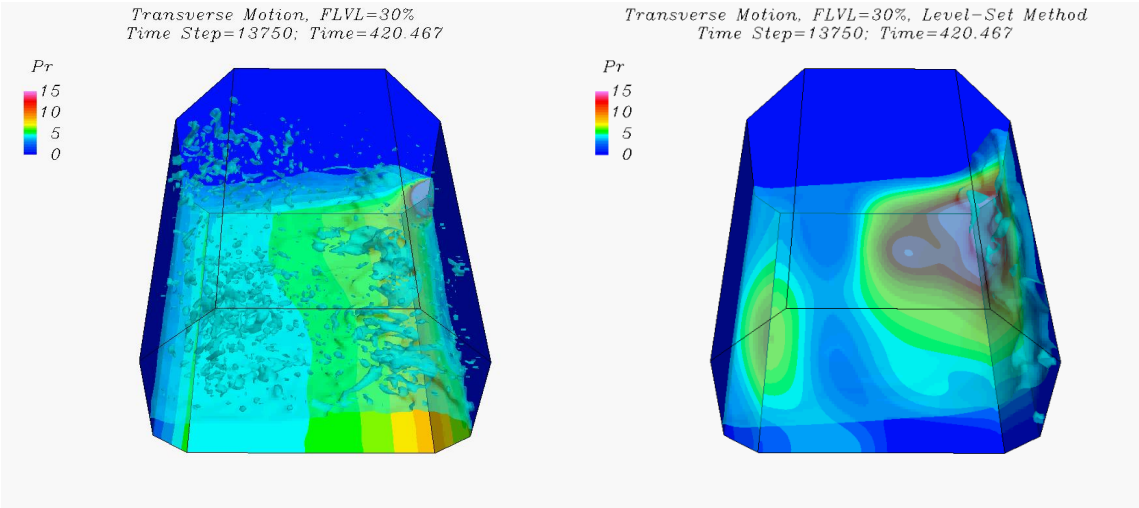

(a) t/T = 13.75

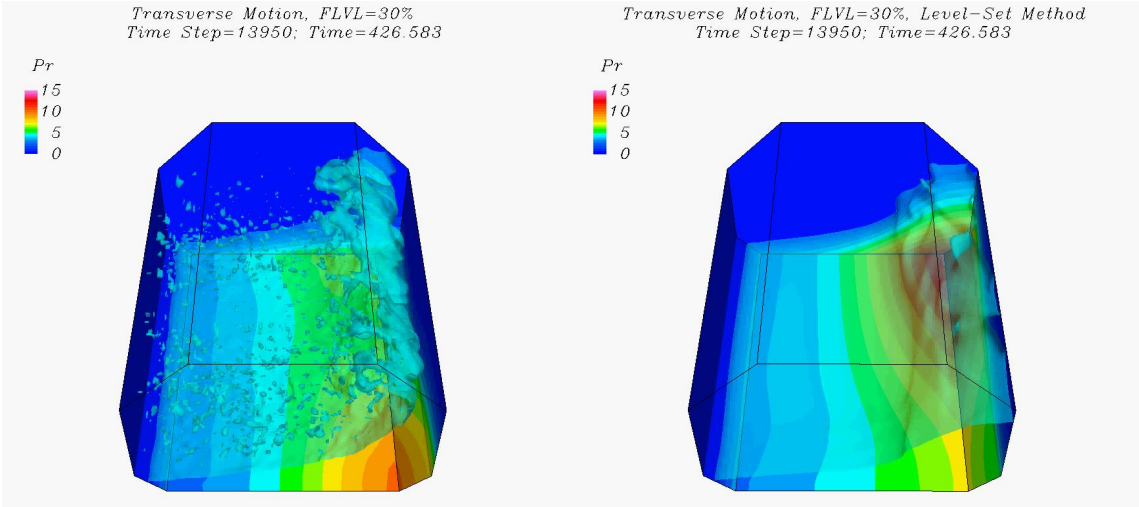

(b) t/T = 13.95

Figure 5.9: Free surface pattern and wall pressure contours in Case 1

(Left column: the CLSVOF method; right column: the improved level set method)

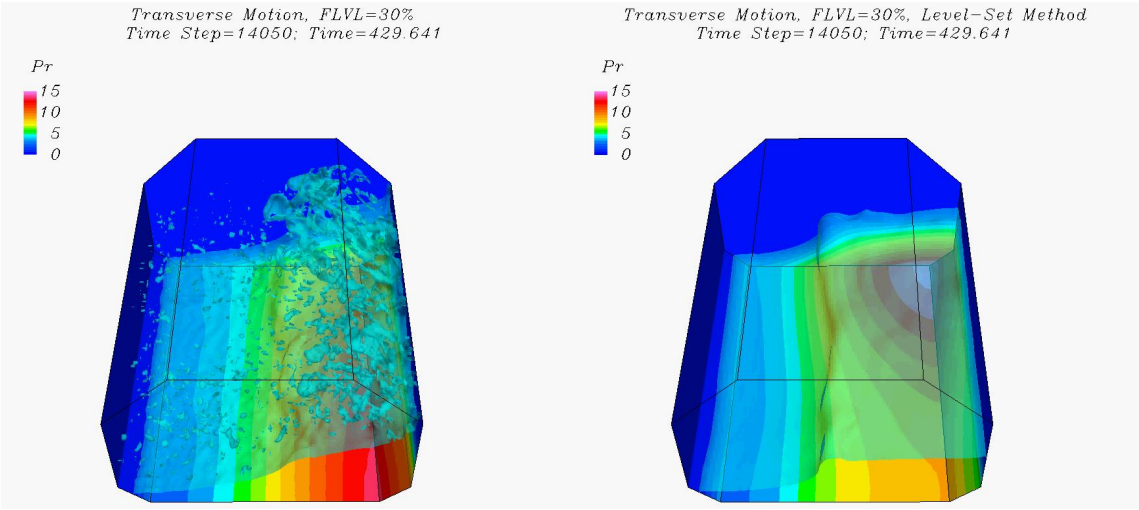

(c) t/T = 14.05

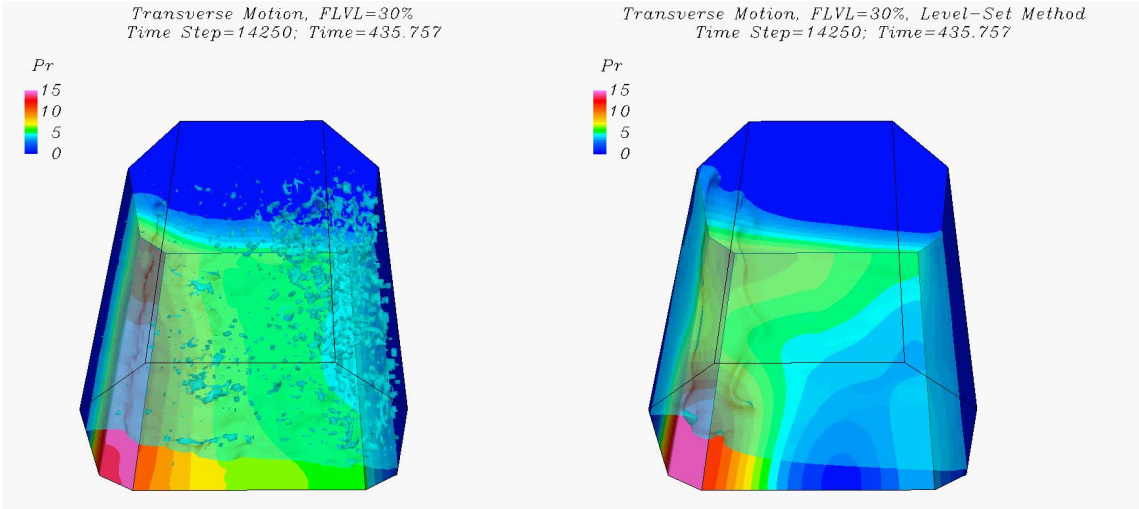

(d) t/T = 14.25

Figure 5.9: (Continued)

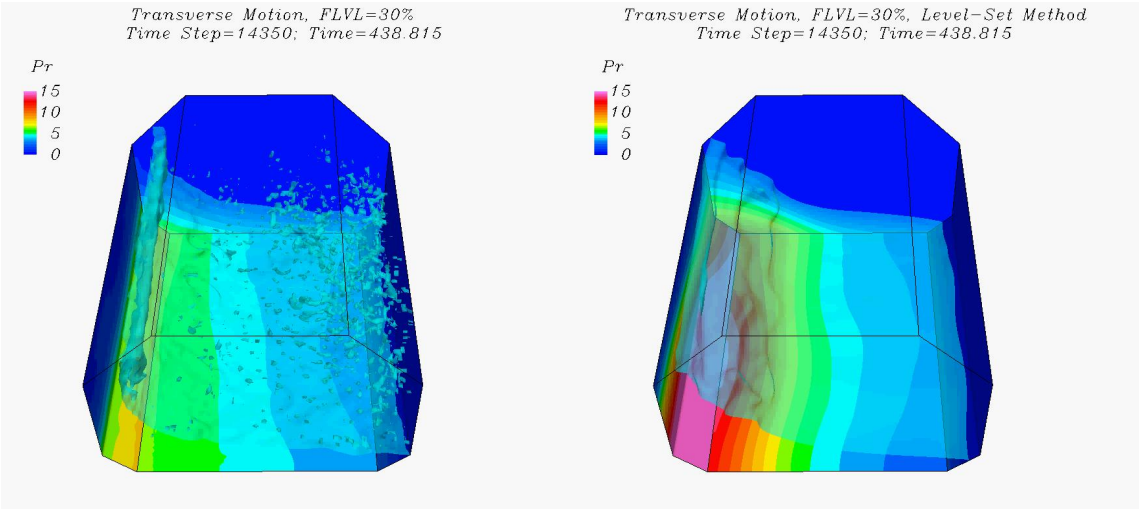

(e) t/T = 14.35

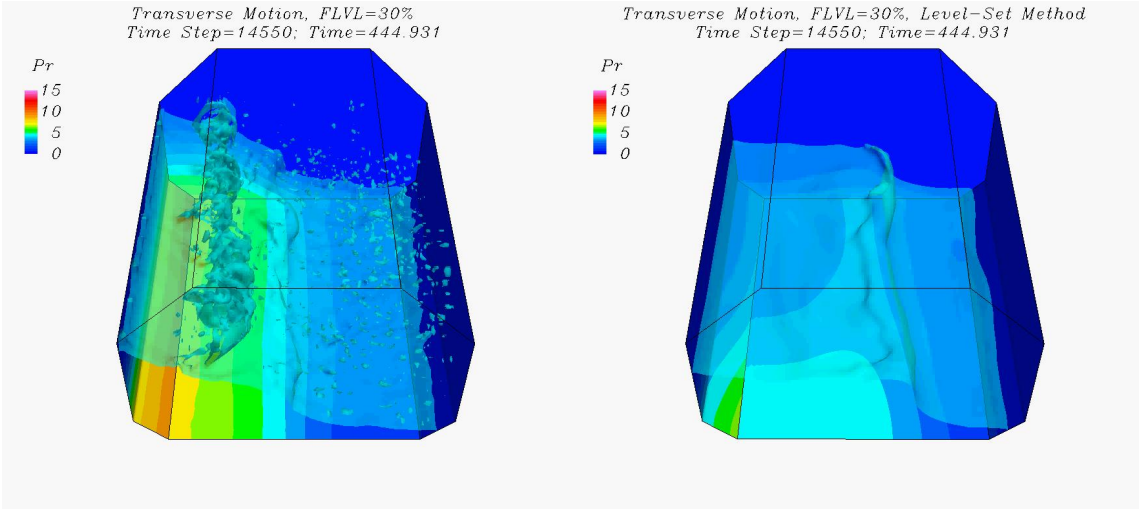

(f) t/T = 14.55

Figure 5.9: (Continued)

Figure 5.9 shows the snapshots of predicted three-dimensional sloshing flow patterns and pressure contours on the tank walls at six different time instants using the CLSVOF method and the improved level set method. As the tank moves to one side, the

fluid is driven by the tank motion to the same direction. Due to the large velocity of tank at that moment, the water moves rapidly and strongly impacts the side wall. It leads to the first impact peak pressure in the "double-peak" pattern. From the figure 5.5, even though the tank reaches the maximum horizontal displacement, the tank continues to move upward to the maximum vertical displacement on only one side. It can result in the other impact peak pressure in the "double-peak" pattern (sensor S38, S40). On the other side, the maximum vertical displacement is done before tank reaches to the maximum horizontal displacement. The pressure history on the same side wall only behaves the "single-peak" pattern (sensor S37, S39). After the tank moves back to original position, the fluid with massy kinetic energy starts to climb along the side vertical wall until the kinetic energy is used up by the gravity. The jet flow along the side vertical wall begins to collapse and develop overturning pattern in air region. As the thickness of the flow is decreasing, the strip of flow is broken into numerous separated droplets which permeate the air. Finally, most of the droplets return to the main part of water due to gravity. It is also observed that the CLSVOF method can capture more details about the interface breaking into the small droplets; while the level set method smoothes the interface and discard such particular phenomena.

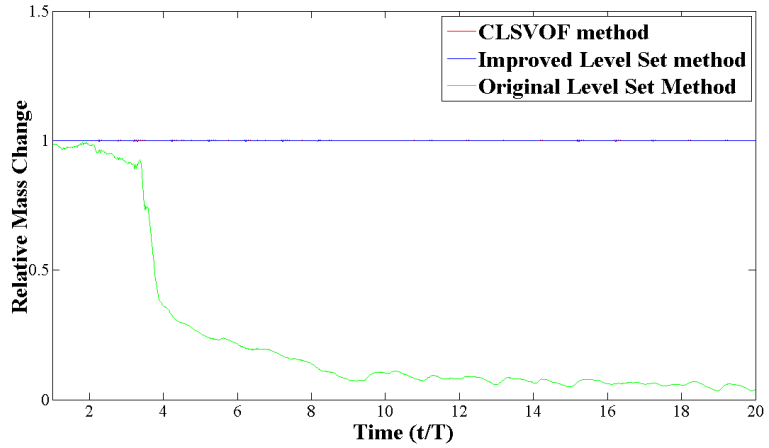

(a) Relative mass change by CLSVOF, improved LS and LS

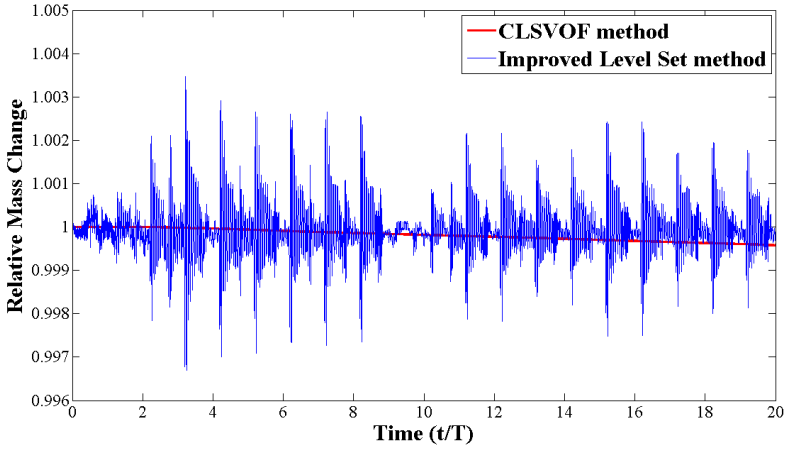

(b) Relative mass change by CLSVOF and improved LS

Figure 5.10: Relative mass change in Case 1

Figure 5.10 shows the time history of the relative mass change by the three numerical methods: the CLSVOF method, improved level set method and the original level set method. The original level set method without particular mass conservation mechanism lost almost 96.11% of the initial mass after 20 periods. The CLSVOF and

improved level set methods preserve good mass conservation all the time. However, the mass change by the improved level set method displays more fluctuations around the initial mass, because the “global” mass conservation mechanism adjusts the mass based on the known mass loss or mass gain. The mass change by the CLSVOF method shows more stable history because the essence of the mass conservation origins from the interface advection algorithm. The numerical error is only the factor to affect the mass change in the CLSVOF method.

5.3.2 Case 2: transverse motion at 50% filling level

Figure 5.11 illustrates the trajectory of the LNG tank center for Case 2 in prescribed transverse motion. A modulation function is again implemented in the first half period of the tank motion to prevent the impulsive start. Different from the trajectory in Case 1, the initial tank position starts from the upper half of the motion trajectory, which induces the out of phase motion with that in Case 1. In addition, the amplitudes in horizontal, vertical and rotational motions are all somewhat smaller than those in Case 1.

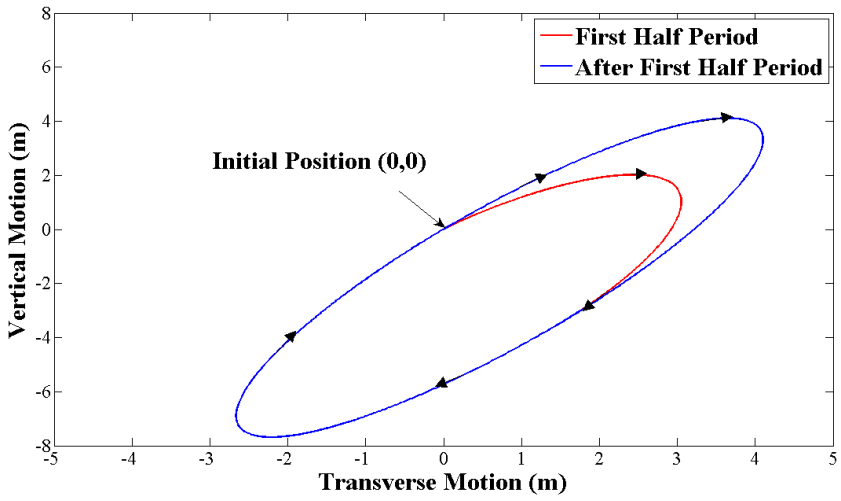

Figure 5.11: Tank motion trajectory in Case 2

Figure 5.12 shows the results of impact pressures at pressure sensor locations S1, S2, S3 and S4 which are corresponding to Ch. 11 and its mirror images. The sensor Ch. 11 is located on the inclined surface where is slightly above the lower knuckle corner point of the upper chamber. And the position is above the initial water level. The pressure patterns exhibited by all four sensors are close to "single-peak" pattern. But there exist the distinct pressure peaks among them, which indicates that the behavior of the sloshing flow is chaotic and strongly three-dimensional. The chaotic three-dimensional effect is more and more significant after the initial several cycles.

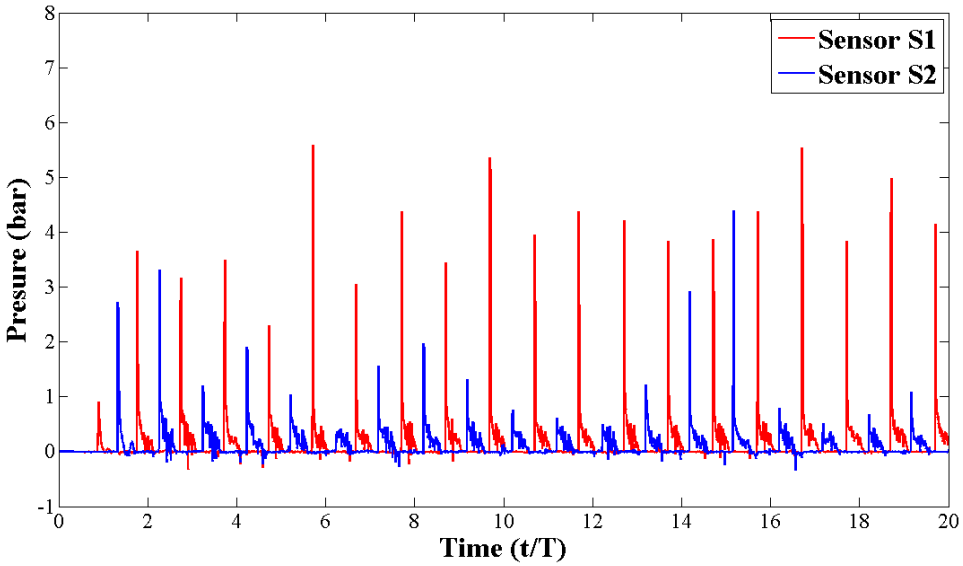

(a) Impact pressure at sensor locations S1, S2

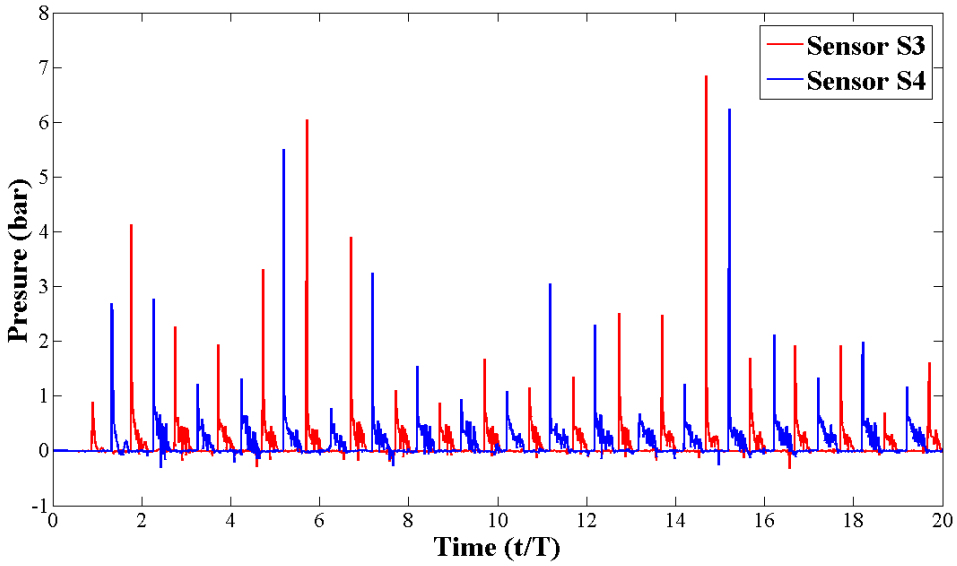

(b) Impact pressure at sensor locations S3, S4

Figure 5.12: Impact pressure histories by the CLSVOF method in Case 2

The largest impact pressure peak tends to occur at sensor S1 which is selected to compare with the experimental data. In figure 5.13, the general pressure history at sensor location S1 is in close agreement with the pressure history of Ch. 11 in experiment. The impact pressure peaks in the CLSVOF method are slightly over-predicted at large t/T. This can be attributed to the sloshing flow which is more three-dimensional and produced a more highly localized impact on the tank walls. When the position of Ch. 11 is slightly deviated from grid point, the apparently different impact pressure peaks are captured.

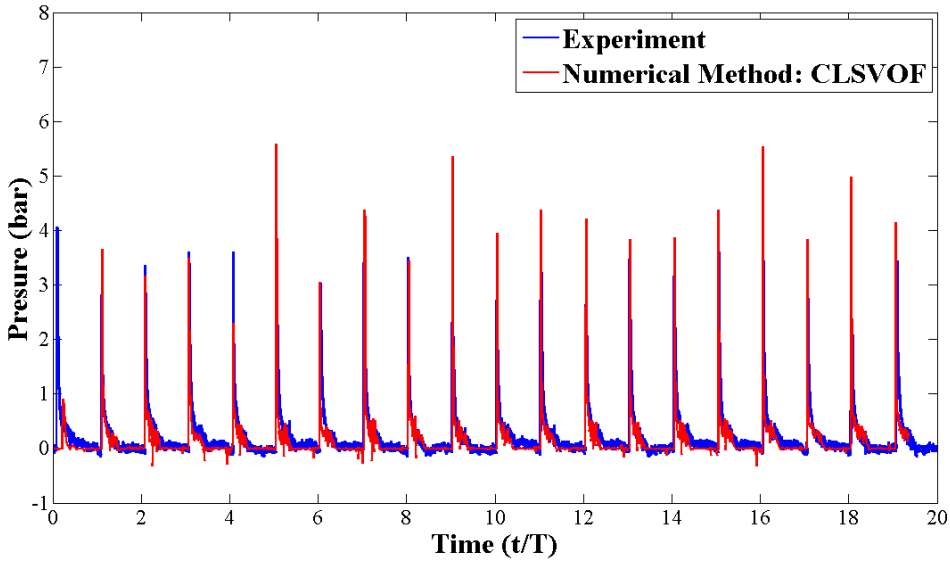

Figure 5.13: Comparisons of measured and predicted pressures in Case 2

The impact pressure history at the location of sensor S1 using the CLSVOF method is also compared with the results by the improved LS method. From figure 5.14, both the general shape and the pressure peaks are closely similar. The only difference is

that the CLSVOF method can capture somewhat higher impact pressure peaks in the first about 10 periods. Since the impact pressure peaks in experiment are closer to the results by the CLSVOF method, it implies that the sloshing flow by improved level set method may not achieve the stable state with the tank motion in the first ten cycles. The other explanation is also the "global" mass conservation mechanism in improved level set method. On the contrary to the explanation in Case 1, most of mass loss may be added back to the interface at tank bottom, whereas few of mass are distributed to attach the side wall. Because the "global" mass conservation mechanism cannot specify the mass distribution locally, it is not able to accurately match the actual impact pressure peaks.

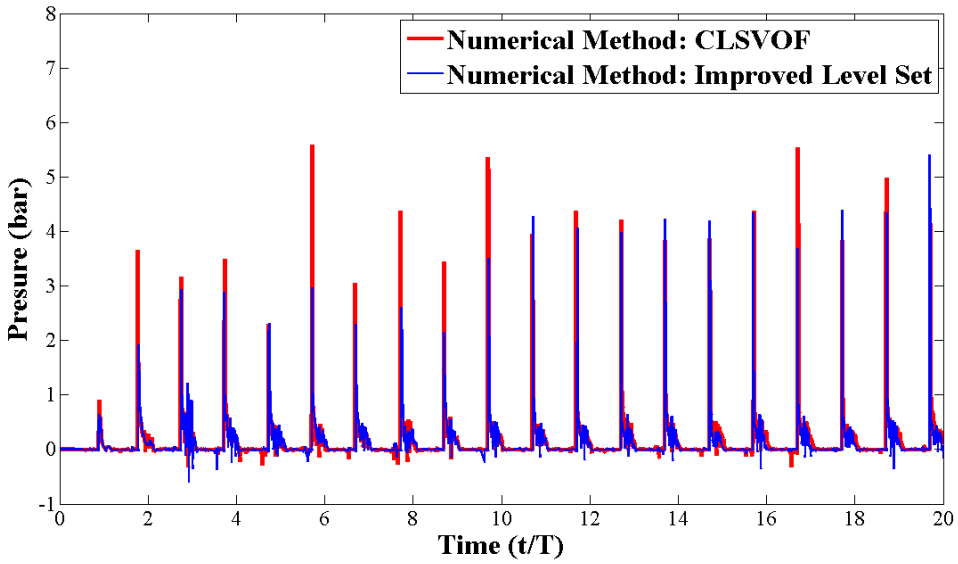

Figure 5.14: Comparisons of predicted pressures in Case 2

Figure 5.15 shows the snapshots of predicted three-dimensional sloshing flow patterns and pressure contours on the tank walls at six different time instants using the CLSVOF method and the improved level set method. When the flow climbs up to the inclined wall on top, the sloshing flow patterns behave the strongly chaotic and three-dimensional, even though the excitation motion is strictly prescribed in two-dimensional. More specifically, a swirling motion occurs in this case. As a result of the 3D swirling flow pattern, the impact pressure histories in figure 5.12 behave distinctly at large t/T, even though these four sensors are located at mirror image positions. The free surface patterns by the CLSVOF method and the improved level set method are generally similar. But the CLSVOF method has the capability to represent the process of breaking flows, which are also observed in experiment.

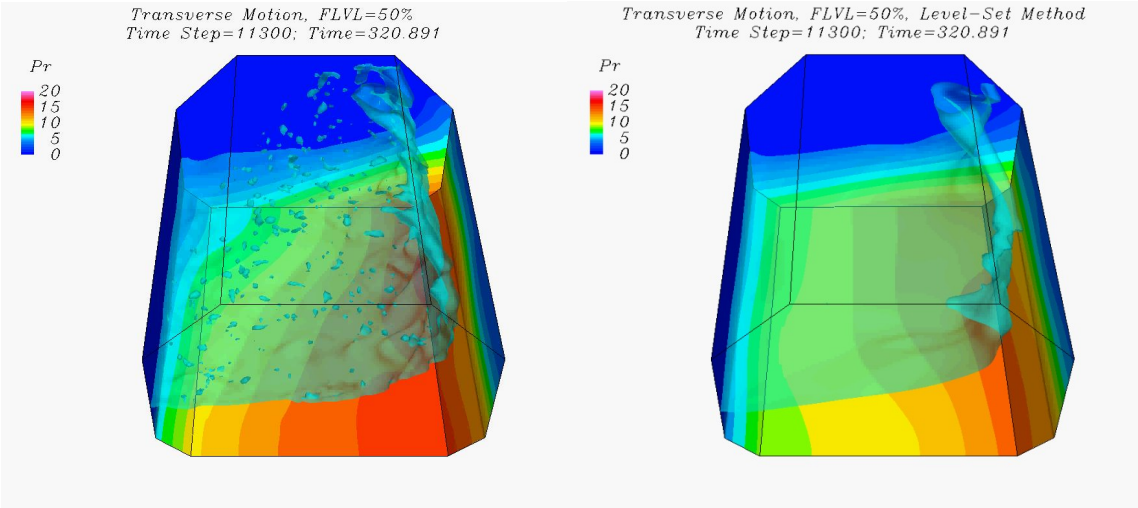

(a) t/T = 11.30

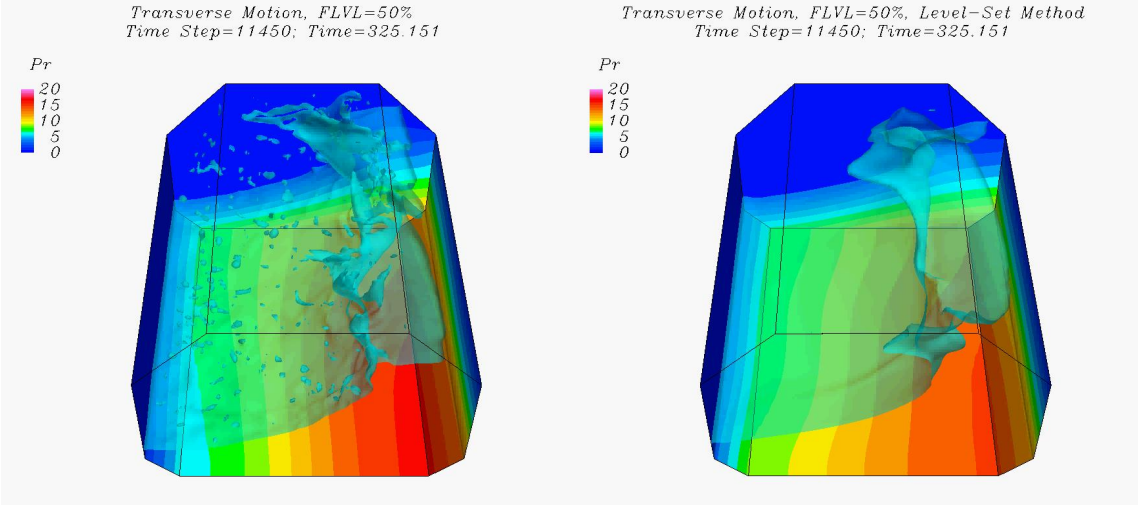

(b) t/T = 11.45

Figure 5.15: Free surface pattern and wall pressure contours in Case 2

(Left column: the CLSVOF method; right column: the improved level set method)

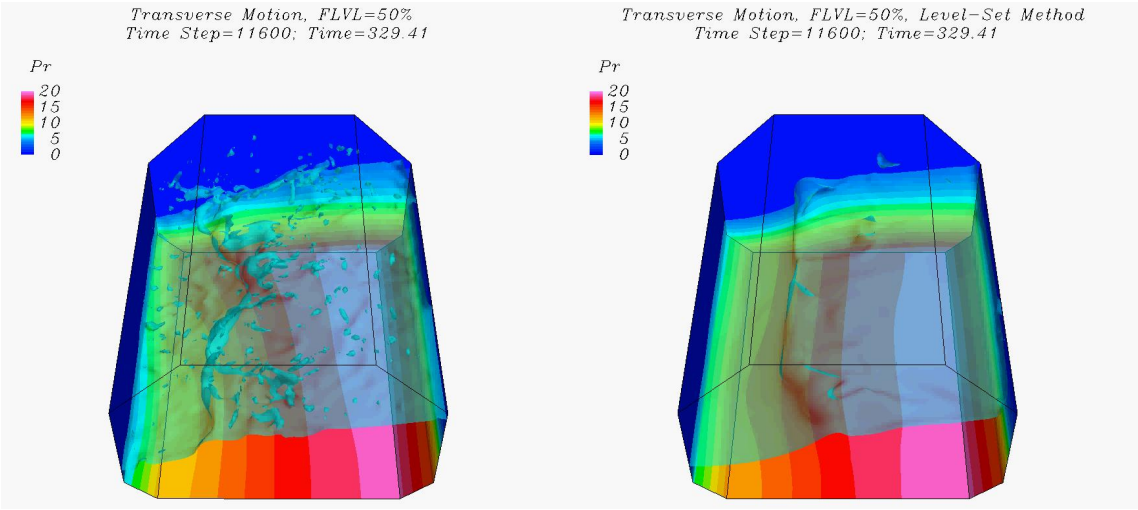

(c) t/T = 11.60

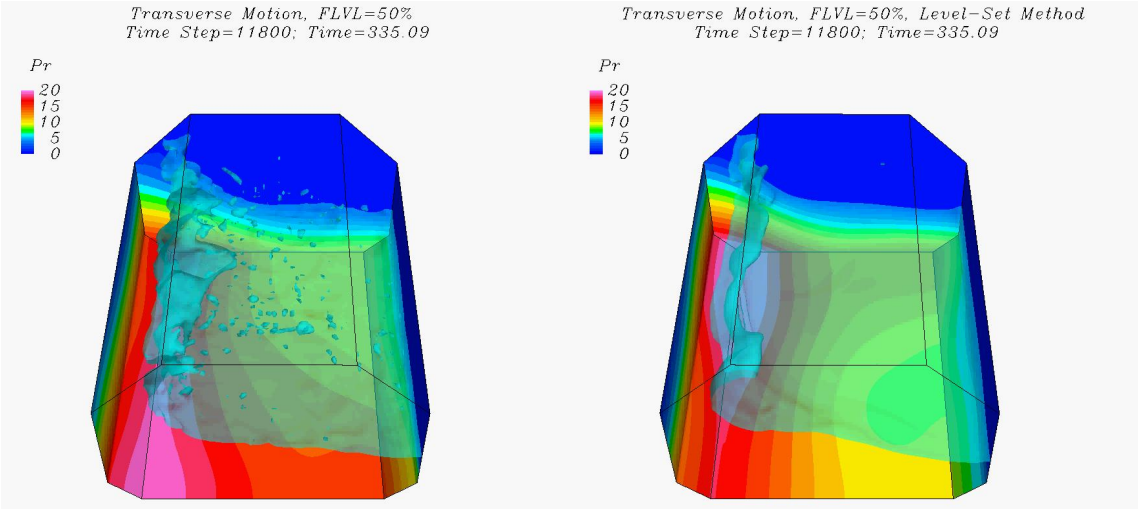

(d) t/T = 11.80

Figure 5.15: (Continued)

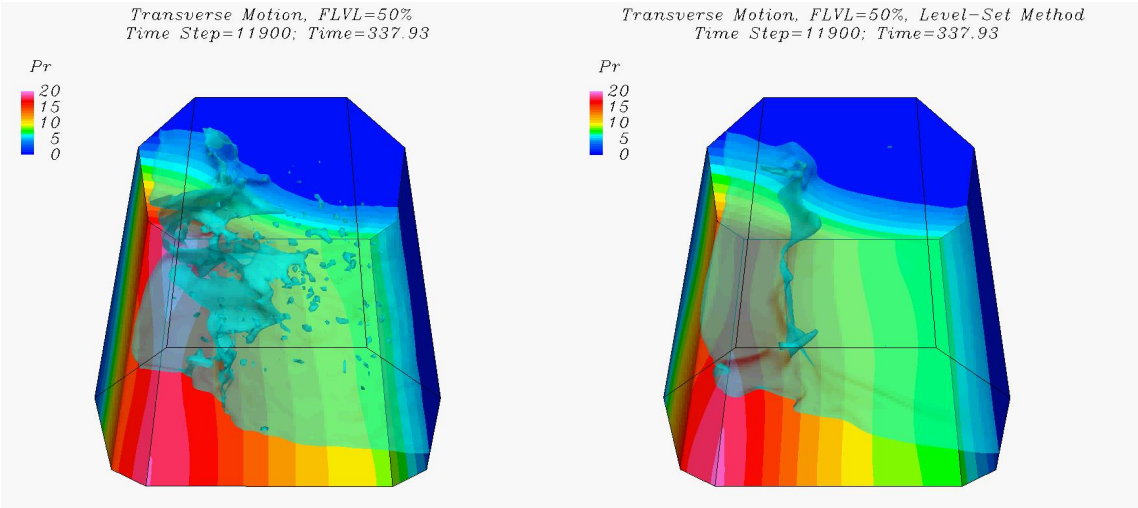

(e) t/T = 11.90

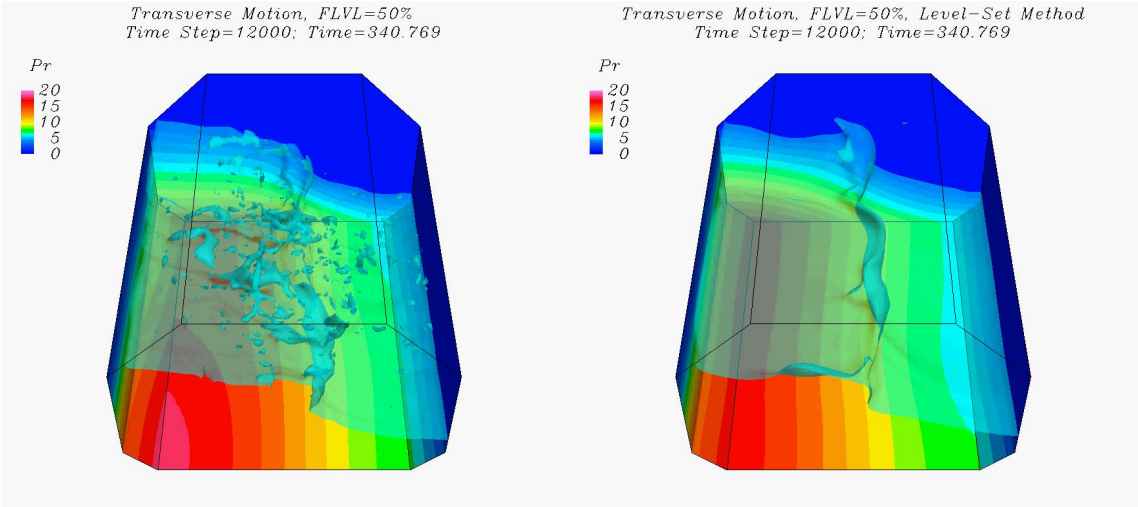

(f) t/T = 12.00

Figure 5.15: (Continued)

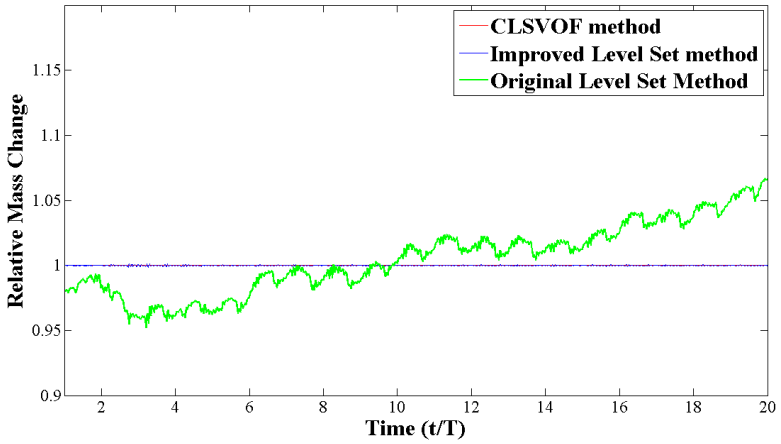

(a) Relative mass change by CLSVOF, improved LS and LS

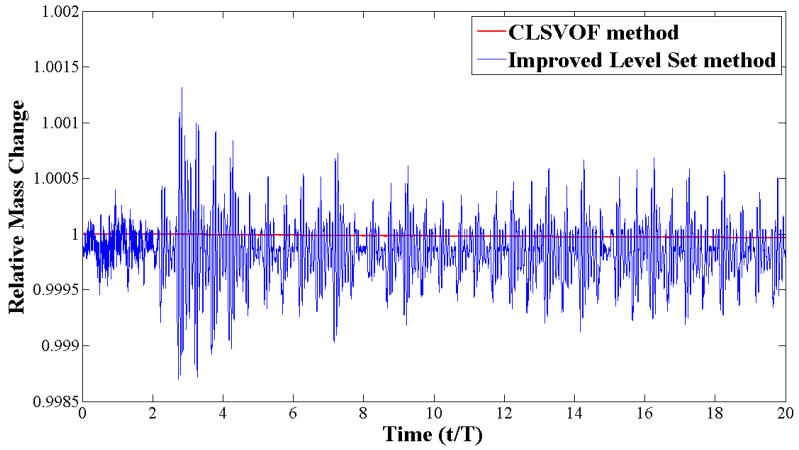

(b) Relative mass change by CLSVOF and improved LS

Figure 5.16: Relative mass change in Case 2

Figure 5.16 shows the time history of the relative mass change by the three numerical methods: the CLSVOF method, improved level set method and the original level set method. The original level set method without particular mass conservation care gain extra 6.6% of the initial mass after 20 periods. The improved level set method also

cannot achieve the exact mass conservation all the time, compared with the CLSVOF method.

5.3.3 Case 3: longitudinal motion at 80% filling level

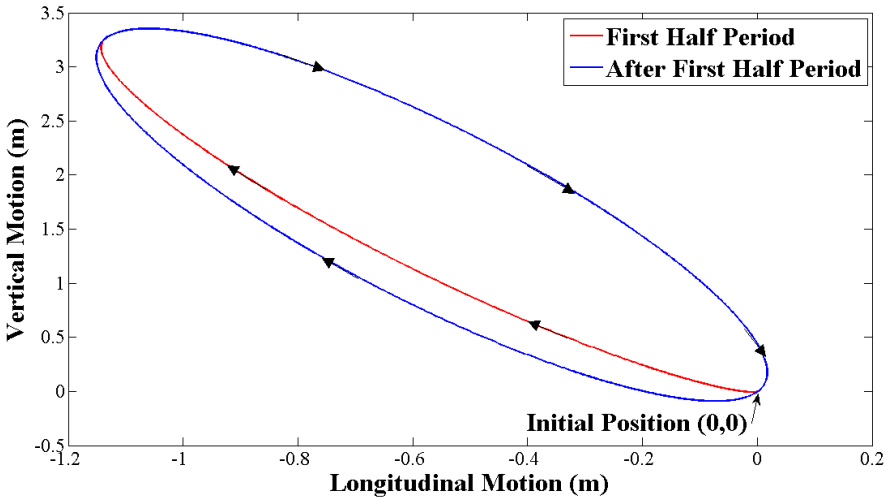

Figure 5.17: Tank motion trajectory in Case 3

Figure 5.17 illustrates the trajectory of the LNG tank center for Case 3 in prescribed longitudinal motion. Similar with the trajectories for Case 1 and Case 2, there is a transition motion from the start to the regular motion of the tank. The location of Ch. 7 in experiment is looked into in this case. The sensors S9, S10, S11 and S12 are located at the positions of Ch.7 and its mirror images, which are the four corner points of the tank top ceiling. Only when the sloshing flow is slamming on the top ceiling, can the impact pressure be predicted. It is found that the impact pressure history only at location of S11 displays high impact peaks continuously since the 10^{th} cycle. Therefore, the

simulation is extended for total 30 periods to fully capture the stable impact pressure history in figure 5.18.

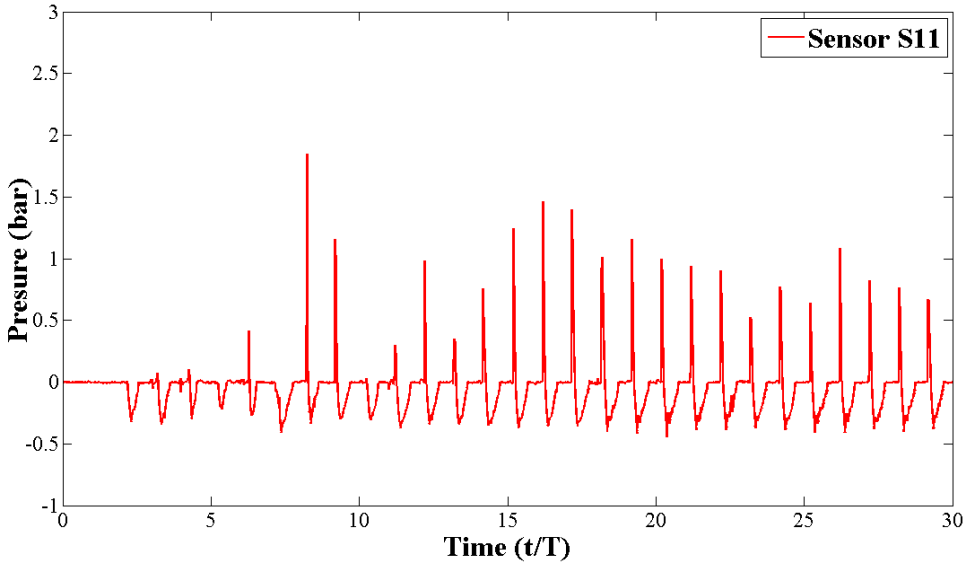

Figure 5.18: Impact pressure histories by the CLSVOF method in Case 3

Figure 5.19 shows the comparison between the predicted pressure at sensor S11 and the measured pressure at Ch. 7 in experiment. The general pressure history at sensor location S11 is in close agreement with the pressure history of Ch. 7 in experiment. Similar to the experimental results, the negative pressures can be observed in predicted pressure history. These negative pressures are attributed to the suction of the water interface receding from the tank ceiling. The negative pressures immediately follow the impact peak pressures in the same cycle. It is noticed that the negative pressures start acting upon the tank ceiling just before the interface of the water is going to leave the top

ceiling. Once the interface is completely unattached to the top ceiling, the pressures on the tank ceiling restore to zero. However, the magnitudes of both the negative and positive pressure peaks in numerical results are somewhat smaller than those in experiment.

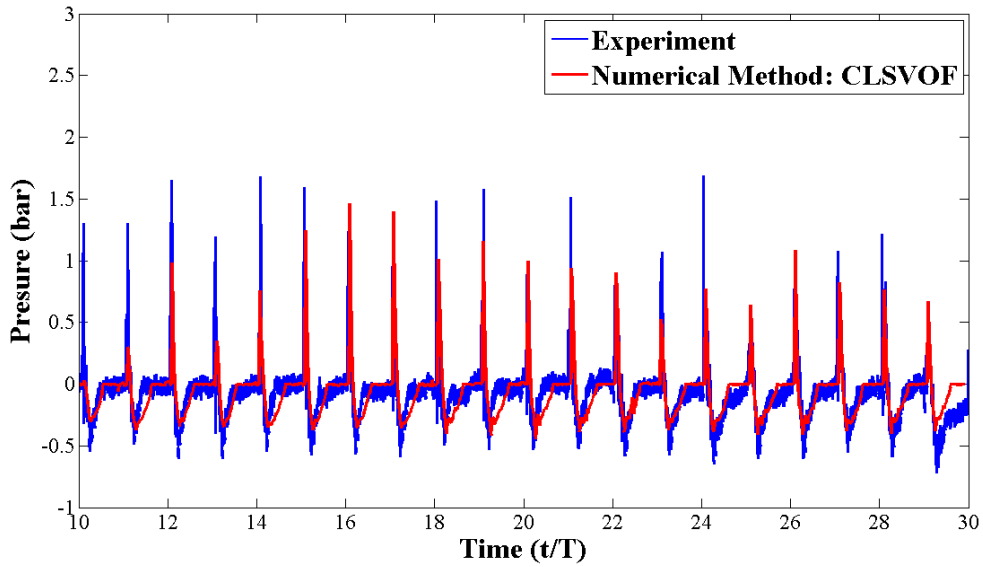

Figure 5.19: Comparisons of measured and predicted pressures in Case 3

The impact pressure history at the location of sensor S11 using the CLSVOF method is also compared with the result by the improved level set method. From figure 5.20, it can be found that the maximum negative pressures predicted by the improved level set method are close to the maximum negative pressures by the CLSVOF method. However, the positive peak pressures by the improved level set method are under-predicted. For numerical method in sloshing flow in LNG tank, it is the most challenging

task to accurately predict the pressure impacting upon top ceiling. In this case with 80% filling condition, the initial filling level is not very close to the tank ceiling. It requires the numerical method to accurately predict the interface motion and capture the agreeable peak pressures on the top ceiling. The CLSVOF method demonstrates superior capability of the interface capturing.

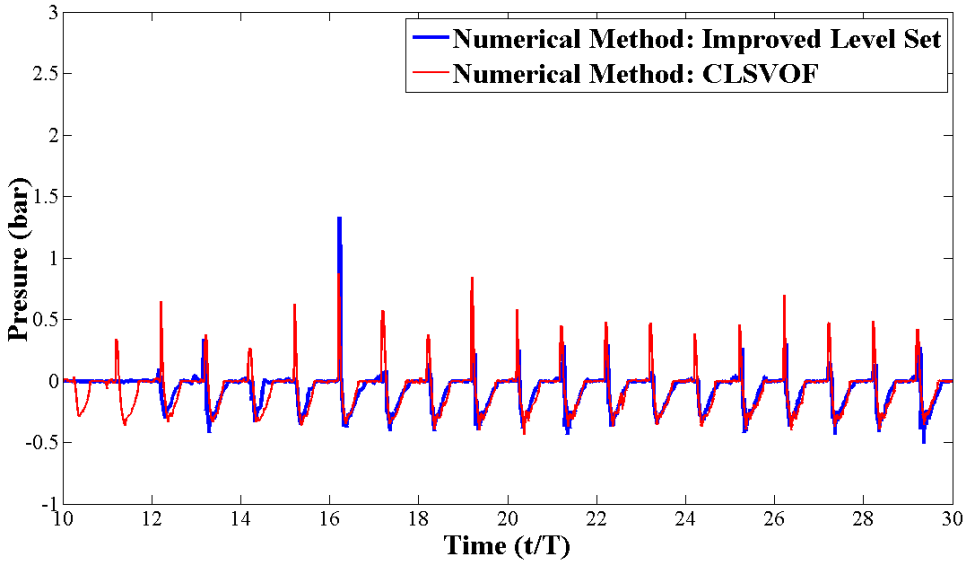

Figure 5.20: Comparisons of predicted pressures in Case 3

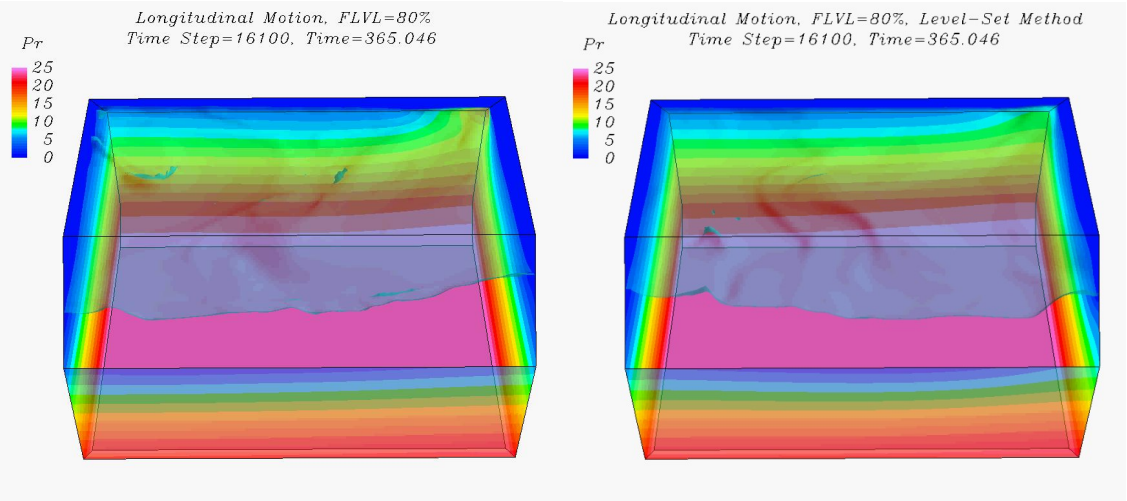

(a) t/T = 16.10

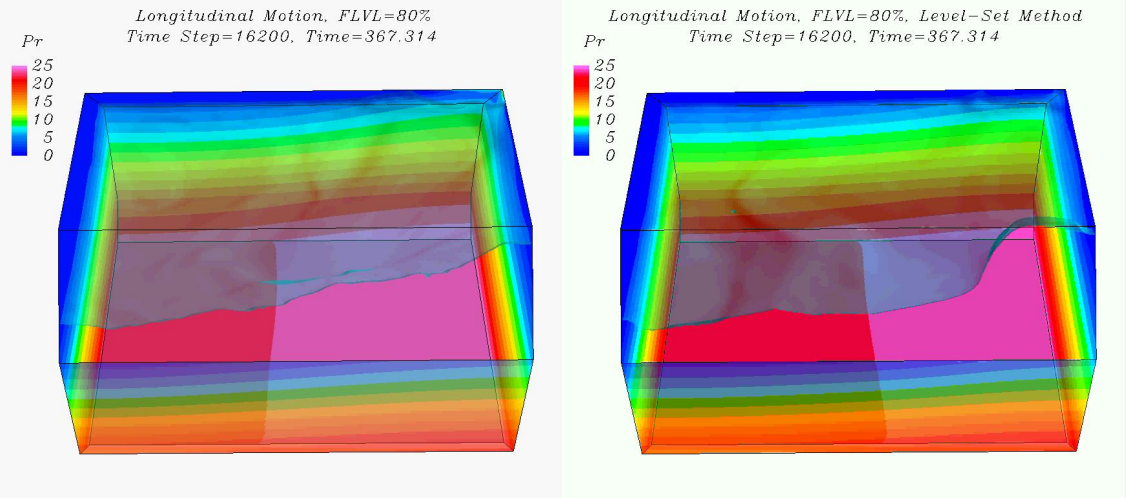

(b) t/T = 16.20

Figure 5.21: Free surface pattern and wall pressure contours in Case 3

(Left column: the CLSVOF method; right column: the improved level set method)

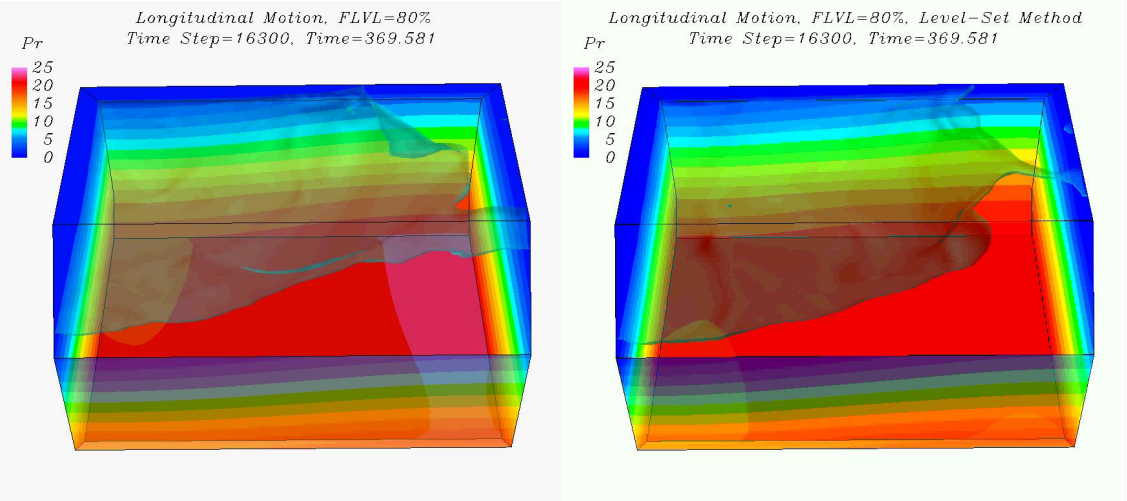

(c) t/T = 16.30

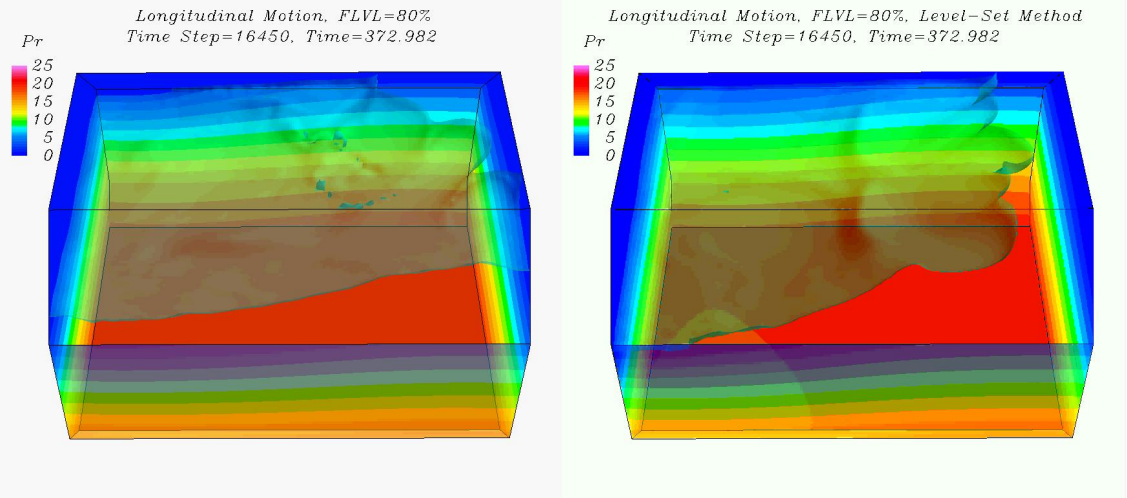

(d) t/T = 16.45

Figure 5.21: (Continued)

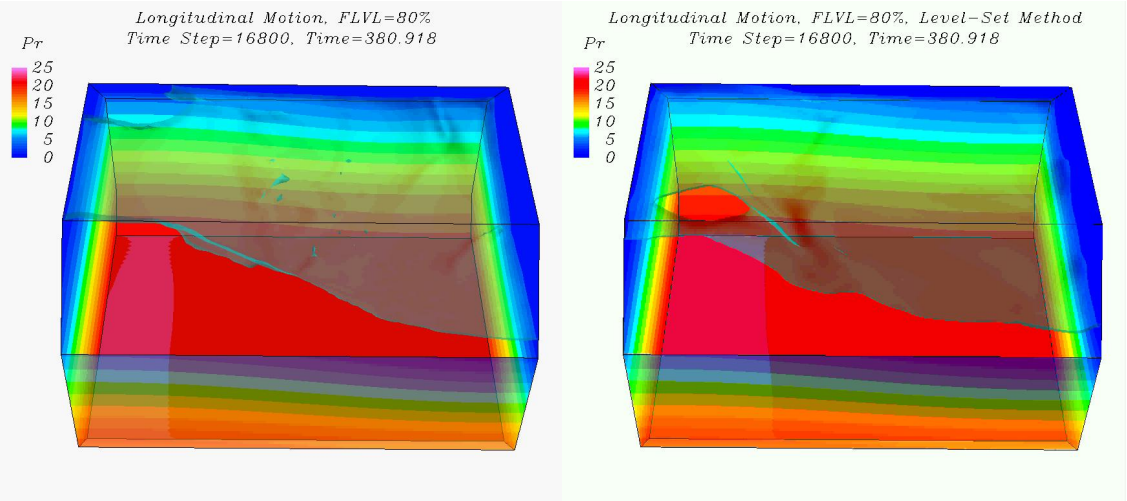

(e) t/T = 16.80

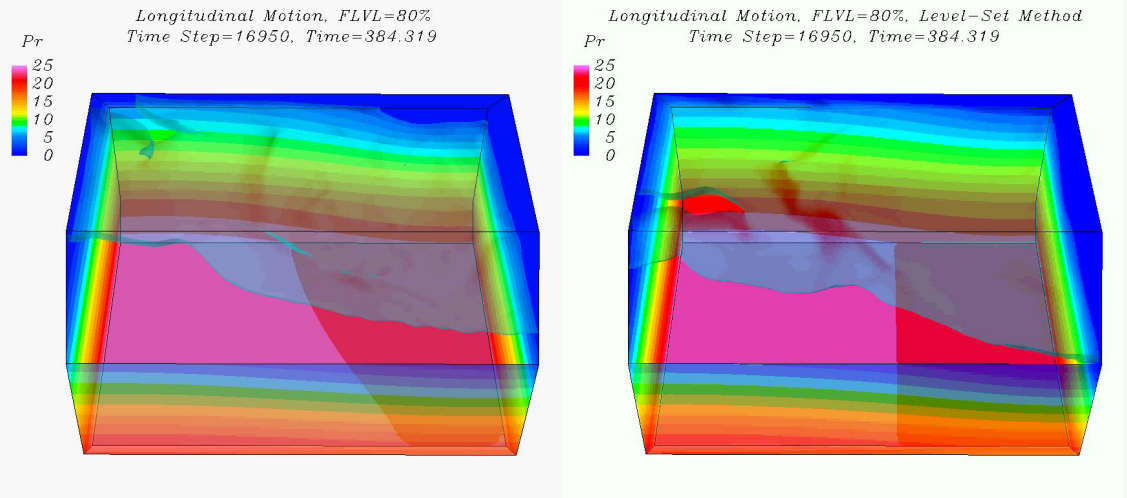

(f) t/T = 16.95

Figure 5.21: (Continued)

Figure 5.21 shows the snapshots of predicted three-dimensional sloshing flow patterns and pressure contours on the tank walls at six different time instants using the CLSVOF method and the improved level set method. The flow motion in this case performs moderate and does not display much breaking flow phenomena. It is because

the motions of tank in horizontal and vertical directions are much smaller than those in Case 1 and Case 2. Another explanation is that Case 3 is studied for high filling level. It indicates there is limited space for the development of the flow. For the selected positions located in the four corner points of top ceiling, it can be observed that there only exists a large wet area nearby one corner point. This is the reason why only the impact pressure history at location of S11 displays high impact peaks continuously. When the water hit on the location of S11, the pressure is positive impact pressure. When the water starts to recede from the top ceiling, the pressure is negative suction pressure. Because the filling level is 80%, the majority of water on bottom is still away from the top ceiling. The gravity drags the water detached from the ceiling face in a short time. Thus, the negative suction peak pressure immediately follows the positive impact peak pressure. Since the flow motion is moderate in this case without obvious breaking flow, the free surface patterns by the CLSVOF method and improved level set method are very similar.

Figure 5.22 shows the time history of the relative mass change by the three numerical methods: the CLSVOF method, improved level set method and the original level set method. The final mass by original level set method after 20 periods obtains extra 11.8% of the initial mass. Although the “global” mass conservation in improved level set method maintains roughly mass conservation, the improved level set method also cannot achieve the exact mass conservation all the time, compared with the CLSVOF method.

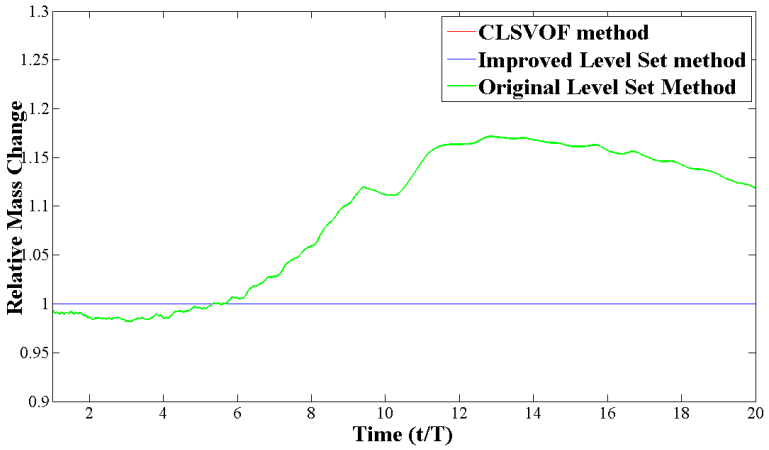

(a) Relative mass change by CLSVOF, improved LS and LS

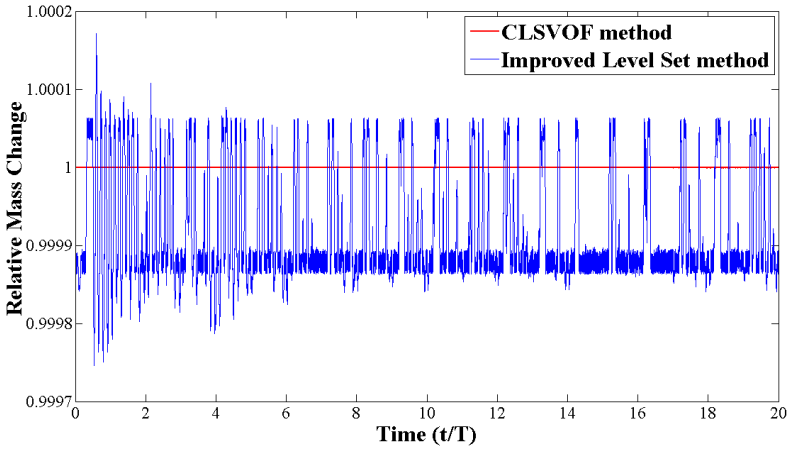

(b) Relative mass change by CLSVOF and improved LS

Figure 5.22: Relative mass change in Case 3

5.3.4 Case 4: longitudinal motion at 92.5% filling level

Figure 5.23 shows the longitudinal motion trajectory of the LNG tank for Case 4 with a 92.5% filling level. Since a 92.5% filling level is close to full tank, the air region

is confined nearby the top ceiling and the top of the upper chamfer. Ch. 3 and its mirror images are the positions of interest in this case, which are the four corner points of the tank top ceiling. Similar to Case 3, only when the sloshing flow is captured to slam upon the top ceiling, can the impact pressures be predicted.

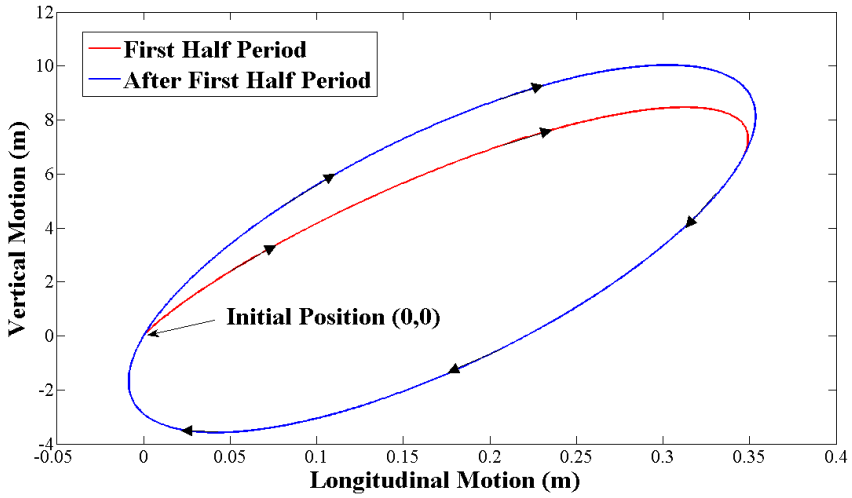

Figure 5.23: Tank motion trajectory in Case 4

Figure 5.24 shows the impact pressure histories at the locations of S9 and S10, which have the comparable peak pressures to the experimental results. The negative suction pressures after the positive peak pressures are observed. Different from the suction pressure pattern in Case 3, the pressures go down from the peaks to the lowest points in some longer time. It is because that the space for the fluid motion is more limited in the nearly full filling level condition. In addition, the magnitudes of the negative pressure are also smaller than the peak values in Case 3.

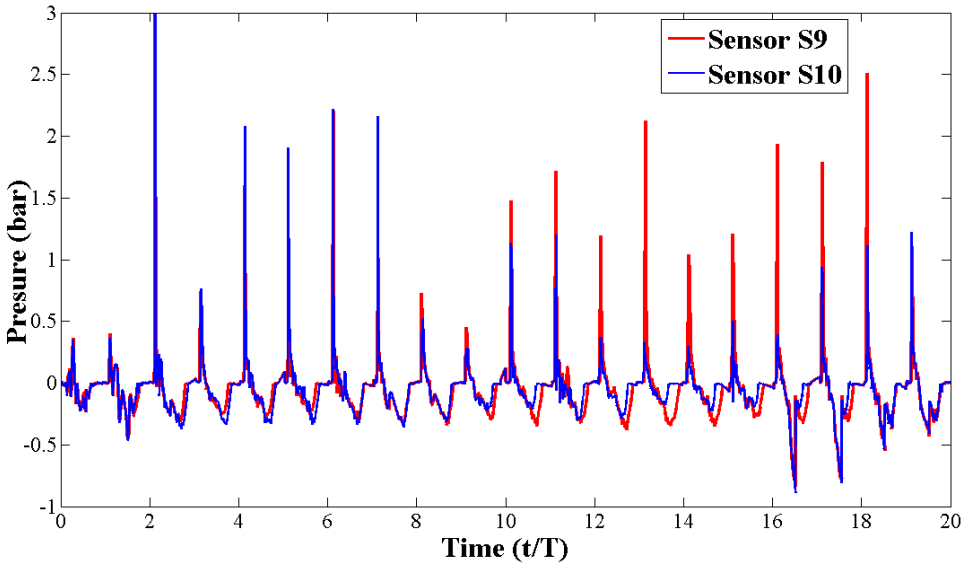

Figure 5.24: Impact pressure histories by the CLSVOF method in Case 4

Figure 5.25 (a) shows the comparison between the predicted pressures at sensor S9 and the measured pressure at Ch. 7 in experiment. Figure 5.25 (b) is the comparison between the predicted pressures at sensor S10 and the measured pressure at Ch. 7 in experiment. From the pressure history of experimental results, it is noted that the pressure history behaves more chaotic without very stable peak pressures over the cycles. In this case, the impact peak pressures between numerical and experimental results are not required to compare one period by one period. Going through the entire history, it is found that the values of the maximum impact peak pressures and the minimum impact peak pressures in numerical and experimental data are close.

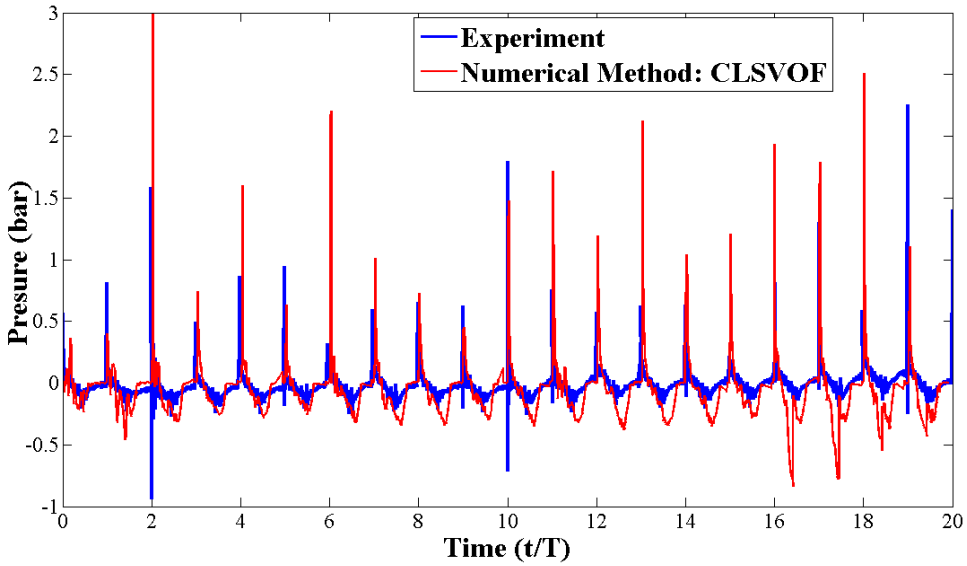

(a) At the location of sensor S9

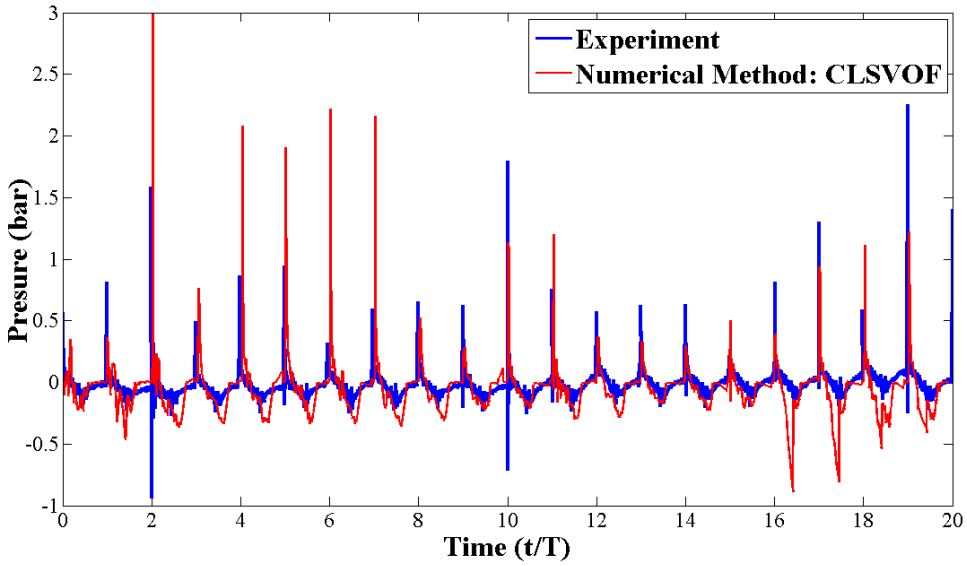

(b) At the location of sensor S10

Figure 5.25: Comparisons of measured and predicted pressures in Case 4

The impact pressure history at the locations of sensor S9 and S10 using the CLSVOF method is also compared with the results by the improved level set method in figure 5.26. Although the histories of impact pressures by the CLSVOF method and the improved level set method are also chaotic, the ranges of the impact peak pressures by both of the numerical methods are similar.

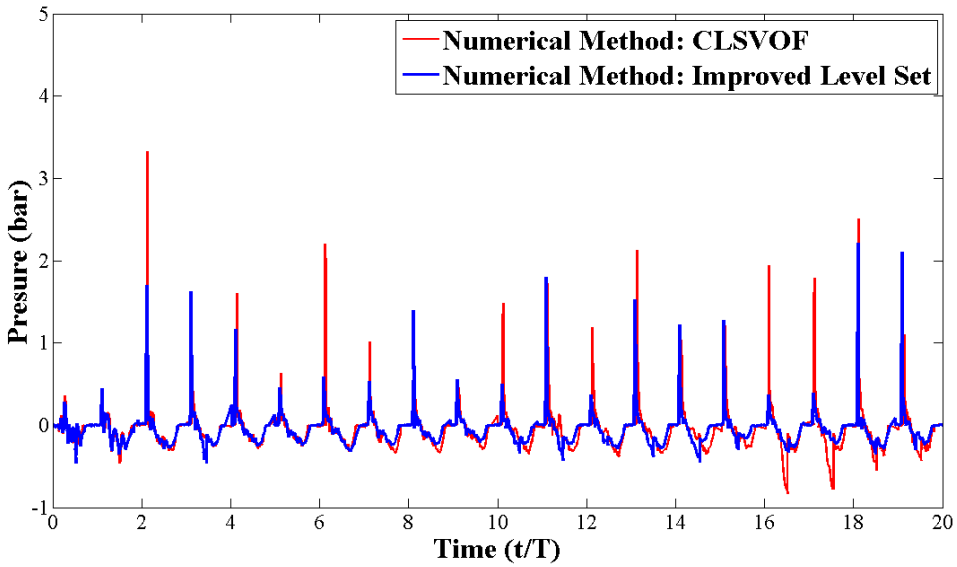

(a) At the location of sensor S9

Figure 5.26: Comparisons of predicted pressures in Case 4

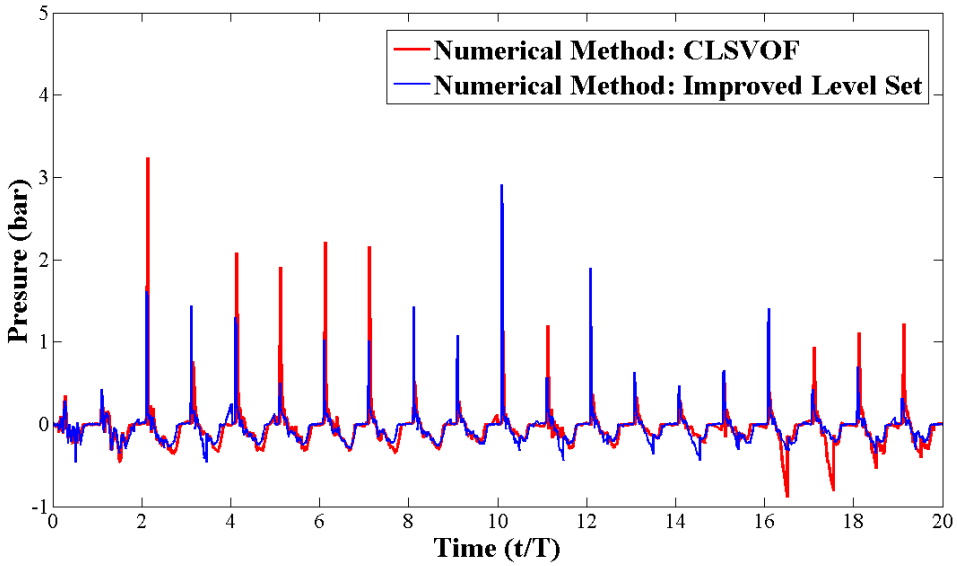

(b) At the location of sensor S10

Figure 5.26: (Continued)

Figure 5.27 shows the snapshots of predicted three-dimensional sloshing flow patterns and pressure contours on the tank walls at six different time instants using the CLSVOF method and the improved level set method. Similar to Case 3, the flow motion is also less violent due to the high filling level condition. However, in 92.5% filling level condition, the air region is so confined that there is always wet region on the top tank face in most of time. Therefore, some portions of air are trapped into water region and form several air pockets inside the water under the top ceiling. These air pockets also develop with motion of the tank. Also because of close to the full tank filling condition, the water attached to the top ceiling is not easy to separate from the tank top face until the tank rotates to large angle. It can explain there is obvious transition from the impact

peak pressure to the suction peak pressure. In addition, the CLSVOF method can capture the development of the air bubbles inside the water; while such air bubbles disappear quickly in the results of the level set method.

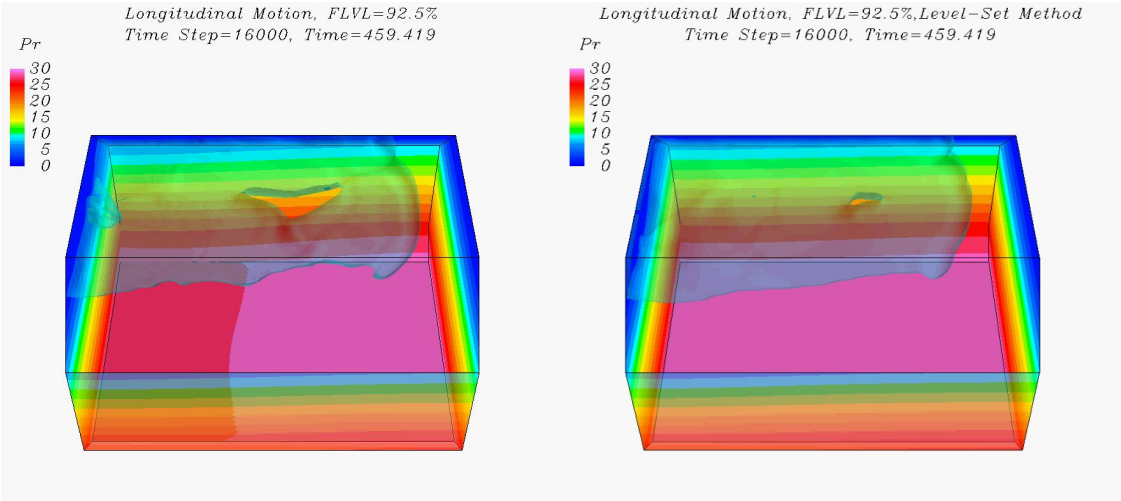

(a) t/T = 16.00

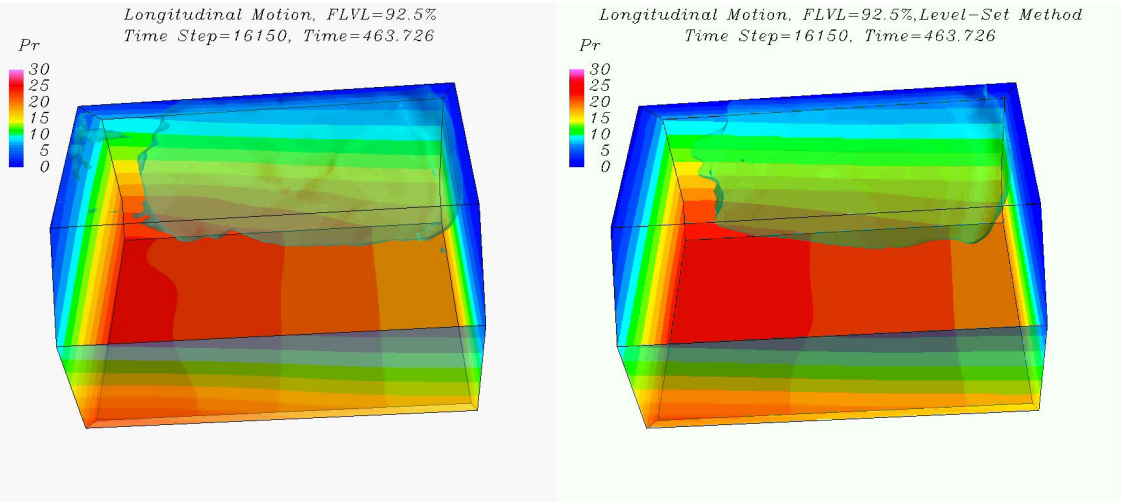

(b) t/T = 16.15

Figure 5.27: Free surface pattern and wall pressure contours, Case 4

(Left column: the CLSVOF method; right column: the improved level set method)

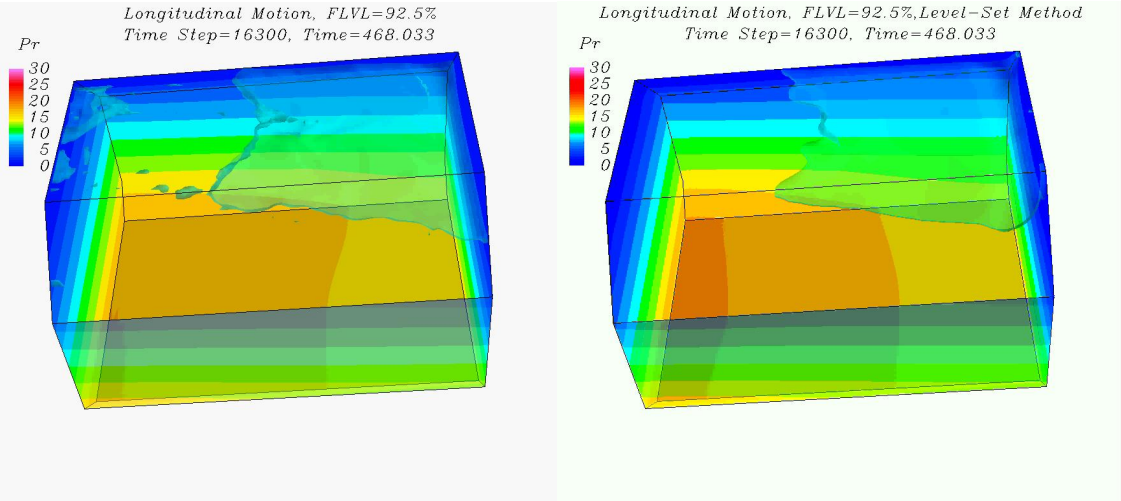

(c) t/T = 16.30

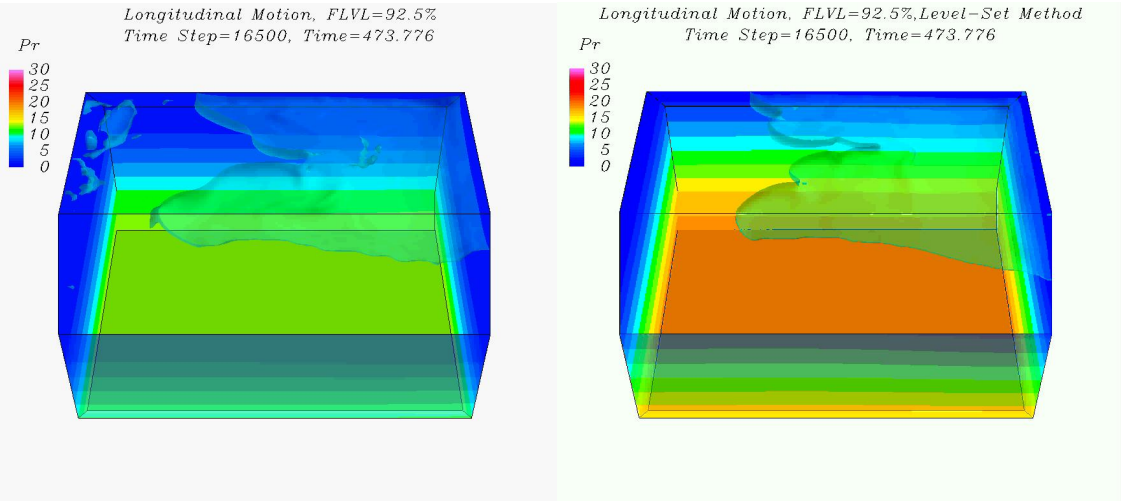

(d) t/T = 16.50

Figure 5.27: (Continued)

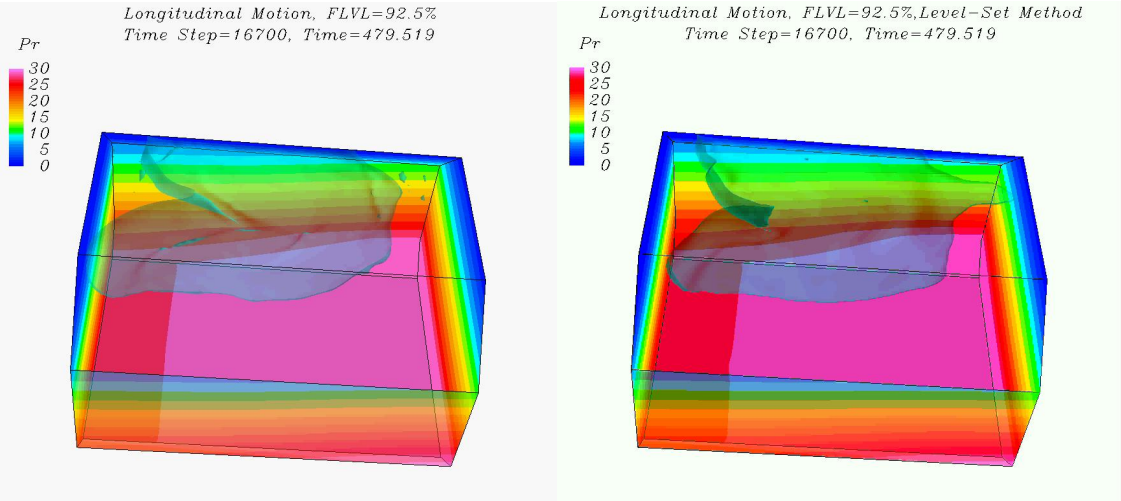

(e) t/T = 16.70

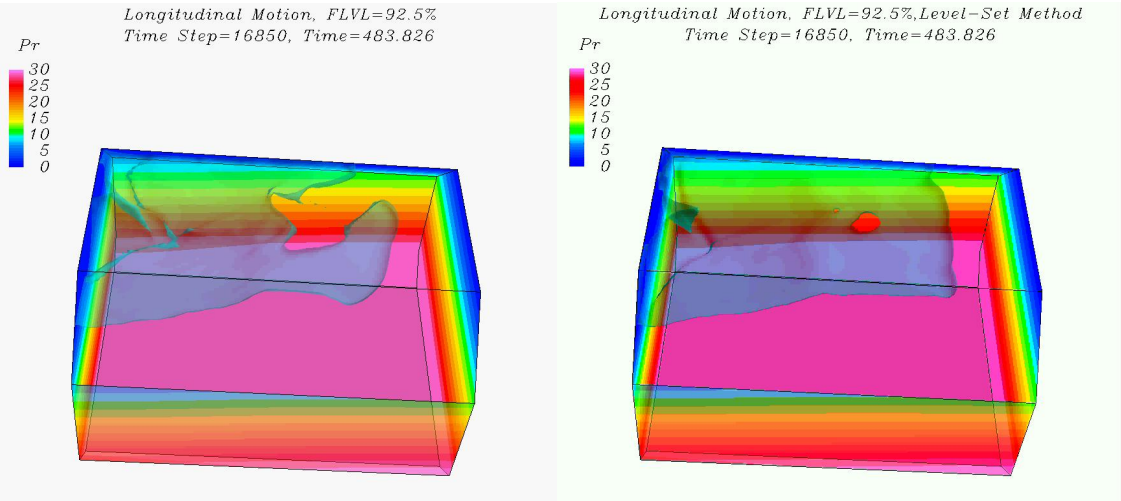

(f) t/T = 16.85

Figure 5.27: (Continued)

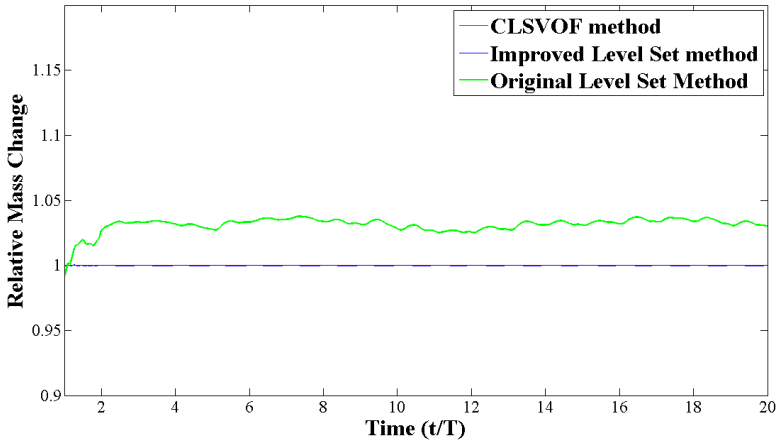

(a) Relative mass change by CLSVOF, improved LS and LS

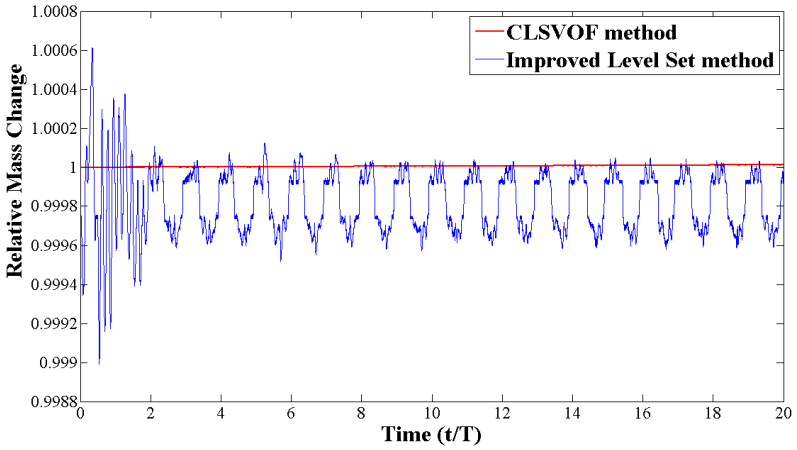

(b) Relative mass change by CLSVOF and improved LS

Figure 5.28: Relative mass change in Case 4

Figure 5.28 shows the time history of the relative mass change by the three numerical methods: the CLSVOF method, improved level set method and the original level set method. The final mass by original level set method after 20 periods obtains extra 3% of the initial mass. The “global” and “local” mass conservation can achieve the

mass conservation, but the “global” mass conservation mechanism cannot preserve exact mass conservation as the “local” mass conservation scheme does.

CHAPTER VI

REGULAR WAVES SLAMMING ON PLATFORM

6.1 Introduction

Wave induced loads on offshore structures are crucial for both the design and the operation of the structures. The impulse loads with large pressure peaks can occur when extreme waves inundate the deck of offshore structures. These loads acting upon the deck are called “slamming” forces. Different from other wave loads, slamming loads happen in much localized space, and in very short time. The impulsive slamming loads may cause damage to the horizontal decks of offshore structure or lead to the collapse of the whole structure.

Here is a review of the theoretical and experimental investigations relating to wave slamming on offshore structures: Wang developed the theoretical technique to predict for both the slow-rise pressure component and the impact components for different incident waves [57]. Kaplan presented an analytical solution to determine the time history of the slamming forces acting on horizontal deck structures [58]. Kaplan also extended the research to predict the wave impact forces and the horizontal forces acting on offshore deck structures during large incident waves [59]. Iwanowski et al. computed the impact loads, through a solution of complete Navier-Stokes equations, with the VOF method [60]. Ren and Wang presented the investigation of random wave slamming on structures in the splash zone by the VOF method [61].

The present study is carried out to analyze the regular wave loads on the underside of a box shaped platform located above the mean water level. The CLSVOF method is employed as the interface-capturing method for time-domain simulation of the regular wave slamming on the platform deck. The slamming impact loads on the underside of the box shaped platform are predicted by the CLSVOF method, which are compared with the experimental data. An overset grid system is utilized to facilitate the simulation of complex flow around the platform deck.

6.2 Experimental and Numerical Setups

This section describes the detailed experimental and numerical setups. The wave slamming impact experimental data adopted for comparison purposes are measured by Ren et al. [62]. In the experiment, the wave channel is 50.0m in length, 3.0m in width and 1.0m in height. The water depth is 50.0cm. The platform structure model is designed as 60.0cm long, 60.0cm wide and 2.0cm thick. A cluster of 16 pressure transducers were mounted on the underside of the deck to measure the slamming impact pressure, as illustrated in figure 6.1. The sampling frequency of the total pressure transducers is about 500 Hz. The direction of regular incident wave propagation β is defined in figure 6.2 and chosen to be 0°, and 30°. The wave height H is 10.0cm, the wave period is T = 1.0s, and the wave length L is 1.512m. The clearance of the underside of the structure above the mean water level s is 0.02m.

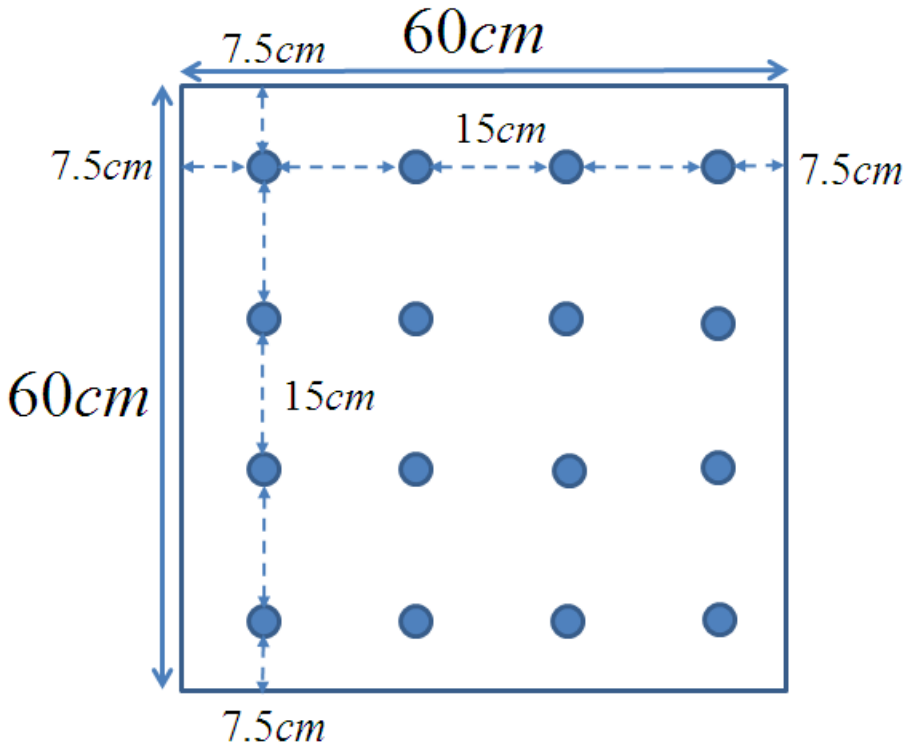

Figure 6.1: Schematic of deck geometry and locations of the pressure transducers

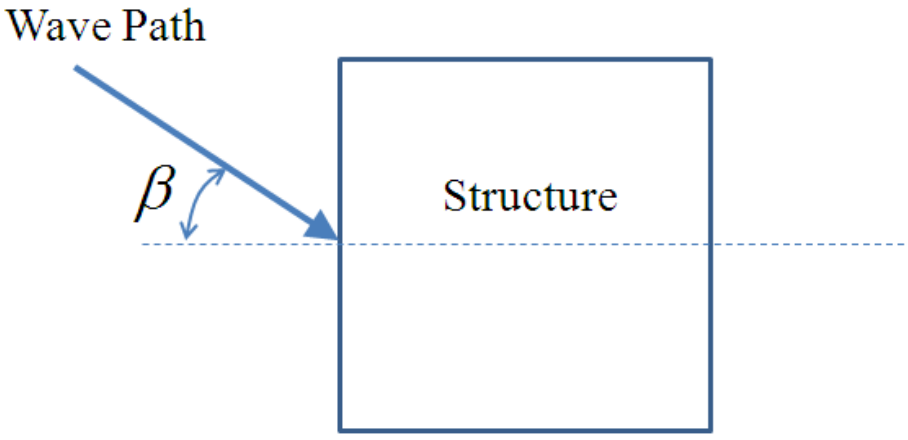

Figure 6.2: Sketch of direction of wave propagation

In the present numerical simulations, the incident wave field is generated using the high order nonlinear wave theory of Cokelet [63]. The characteristic length is 1.0m and Froude number is 1.0. The time increment is chosen as $0.005T$, where T is the wave period. An absorption condition (numerical damping beach) is imposed in the downstream region of the structure. The damping function is specified as,

$$damp = 1 - \frac{1}{2}[1 - \cos(\pi \frac{s_{damp}}{l_{damp}})] \tag{6.1}$$

where s_{damp} is the distance to starting point of damping beach; l_{damp} is the total length of the numerical damping beach. When the damping function is available, all the velocities and pressure within the damping region are damped by this function. Alternatively, another damping method is applied to guarantee the damping effect. It is to generate somewhat coarse grid region in the downstream of the structure. If the grid size is coarse, the low accuracy will lead to damp the numerical solutions.

Moreover, an overset grid system is employed to generate the appropriate grids. In this case, the overset grid system consists of eight computational blocks with a total of 1,197,627 grid points. One block plays the role of wave maker to generate the specified incoming waves to numerical wave tank. One block serves as the wave tank from wave maker to absorbing beach (figure 6.3 (a)). The near-field region is consisted of the other six blocks, which are embedded in wave tank block (figure 6.3 (b)). The platform deck is surrounded by two cubic grids on top and bottom, and four cubic grids on its sides. In this case, a series of cases with different directions of wave propagation are carried out. It is convenient to apply the Chimera domain decomposition technique to generate the

overset grid system. For the girds with different directions, each of blocks is kept in the same dimension and configuration, but the six-block near-field region is rotated by the direction of wave propagation.

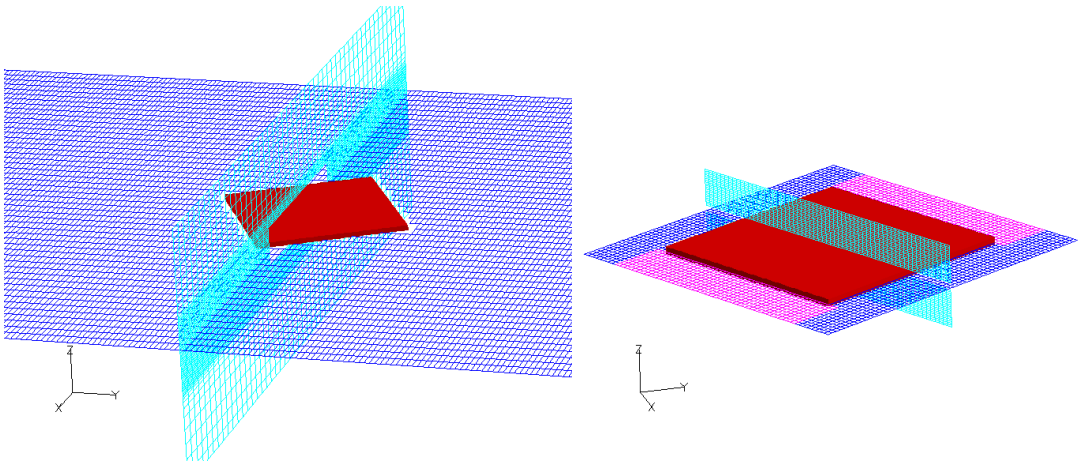

(a) Grid for wave tank (b) Grids for near-field region

Figure 6.3: Overset grid system

6.3 Results and Discussions

All of the simulations are normally performed for about 17 periods. The pressures at selected locations in figure 6.1 are measured by the pressure sensors. The pressures in numerical results are scaled up to the experiment test and compared with the experimental data. The total force acting upon the bottom of the platform deck is calculated by the 16 pressures multiplied the proper areas.

6.3.1 Case 1: 0° direction of wave propagation

The incoming waves are perpendicular waves to the structure when direction of wave propagation is 0°. Figure 6.4 shows snapshots of regular wave impingement on the three-dimensional platform deck in top view and side view perspectives. The incoming wave height H is 0.1m, while the clearance of the underside of the structure above the mean water level s is 0.02m which is lower than the wave crest. The wavelength L is 1.512m, while the size of the structure is $0.6\text{m} \times 0.6\text{m}$ which can only occupy some portion of one complete wave. When the wave trough reaches the structure, there exists sufficient air gap between the underside of the deck and the free surface. The slamming impact can be avoided until the wave crest reaches the structure. The rising elevation of the wave not only impinges the underside of the deck, but also inundates some of topside deck region. The impact loads keeps acting upon the deck until the water attached to the downside of the deck is going to recede. The water on the top of the deck continues its motion with its kinetic energy, and most of them falls down to the water wave from the sides of the deck. Moreover, the flow field in the downstream of the structure is also disturbed by the deck. The ripples can be captured behind the structure and follow the waves to far field.

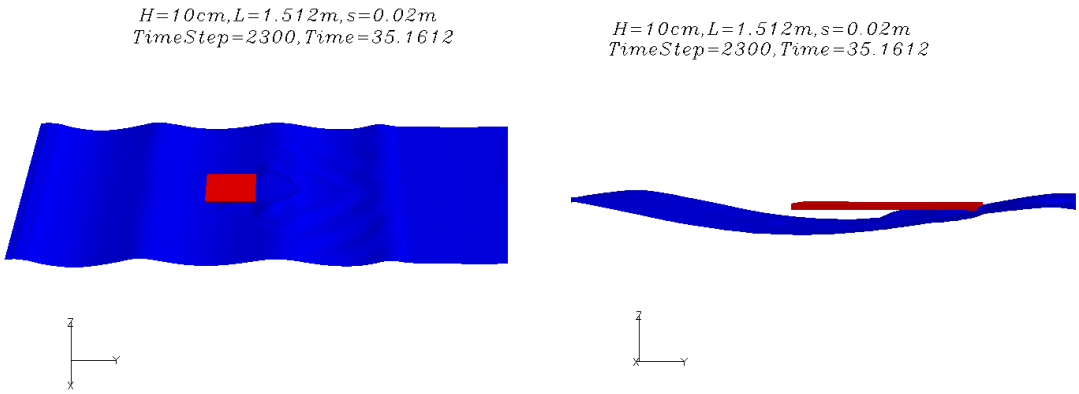

(a) t/T = 11.5

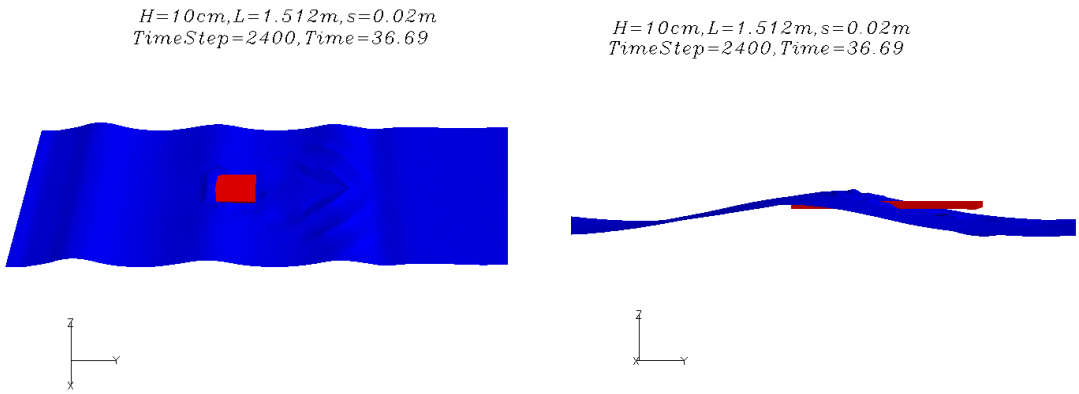

(b) t/T = 12.0

Figure 6.4: Free surface pattern in top view and side view, Case 1

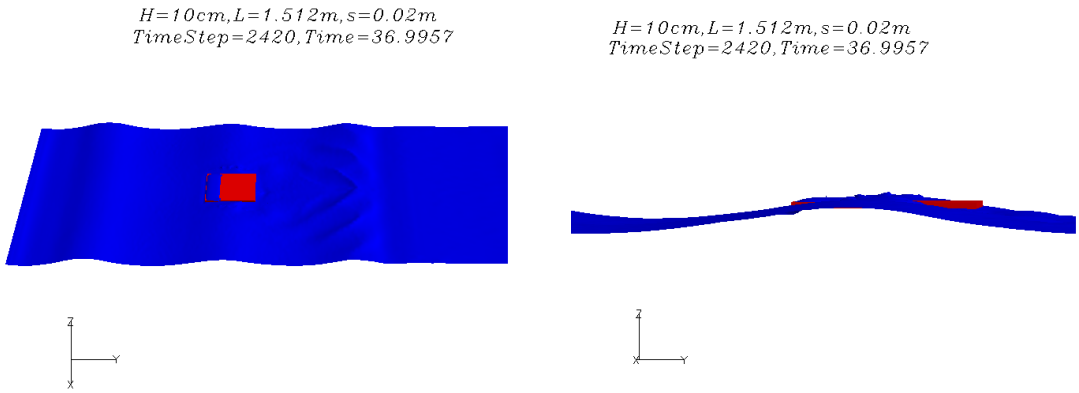

(c) t/T = 12.1

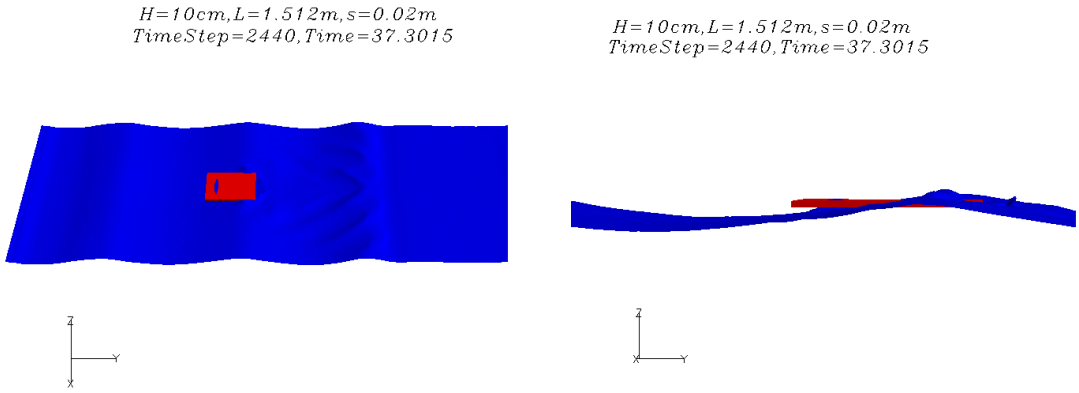

(d) t/T = 12.2

Figure 6.4: (Continued)

Figure 6.5 shows a comparison of the total impacting force on the underside of the deck between numerical result and experimental data. From the time history of the impact force in experiment, the amplitudes of the forces during different periods show strong randomicity. However, the patterns in every period are similar. In one slamming period, there is an impact pattern which is followed by a negative suction peak force.

The impact forces are due to the rising elevation of the free surface, and the suction forces is developed as the water recedes from the underside of the deck. The impact force using the CLSVOF method can also capture the similar impact force pattern. Moreover, the positive peak impact forces in the numerical result is stable around 0.07KN, which are also the approximate mean value of the peak impact forces in experimental result. In addition, the negative peak forces in the numerical result is around -0.03KN, which are also in good agreement with the experimental data.

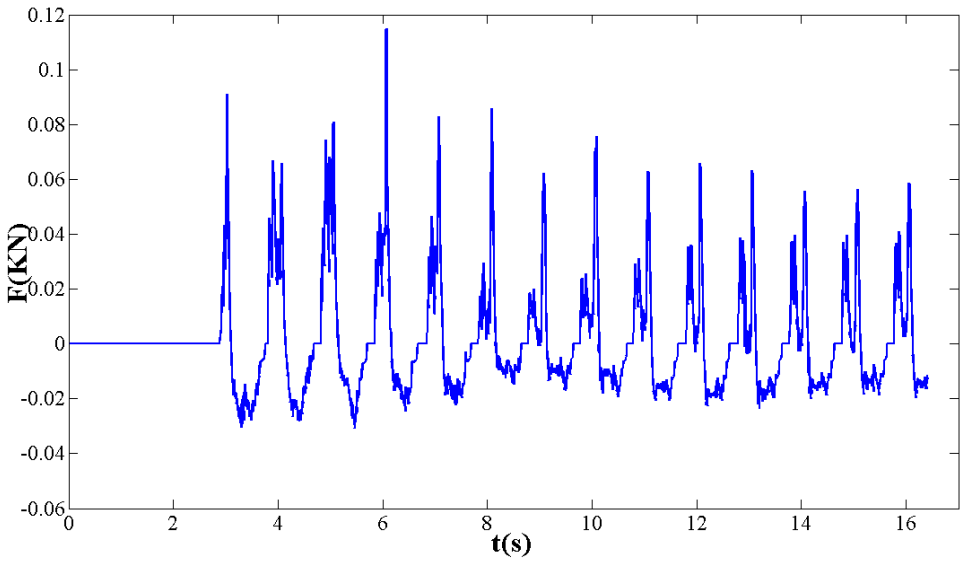

(a) Impact force by the CLSVOF method

Figure 6.5: Wave slamming impact forces, Case 1

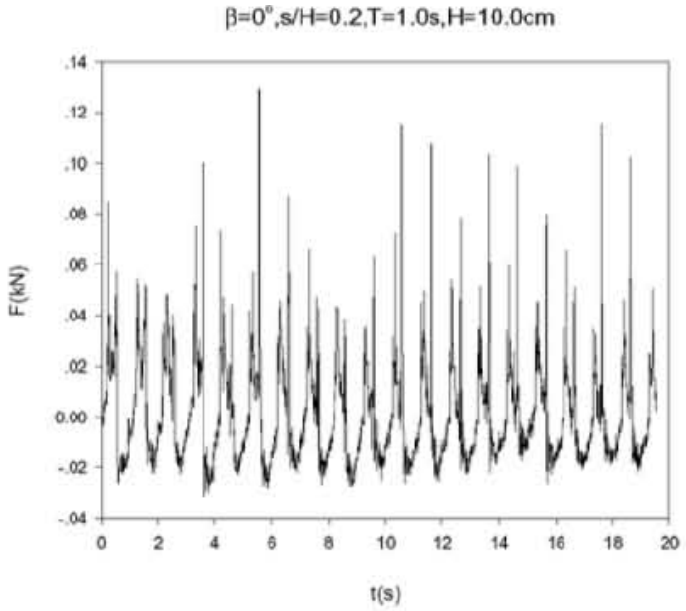

(b) Impact force by experiment

Figure 6.5: (Continued)

6.3.2 Case 2: 30° direction of wave propagation

The incoming waves are oblique waves to the structure when direction of wave propagation is 30°. Figure 6.6 shows snapshots of regular wave impingement on the three-dimensional platform deck in top view and side view perspectives. The patterns in top view and side view are similar those in Case 1. The difference is the incoming waves can climb up to the topside of the deck from two sides, since there is an angle between wave path and the platform deck.

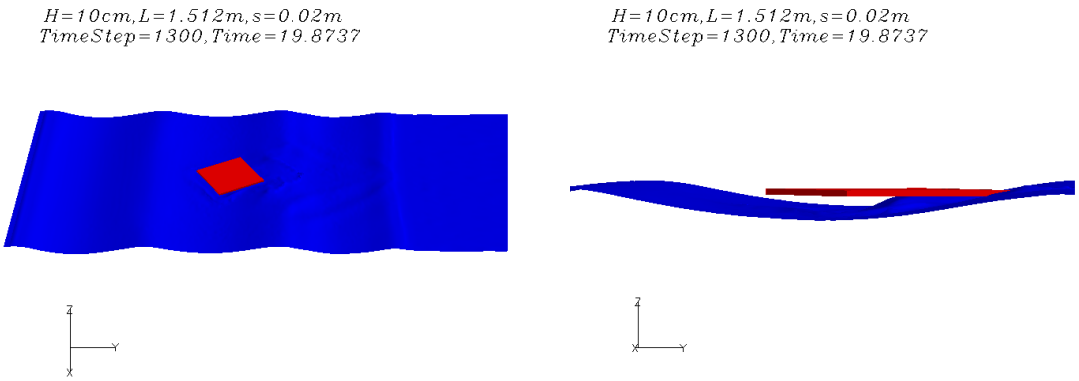

(a) t/T = 6.5

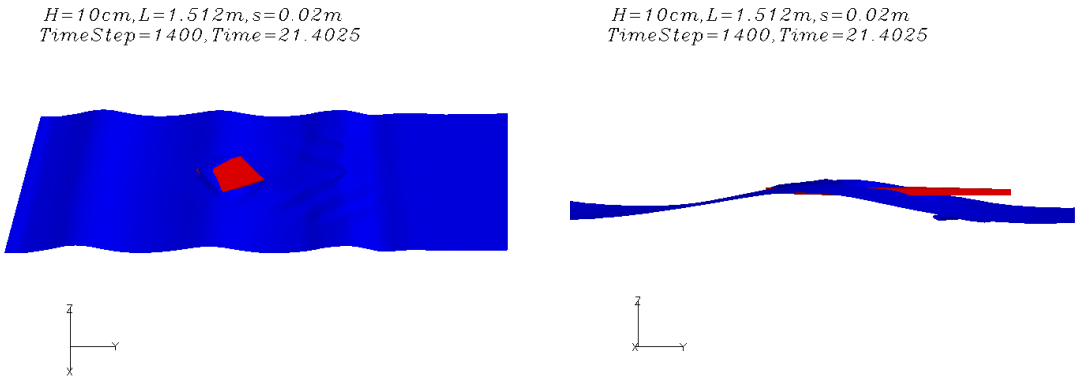

(b) t/T = 7.0

Figure 6.6: Free surface pattern in top view and side view, Case 2

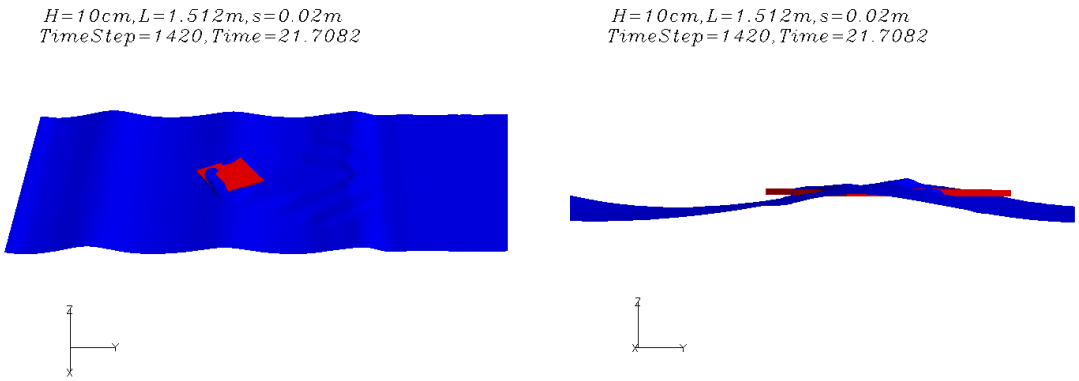

(c) t/T = 7.1

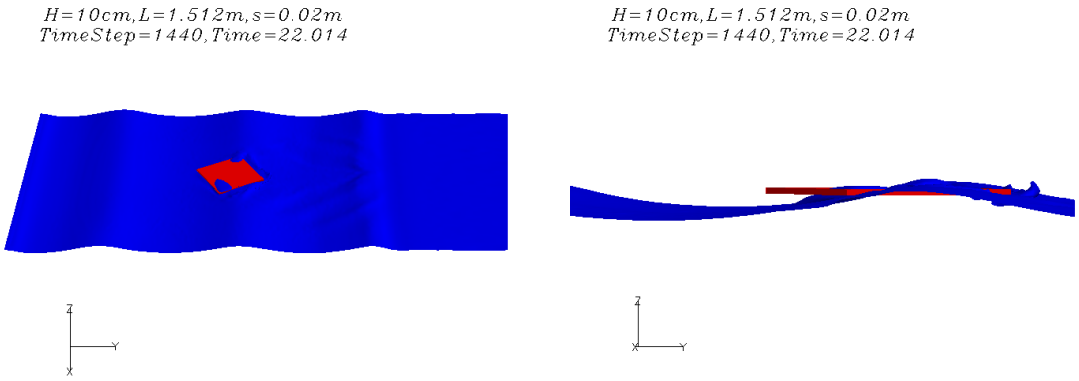

(d) t/T = 7.2

Figure 6.6: (Continued)

Figure 6.7 shows a comparison of the total impacting force on the underside of the deck between numerical result and experimental data. The patterns of peak impact forces followed by suction forces also occur in Case 2. The positive and negative peak forces predicted by the CLSVOF method are close to those in experimental result.

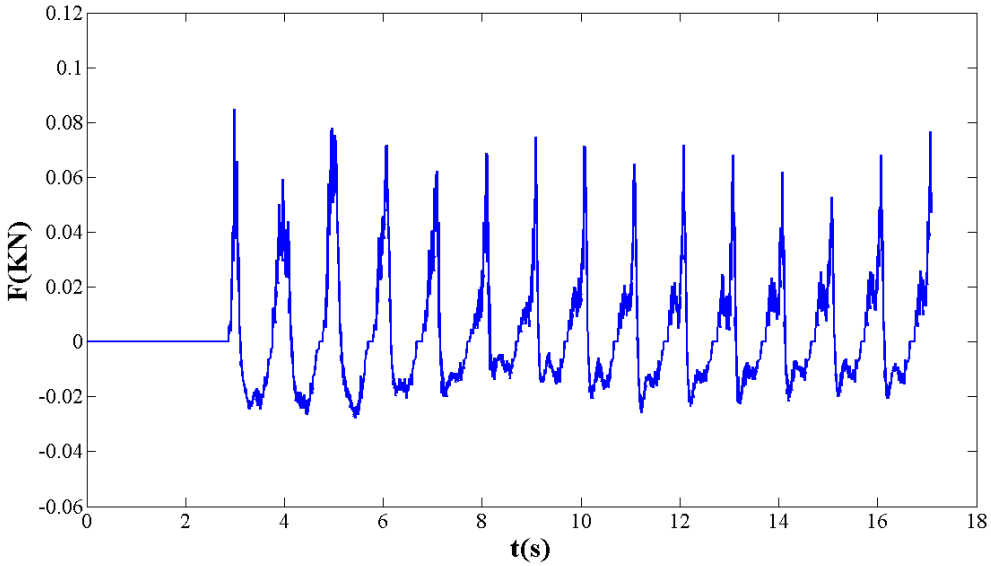

(a) Impact force by the CLSVOF method

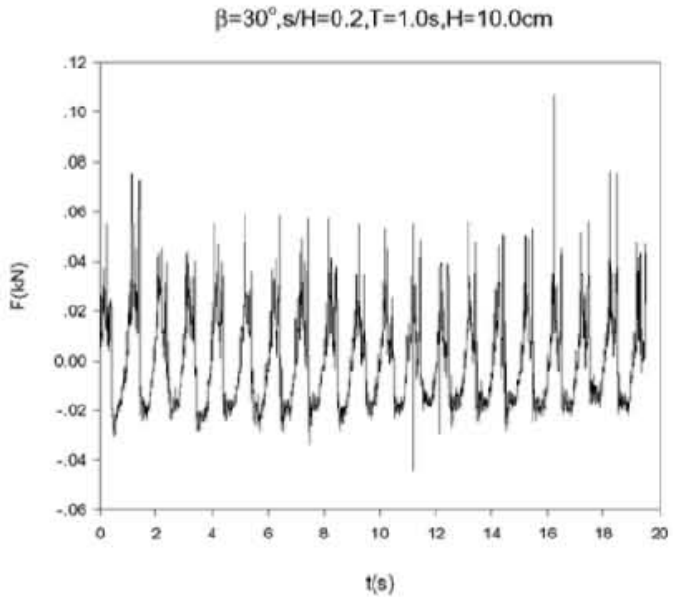

(b) Impact force by experiment

Figure 6.7: Wave slamming impact forces, Case 2

CHAPTER VII

CONCLUSIONS

In previous chapters, the CLSVOF method as a hybrid method has been presented to strengthen the advantages of the pure level set and the pure VOF method and also to avoid the potential predicament by either of the methods. The CLSVOF method is proposed for general overset grid system to solve the complex fluid-structure interaction problems in industrial field. In addition, a new mass conservation scheme for general overset grid system has been implemented in the CLSVOF method to ensure the inherit quality of mass conservation.

In Chapter IV, several benchmark test cases have been implemented to verify the CLSVOF method in the aspects regarding sharp interface capturing and exact mass conservation. Single vortex case under the prescribed velocity field is a qualified test case to independently validate the interface capturing scheme in the present CLSVOF method. The numerical solutions are straightforward to contrast the available analytical solutions at any time instance. The author designed a series of single vortex test cases to validate the CLSVOF method for 2D case, for 3D case, for single Cartesian gird, for single curvilinear grid, and for an overset grid system. The series of single vortex test cases demonstrate that the CLSVOF method can capture the accurate interface motion and preserve exact mass conservation. The present CLSVOF method has also been employed in conjunction with the FANS flow solver to solve the violent free surface

flow problems. The dam breaking case in 2D and in 3D cases are fundamental cases which have reliable experimental data from plenty publications.

In Chapter V, the CLSVOF method was used to capture the sloshing flow induced by the transverse or longitudinal motion of a membrane-type LNG tank. One 3D curvilinear grid block with the motion in multiple degrees of freedom was employed for this case. The impact pressures predicted by the CLSVOF method were compared with the experimental data and the numerical data by the pure level set method. The comparisons about the impact pressures showed the good agreements between the results by the CLSVOF method and the experimental results. In addition to the accurate impact pressure prediction, the CLSVOF method can turn the sloshing phenomena to reality. The details about the breaking flow including liquid droplets and air pockets are also captured by the CLSVOF method.

In Chapter VI, the CLSVOF method was used to simulate the green-water over the 3D platform deck and predict the slamming impact force acting upon the underside of the deck. An overset grid system was employed for this case. By designing a numerical wave tank, the nonlinear regular waves can be continuously propagating and impinge the deck. On the one hand, it can be observed that the wave ran up and inundated the deck. On the other hand, the impact forces acting on the underside of the deck were able to be predicted. Moreover, the positive and negative impact peak forces can be accurately predicted by the CLSVOF method.

In conclusion, this study can be generally applied to predict the interface motion of any immiscible two-phase fluids flow. The capability of the present CLSVOF method

for overset grid system is one prominent feature, which can be an efficient, accurate and robust tool to handle the complex fluid-structure interaction problems. It is the motivation of the author to pursue the present methodology at the beginning of this study.

REFERENCES

[1] F.H. Harlow, and J.E. Welch, "Numerical calculation of time-dependent viscous incompressible flow of fluid with free surface," *Physics of Fluids*, vol. 8, no. 12, pp. 2182-2189, 1965.

[2] B.J. Daly, "A technique for including surface tension effects in hydrodynamics calculation," *Journal of Computational Physics*, vol. 4, pp. 97-117, 1969.

[3] C.W. Hirt, and B.D. Nichols, "Volume of fluid (VOF) method for the dynamics of free boundaries," *Journal of Computational Physics*, vol. 39, pp. 201-225, 1981.

[4] W.F. Noh, and P.R. Woodward, "SLIC (simple line interface method)," *Lecture Notes in Physics*, vol. 59, pp. 330-340, 1976.

[5] S.J. Osher, and J.A. Sethian, "Fronts propagating with curvature dependent speed: algorithms based on Hamilton-Jacobi formulations," *Journal of Computational Physics*, vol. 79, pp. 12-49, 1988.

[6] M.D. Torrey, L.D. Cloutman, R.C. Mjolsness, and C.W. Hirt, "NASA-VOF2D: a computer program for incompressible flows with free surfaces," Technical Report LA-10612-MS, Los Alamos National Laboratory, NM, 1985.

[7] M.D. Torrey, R.C. Mjolsness, and L.R. Stein, "NASA-VOF3D: a three-dimensional computer program for incompressible flows with free surfaces," Technical Report LA-11009-MS, Los Alamos National Laboratory, NM, 1987.

[8] D.B. Kothe, R.C. Mjolsness, and M.D. Torrey, "RIPPLE: a computer program for incompressible flows with free surfaces," Technical Report LA-12007-MS, Los Alamos National Laboratory, NM, 1991.

[9] D.B. Kothe, and R.C. Mjolsness, "RIPPLE: a new model for incompressible flows with free surfaces," *AIAA Journal*, vol. 30, no. 11, pp. 2694-2700, 1998.

[10] C.W. Hirt, and B.D. Nichols, "FLOW-3D Users Manual," Flow Sciences, Tech. Rep. V9.2. 1988.

[11] D.L. Youngs, "Time-dependent multi-material flow with large fluid distortion," Numerical Methods for Fluid Dynamics, K.W. Morton and M.J. Baines, Eds. London: Academic Press, pp. 273-285, 1982.

[12] F.L. Addessio, D.E. Carroll, J.K. Dukowicz, F.H. Harlow, J.N. Johnson, B.A. Kashiwa, M.E. Maltrud, and H.M, Ruppel, "CAVEAT: a computer code for fluid dynamics problems with large distortion and internal slip," Technical Report LA-10613-MS, Los Alamos National Laboratory, NM, 1986.

[13] P. Colella, L.F. Henderson, and E.G. Puckett, "A numerical study of shock wave refractions at a gas interface," *in Proceedings of the AIAA Ninth Computational Fluid Dynamics Conference*, AIAA Paper 89-1973-CP, 1989.

[14] J.E. Pilliod Jr., and E.G. Puckett, "Second-order accurate volume-of-fluid algorithms for tracking material interfaces," *Journal of Computational Physics*, vol. 199, pp. 465-502, 2004.

[15] R. Scardovelli, and S. Zalesaki, "Interface reconstruction with least-square fit and split Eulerian-Lagrangian advection," *International Journal for Numerical Methods in Fluids*, vol. 41, pp. 251-274, 2003.

[16] W.J. Rider, and D.B. Kothe, "Reconstructing volume tracking," *Journal of Computational Physics*, vol. 141, pp. 112-152, 1998.

[17] J. Lopez, J. Hernandez, P. Gomez, and F. Faura, "A volume of fluid method based on multidimensional advection and spline interface reconstruction," *Journal of Computational Physics*, vol. 195, pp. 718-742, 2004.

[18] K. Shahbazi, M. Paraschivoiu, and J.Mostaghimi, "Second order accurate volume tracking based on remapping for triangular meshes," *Journal of Computational Physics*, vol. 188, pp. 100-122, 2003.

[19] N. Ashgriz, T. Barbat, and G. Wang, "A computational Lagrangian-Eulerian advection remap for free surface flows," *International Journal for Numerical Methods in Fluids*, vol. 44, pp. 1-32, 2004.

[20] E.G. Puckett, and J.S. Saltzman, "A 3-d adaptive mesh refinement algorithm for multimaterial gas dynamics," *Physica D*, vol. 60, pp. 84-104, 1992.

[21] B.J. Parker, and D.L. Youngs, "Two and three dimensional Eulerian simulation of fluid flow with material interface," Technical Report 01/92, UK Atomic Weapon Establishment, Aldermaston, Berkshire, 1992.

[22] E.G. Puckett, "A volume-of-fluid interface tracking algorithm with applications to computing shock wave refraction," *in Proceedings of the Fourth International Symposium on Computational Fluid Dynamics*, Davis, CA, pp. 933-938, 1991.

[23] J.E. Pilliod, "An analysis of piecewise linear interface reconstruction algorithms for volume-of-fluid methods," M.S. Thesis, University of California, Davis, 1992.

[24] M. Sussman, P. Smereka, and S. Osher, "A level set approach for computing solutions to incompressible two-phase flow," *Journal of Computational Physics*, vol. 114, pp. 146-159, 1994.

[25] M. Sussman, E. Fatemi, P. Smereka, and S. Osher, "An improved level set method for incompressible two-phase flows," *Computers & Fluids*, vol. 27, pp. 663-680, 1998.

[26] H. Takahira, T. Horiuchi, and S. Banerjee, "An improved three-dimensional level set method for gas-liquid two-phase flows," *Journal of Fluids Engineeing*, vol. 126, pp. 578-585, 2004.

[27] S.P. Van der pijl, A. Segal, C. Vuik, and P. Wesseling, "A mass-conserving level set method for modeling of multi-phase flows," *International Journal for Numerical Methods in Fluids*, vol. 47, pp. 339-361, 2005.

[28] D. Enright, R. Fedkiw, J. Ferziger, and I. Mitchell, "A hybrid particle level set method for improved interface capturing," *Journal of Computational Physics*, vol. 183, pp. 83-116, 2002.

[29] E. Aulisa, S. Manservisi, and R. Scardovelli, "A mixed markers and volume-of-fluid method for the reconstruction and advection of interfaces in two-phase and free-boundary flows," *Journal of Computational Physics*, vol. 188, pp. 611-639, 2003.

[30] M. Sussman, and E.G. Puckett, "A coupled level set and volume-of-fluid method for computing 3d and axisymmetric incompressible two-phase flow," *Journal of Computational Physics*, vol. 162, pp. 301-337, 2000.

[31] M. Sussman, "A second order coupled level set and volume-of-fluid method for computing growth and collapse of vapor bubbles," *Journal of Computational Physics*, vol. 187, pp. 110-136, 2003.

[32] G.S. Jiang, and C.W. Shu, "Efficient implementation of weighted ENO schemes," *Journal of Computational Physics*, vol. 126, pp. 202-228, 1996.

[33] D. Gueyffier, J. Li, A. Nadim, R. Scardovelli, and S. Zaleski, " Volume-of-Fluid interface tracking with smoothed surface stress methods for three-dimensional flows," *Journal of Computational Physics*, vol. 152, pp. 423-456, 1999.

[34] R.P. Brent, "Algorithms for minimization without derivatives," Englewood Cliffs, NJ: Prentice-Hall, Chapters 3-4, 1973.

[35] E. Aulisa, S. Manservisi, R. Scardovelli, and S. Zaleski, "Interface reconstruction with least-squares fit and split advection in three-dimensional Cartesian geometry," *Journal of Computational Physics*, vol. 225, pp. 2301-2319, 2007.

[36] Y. Zhao, and H.C. Chen, "CFD simulation of violent free surface flows by a coupled level-set and volume-of-fluid method," *in Proceedings of the 23th International Offshore and Polar Engineering Conference*, vol. 3, pp. 968-975, 2013.

[37] A. Bourlioux, "A coupled level-set volume-of-fluid algorithm for tracking material interfaces," *in Proceedings of the 6th International Symposium on Computational Fluid Dynamics,* Lake Tahoe, CA, USA, 1995.

[38] G. Son, and N. Hur, "A coupled level set and volume-of-fluid method for the buoyancy-driven motion of fluid particles," *Numerical Heat Transfer*, Part B, vol. 42, pp. 523-542,2002.

[39] G. Son, "Efficient implementation of a coupled level-set and volume-of-fluid method for three-dimensional incompressible two-phase flows," *Numerical Heat Transfer*, Part B, vol. 43, pp. 549-565, 2003.

[40] T. Menard, S. Tanguy, and A. Berlemont, "Coupling level set/VOF/ghost fluid methods: Validation and application to 3D simulation of the primary break-up of a liquid jet," *International Journal of Multiphase Flow*, vol. 33, pp. 510-524, 2007.

[41] X. Yang, A.J. James, J. Lowengrub, X. Zheng, and V. Cristini, " An adaptive coupled level-set/volume-of-fluid interface capturing method for unstructured triangular girds," *Journal of Computational Physics*, vol. 217, pp. 364-394, 2006.

[42] Z. Wang, J. Yang, B. Koo, and F. Stern, "A coupled level set and volume-of-fluid method for sharp interface simulation of plunging breaking waves," *International Journal of Multiphase Flow*, vol. 35, pp. 227-246, 2009.

[43] Z. Wang, J. Yang, and F. Stern, "A new volume-of-fluid method with a constructed distance function on general structured grids," *Journal of Computational Physics*, vol. 231, pp. 3703-3722, 2012.

[44] H.C. Chen, and K. Yu, "CFD simulation of wave-current-body interactions including greenwater and wet deck slamming," *Computers & Fluids*, vol. 38, pp. 970-980, 2008.

[45] H.C. Chen, "Time-domain simulation of nonlinear wave impact loads on fixed offshore platform and decks," *International Journal of Offshore and Polar Engineering*, vol. 20, No. 4, pp. 275-283, 2010.

[46] J.C. Martin, and W.J. Moyce, "An experimental study of the collapse of liquid columns on a rigid horizontal plane," *Philosophical Transactions of the Royal Society of London*, vol. 244, pp. 312-324, 1952.

[47] M. Arai, L.Y. Cheng, A. Kumano, and T. Miyamoto, "A technique for stable numerical computation of hydrodynamic impact pressure in sloshing simulation," *Journal of the Society of Naval Architects of Japan*, vol. 191, pp. 299-307, 2002.

[48] M. Arai, L.Y. Cheng, "An accurate and stable method for computing sloshing impact pressure and its application to the study of bulk-carrier ballast-tank sloshing," *in Proceedings of the 9th symposium on practical design of ships and other floating structures*, Luebeck-Travemuende, Germany, 2004.

[49] B.W. Nam, and Y. Kim, "Simulation of two-dimensional sloshing flows by SPH method," in Proceedings of the 16th *International Offshore and Polar Engineering Conference*, pp. 342-347, 2006.

[50] Y. Kim, "Numerical simulation of sloshing flows with impact load," *Applied Ocean Research*, vol. 23, pp. 53-62, 2001.

[51] Y. Kim, "Numerical study on sloshing-induced impact pressures on three-dimensional prismatic tanks," *Applied Ocean Research*, vol. 26, pp. 213-216, 2004.

[52] E. Loots, W. Pastoor, B. Buchner, and T. Tveitnes, "The numerical simulation of LNG sloshing with an improved volume of fluid method," *in Proceedings of the 23rd International Conference on Offshore Mechanics and Arctic Engineering*, 2004.

[53] R. Wemmenhove, E. Loots, R. Luppes, and A.E.P. Veldman, "Modeling two-phase flow with offshore applications," *in Proceedings of the 24th International Conference on Offshore Mechanics and Arctic Engineering*, 2005.

[54] K. Yu, H.C. Chen, J.W. Kim, and Y.B. Lee, "Numerical simulation of two-phase sloshing flow in LNG tank using finite-analytic level-set method," *in Proceedings of the 26th International Conference on Offshore Mechanics and Arctic Engineering*, 2007.

[55] H.C. Chen, "CFD simulation of compressible two-phase sloshing flow in a LNG tank," *Ocean Systems Engineering*, vol. 1, No. 1, pp. 29-55, 2011.

[56] Y.B. Lee, J.M. Lee, Y.S. Kim, J.H. Jung, D.W. Jung, and S.H. Kwon, "An experimental study of impulsive sloshing load acting on LNGC tank," *in Proceedings of the 16th International Offshore and Polar Engineering Conference*, 2006.

[57] H. Wang, "Water wave pressure on horizontal plates," *Journal of the Hydraulics Division*, vol. 96, No. 10, pp. 1997-2017, 1970.

[58] P. Kaplan, "Wave impact force on offshore structures: re-examination and new interpretations," *in Proceedings of Offshore Technology Conference,* OTC-6814, pp. 79-86, 1992.

[59] P. Kaplan, J.J. Murray, W.C. Yu, "Theoretical analysis of wave impact forces on platform deck structures," *in Proceedings of the 14th International Conference on Offshore Mechanics and Arctic Engineering*, pp. 189-198, 1995.

[60] B. Iwanowski, H. Grigorian, I. Scherf, "Subsidence of the Ekofisk platforms: wave in deck impact study, Various wave models and computational methods," *in Proceedings of the 21th International Conference on Offshore Mechanics and Arctic Engineering*, pp. 95-102, 2002.

[61] B. Ren, Y. Wang, "Numerical simulation of random wave slamming on structures in the splash zone," *Ocean Engineering*, vol. 31, pp. 547-560, 2004.

[62] B. Ren, Z. Ding, Y. Wang, and X. Ren, "Experimental study of regular wave impact on the three-dimensional structure in the splash zone," *in Proceedings of the 17th International Offshore and Polar Engineering Conference*, 2007.

[63] E.D. Cokelet, "Steep gravity waves in water of arbitrary uniform depth," *Philosophical Transactions of Royal Society of London*, vol. 286, pp. 183-230, 1977.